

UNIVERSITY OF CALIFORNIA

Los Angeles

Plasma Wakefield Acceleration of an
Intense Positron Beam

A dissertation submitted in partial satisfaction
of the requirements for the degree Doctor of Philosophy
in Electrical Engineering

by

Brent Edward Blue

2003

© Copyright by

Brent Edward Blue

2003

The dissertation of Brent Edward Blue is approved.

Oscar Stafsuud

Warren B. Mori

Claudio Pellegrini

Chandrasekhar J. Joshi, Committee Chair

University of California, Los Angeles

2003

This dissertation is dedicated to my parents, my grandparents,
my sister, and my brother

Table of Contents

List of Figures	vi
List of Tables	ix
Acknowledgements	x
Vita	xii
Abstract	xv
1 Introduction	1
1.1 Plasma wakefield accelerator	1
1.2 Electron beam driven plasma wakefield accelerators	2
1.3 Regimes of electron beam driven PWFAs	3
1.4 Positron Beam Driven PWFAs	6
1.5 Regimes of positron beam driven PWFAs	7
1.6 Review of previous PWFA work	9
1.7 Summary of the dissertation	10
2 Theory and Simulations	13
2.1 Plasma impulse response (linear theory)	13
2.2 Scaling laws explored through PIC simulations for a positron beam	24
2.3 3-D Particle in Cell Simulations	41
3 Experimental Setup and Diagnostics	43
3.1 Lithium plasma source	45
3.2 Measurement of plasma density	47
3.3 Plasma decay	52
3.4 Imaging Spectrometer	57
3.5 Proof that the spectrometer is imaging in x	57
3.6 Optical Transition Radiators (OTR)	60
3.7 Proof of OTR resolution	64
3.8 Beam Position Monitors (BPMs)	67
3.9 Aerogel Cherenkov Radiator	68
3.10 Time-Integrated Cherenkov Calibration	71
3.11 Streak Camera Calibration	73
3.12 Measurement of bunch length	75
4 Transverse Dynamics of the Positron Beam	77
4.1 Focusing and Defocusing	77
4.2 Is there evidence of a hosing instability?	81
4.3 Effect of transverse dynamics on energy gain diagnostic	87

5 Longitudinal Dynamics of the Positron Beam in a Meter Long Plasma Column	96
5.1 Energy loss of core of beam	96
5.2 Energy Gain	100
6 Conclusion	106
Appendix A Experimental Facilities	107
A.1 Stanford Linear Accelerator (SLAC)	107
A.2 Linac beam transport. Why low charge?	108
A.3 Final Focus Test Beam (FFTB)	111
Appendix B Compendium of analyzed images	112
Appendix C Design for an advanced accelerator	124
C.1 3 rd generation plasma wakefield accelerators	124
C.2 Simulations of proton driven PWFAs	127
C.3 Methods of generating short ($<100\mu\text{m } \sigma_z$) proton pulses	136
Bibliography	140

List of Figures

Chapter 1

1.2.1	Wakefield generated by an electron beam	3
1.4.1	Wakefield generated by a positron beam	7
1.4.1	Ranges and types of plasmas	8

Chapter 2

2.2.1	Convention of Analysis	27
2.2.2	Peak Decelerating Field vs. Charge	28
2.2.3	Peak Accelerating Field vs Charge	29
2.2.4	Peak Decelerating Field vs Plasma Density	31
2.2.5	Peak Accelerating Field vs Plasma Density	32
2.2.6	Accelerating Bucket Width vs Plasma Density	33
2.2.7	Number of Accelerated Particles vs Plasma Density	34
2.2.8	Peak Fields vs Bunch Radius	35
2.2.9	Peak Fields vs Bunch Length	37
2.2.10	Optimized ($k_p \sigma_z = \sqrt{2}$) Fields vs Bunch Length	40
2.3.1	Beam energy at the exit of the plasma cell	42

Chapter 4

3.0.1	Schematic of experimental setup	45
3.1.1	Diagram of Lithium Oven Setup and Depiction of Lithium Column	46
3.2.1	Temperature and vapor density profile inside oven	48
3.2.2	Focusing of laser in x and y through oven	50
3.2.3	Area of laser pulse as it propagates through the oven	50
3.2.4	Plasma density profile with an initial pulse energy of 3 mJ	51
3.3.1	Theoretically predicted plasma density decay	53
3.3.2	Focusing of positron beam vs initial plasma density	54
3.3.3	Betatron oscillations from a experiment and b theory	55
3.3.4	Betatron oscillations a with no plasma decay and b with decay	56
3.5.1	Spot size at plasma exit vs focusing strength	59
3.5.2	Spot size at Cherenkov vs focusing strength	59
3.6.1	Sample upstream OTR image	62
3.6.2	Sample Downstream OTR Image	62
3.6.3	Image analysis of upstream and downstream OTR images	63
3.7.1	USAF 1951 Resolution target	64
3.7.2	Acquired image of resolution target through our OTR optical setup	65
3.7.3	Strip of Focus	66

3.8.1	Typical Stripline BPM	67
3.9.1	Time Integrated Cherenkov Image depicting the parts of the beam seen by the horizontal and vertical slits on the streak camera	70
3.9.2	Typical Streak Camera image showing both the horizontal and vertical streaks	70
3.9.3	Diagram of Cherenkov radiation detector setup	71
3.10.1	Resolution target image on integrated Cherenkov	72
3.10.2	Line out of resolution target for pixel calibration	73
3.11.1	Resolution target for streak camera calibration	74
3.12.1	Time Integrated and Time Resolved images for the same shot	75
3.12.2	Gaussian fit of bunch length	76
Chapter 4		
4.1.1	PIC Simulation of Positron Beam's Transverse Profile	79
4.1.2	Integrated spot size after the plasma vs density	80
4.2.1	Slit location of beam sample	82
4.2.2	3-D y-data extraction from Cherenkov data	83
4.2.3	3-D x,z data extraction from Streak Camera data	83
4.2.4	3-D beam analysis at a plasma density of $5E13 \text{ cm}^{-3}$	85
4.2.5	3-D beam analysis at a plasma density of $1.8E14 \text{ cm}^{-3}$	85
4.2.6	Oscillations of beam slices vs plasma density	86
4.3.1	Imaging Spectrometer Schematic	87
4.3.2	Gaussian propagation through the spectrometer with no energy change	88
4.3.3	Gaussian propagation through the spectrometer with energy change (red)	89
4.3.4	Gaussian propagation with an energy change and offset	91
4.3.5	Unfocused tilted offset beam on streak camera slit	94
4.3.6	Focused, tilted offset beam on streak camera slit	95
Chapter 5		
5.1.1	Energy Loss vs. Plasma Density Measured on the Streak Camera	97
5.1.2	Variations in the Incident Beam Energy	98
5.1.3	Peak energy loss after propagating through 1.4 meters of plasma	99
5.2.1	Amplitude of Slice Data From the Streak Camera	101
5.2.2	Raw data of -6 ps slice	102
5.2.3	Slice Analysis of -6 ps slice	102
5.2.4	Raw Data of 5 ps Slice	103
5.2.5	Slice Analysis of 5 ps slice	103
5.2.6	Time Slice Analysis of the Energy Dynamics with a Positron Bunch	104

Appendix A	
A.2.1	Improved beam quality at lower charge 110
Appendix B	
B.0	Image locations in the following figures. 114
B.1	Shot 185 – No Plasma – Raw Images 115
B.2	Shot 186 – Plasma Density $1.8 \times 10^{14} \text{ e}^- / \text{cm}^3$ – Raw Images 116
B.3	Shot 187 – Plasma Density $1.88 \times 10^{14} \text{ e}^- / \text{cm}^3$ – Raw Images 117
B.4	Shot 188 – Plasma Density $1.69 \times 10^{14} \text{ e}^- / \text{cm}^3$ – Raw Images 118
B.5	Shot 189 – No Plasma – Raw Images 119
B.6	Shot 190 – Plasma Density $1.65 \times 10^{14} \text{ e}^- / \text{cm}^3$ – Raw Images 120
B.7	Shot 191 – Plasma Density $1.92 \times 10^{14} \text{ e}^- / \text{cm}^3$ – Raw Images 121
B.8	Shot 192 – Plasma Density $1.76 \times 10^{14} \text{ e}^- / \text{cm}^3$ – Raw Images 122
B.9	Shot 193 – No Plasma – Raw Images 123
Appendix C	
C.2.1	Wakefield field induced in a plasma by a proton beam 130
C.2.2	Wakefield induced by a proton beam in a Li vapor 131
C.2.3	Tunnel ionized channel width 132
C.2.4	Evolution of the proton drive beam and witness electron beam 133
C.2.5	Energy evolution of the proton drive beam and witness electron beam. 134
C.2.6	Relative separation between an accelerating electron bunch and a decelerating proton bunch in a 10 GeV/m PWFA 136
C.3.1	Wakefield generated by a electron beam in a tunnel ionized plasma. 139

List of Tables

Chapter 1

1.3.1 Regimes of electron beam propagation 4

1.5.1 Regimes of positron beam propagation 8

Chapter 2

2.2.1 Nominal Simulation Parameters 25

Appendix C

C.2.1 Proton PWFA simulation parameters 125

Acknowledgments

It has been a great pleasure to work in the field of plasma physics at UCLA and USC and the field of high-energy physics at Stanford. I would like to thank all of the faculty, staff, and students that I have worked and collaborated with at these first-rate institutions.

In particular I would like to first thank Prof. Muggli for his support and guidance. This work would not have been possible if it were not for the many long hours in the E162 trailer Patrick spent teaching me the dynamics of a positron beam in a plasma. Furthermore, this work was greatly aided by the insight he gave me from his work on analyzing the energy dynamics of an electron beam in a plasma.

I would like to also thank my colleagues at Stanford. Prof. Siemann has helped me out considerably in the fields of high-energy physics. His insight and expertise he instilled upon me during the long hours we spent on shift together has made me a better physicist. Special thanks needs to be given for all of the Matlab code he has written which made my data analysis possible and for the Red Bull he bought me in order to keep me awake so that I could continue running the experiment. I am eternally grateful to all of the work Dr. Hogan has contributed to the E162 experiment. If it were not for his work, none of my work would have been possible. In addition,

Mark taught me the principles of “Strong Body, Strong Mind.” There were many nights where we would work until 1 AM, and then we would go out for a 3 hour bike ride in the freezing cold rain. Furthermore, the retreats we took out to Lake San Antonio so that we could discuss Science and Physics were invaluable to my growth as a Scientist and Philosopher. I would also like to thank Caolionn O’Connell for the countless hours we spent working together on shift and for the hours we spent everyday collaborating over the phone while I was in Los Angeles and she was in Menlo Park. Although we will eternally have different tastes in literature, the magniloquence she has given me will last a lifetime.

I would like to thank David Bruhwiler and the Tech-X Corporation for the use of OOPIC. I would also like to thank the Particle Data Group for the use of their figures detailing high energy physics.

Special thanks need to be given to my colleagues at UCLA whose contributions throughout my graduate career have been invaluable. Wei Lu and Prof. Warren Mori for their assistance on running the OSIRIS simulations. Dr. Chris Clayton has taught me about physics and opened my eyes on seeing problems in a whole new light. Ken Marsh has advised me on topics ranging from Lithium vapor to ultra-endurance cycling. Finally, I would like to thank Prof. Chan Joshi, my advisor, who has given me the opportunity to work on a top notch experiment.

VITA

June 1, 1974	Born, Los Angeles, California
1997	B.S., Electrical Engineering University of California Los Angeles Los Angeles, CA
1998-1989	Electrical Engineering Departmental Fellowship University of California Los Angeles Los Angeles, CA
1998-2000	Research Assistant University of California Los Angeles Los Angeles, CA
1999-2002	Researcher Stanford Linear Accelerator Center Menlo Park, CA
2000	M.S., Electrical Engineering University of California Los Angeles Los Angeles, CA
2000-2003	Research Assistant University of California Los Angeles Los Angeles, CA

PUBLICATIONS AND PRESENTATIONS

Blue, B. et. al. (2003). Plasma Wakefield Acceleration of an Intense Positron Beam. Physical Review Letters.

Blue, B. (2002). Acceleration of a Relativistic Positron Beam in the Plasma Wakefield Accelerator. Talk presented at the American Physical Society Division of Plasma Physics Meeting, Orlando, FL.

- Blue, B. (2001). Impact Ionization of a 30 GeV Electron Beam in Helium, Argon, and Nitrogen. Presentation at the American Physical Society Division of Plasma Physics Meeting, Long Beach.
- Blue, B. et.al. (2001). Test of the Electron Hose Instability in the E157 Experiment. Proceedings of the 2001 Particle Accelerator Conference, Chicago.
- Blue, B (2000). Electron Hose Instability in the E157 Experiment. Presentation at the American Physical Society Division of Plasma Physics Meeting, Quebec.
- Blue, B. (2000). Centroid Oscillations in the E157 Plasma Wakefield Accelerator. Talk presented at the Advanced Accelerator Conference, Albuquerque, NM.
- Clayton, C. et.al. (2002) Transverse envelope dynamics of a 28.5-GeV electron beam in a long plasma. *Physical Review Letters* April 15.
- Hogan, M. et.al. (2000). E-157: A 1.4-m-long plasma wake field acceleration experiment using a 30 GeV electron beam from the Stanford Linear Accelerator Center Linac. *Physics of Plasmas*, vol.7, (no.5), p.2241-8.
- Hogan, M. et. al. (2003). Ultra-Relativistic Positron-Beam Transport through Meter-Scale Plasmas. *Physical Review Letters*.
- Joshi, C. et. al. (2002). High energy density plasma science with an ultrarelativistic electron beam. *Physics of Plasmas*, Vol. 9, 1845.
- Lee, S. et. al. (2002). Energy Doubler for a Linear Collider. *Physical Review Letters Special Topics Accelerators and Beams*, Vol 5. 011001.
- Muggli, P. et.al. (2001). Boundary effects: Refraction of a particle beam. *Nature*, 411 p.43, May 3.
- Muggli, P. et. al. (2001). Collective refraction of a beam of electrons at a plasma-gas interface. *Physical Review Letters Special Topics Accelerators and Beams*, Vol 4. 091301.
- O'Connell, C. et. al. (2002). Dynamic focusing of an electron beam through a long plasma. *Physical Review Letters Special Topics Accelerators and Beams*, Vol 5. 121301.

Tochitsky, S.Ya et.al., (1999). Amplification of two-wavelength CO₂ laser pulses to terawatt level. Proceedings of the International Conference on Lasers, Quebec.

Wang, S. et.al. (2002) X-Ray Emission from Betatron Motion in a Plasma Wiggler. Physical Review Letters April 1.

ABSTRACT OF THE DISSERTATION

Plasma Wakefield Acceleration of an Intense Positron Beam

by

Brent Edward Blue

Doctor of Philosophy in Electrical Engineering

University of California, Los Angeles, 2003

Professor Chandrasekhar J. Joshi, Chair

The Plasma Wakefield Accelerator (PWFA) is an advanced accelerator concept which possess a high acceleration gradient and a long interaction length for accelerating both electrons and positrons. Although electron beam-plasma interactions have been extensively studied in connection with the PWFA, very little work has been done with respect to positron beam-plasma interactions. This dissertation addresses three issues relating to a positron beam driven plasma wakefield accelerator. These issues are a) the suitability of employing a positron drive bunch to excite a wake; b) the transverse stability of the drive bunch; and c) the acceleration of positrons by the plasma wake that is driven by a positron bunch. These three issues are explored first through computer simulations and then through experiments. First, a theory is developed on

the impulse response of plasma to a short drive beam which is valid for small perturbations to the plasma density. This is followed up with several particle-in-cell (PIC) simulations which study the experimental parameter (bunch length, charge, radius, and plasma density) range. Next, the experimental setup is described with an emphasis on the equipment used to measure the longitudinal energy variations of the positron beam. Then, the transverse dynamics of a positron beam in a plasma are described. Special attention is given to the way focusing, defocusing, and a tilted beam would appear to be energy variations as viewed on our diagnostics. Finally, the energy dynamics imparted on a 730 μm long, 40 μm radius, 28.5 GeV positron beam with 1.2×10^{10} particles in a 1.4 meter long $0\text{-}2 \times 10^{14}$ e^-/cm^3 plasma is described. First the energy loss was measured as a function of plasma density and the measurements are compared to theory. Then, an energy gain of 79 ± 15 MeV is shown. This is the first demonstration of energy gain of a positron beam in a plasma and it is in good agreement with the predictions made by the 3-D PIC code. The work presented in this dissertation will show that plasma wakefield accelerators are an attractive technology for future particle accelerators.

1 Introduction

This chapter is an introduction to beam driven plasma wakefield accelerators. The fundamental concepts of the mechanisms inside the plasma wakefield accelerator will be covered in the first section. The next section will describe how our experiment was conceived and what its goals were. Next, this chapter will address the differences between electron and positron driven plasma wakefield accelerators. Finally, this chapter will conclude with a review of previous work done on plasma wakefield accelerators.

1.1 Plasma wakefield accelerator

Plasma wakefield accelerators utilize a relativistically propagating electron plasma wave to accelerate particles [1]. They are very attractive because they can sustain accelerating fields on the order of the non-relativistic wavebreaking field E_0 [2]. This field is roughly that which would be generated by 100% sinusoidal modulation of the plasma electron density at the plasma wavelength.

$$E_0 [V/m] \approx 96 \sqrt{n_0 [cm^{-3}]} \quad (1.1)$$

For instance, the accelerating gradient at a density of $10^{16} cm^{-3}$ is approaching 10 GeV/m. This is significantly greater than the 25-100 MeV/m used in current RF accelerators [3]. Different methods exist for generating the plasma wave. The three most common are the laser beatwave (PBWA) [4, 5, 6], laser wakefield (LWFA) [7, 8,

9], and particle beam driven wakefield (PBWA) [10, 11, 12]. The laser driven methods are very attractive since compact, table top size lasers can generate very high accelerating gradients (~ 100 GeV/m). The setback is that the interaction length for acceleration is on the order of the Raleigh length of the laser beam (>1 mm). On the other hand, particle beams can sustain the high accelerating gradients over meter scale distances since the Raleigh length of the beam can be 10's of meters. A major design requirement of accelerators is high energy which implies that both a high gradient and a long interaction length are needed. This is a reason why beam driven plasma wakefield accelerators are very attractive as an advanced accelerator concept. The physic's issues of a positron beam driven plasma wakefield accelerator are the subject of this dissertation.

1.2 Electron beam driven plasma wakefield accelerators

Conceptually, the plasma wakefield accelerator (PWFA) operating in the “blow-out” regime (beam density is greater than the plasma density) is a very simple device. First, an electron beam is injected into a neutral plasma. The space-charge field of the beam rapidly expels the plasma electrons. The plasma ions, which are much more massive than the plasma electrons, remain stationary during the time scale of our bunch length. Since the beam density is greater than the plasma density, an ion column is formed which is devoid of plasma electrons. The expelled plasma electrons now witness the space-charge field of the ion column and are pulled back in towards

the beam axis. Due to their momentum, the plasma electrons overshoot the axis. These plasma electrons now oscillate on axis with a frequency which is approximately the characteristic plasma frequency ω_p .

$$\omega_p = \sqrt{\frac{4\pi n_p e^2}{m_e}} \quad (1.2)$$

Here, m_e , e , and n_p are the electron mass, the elementary charge, and the plasma density respectively. These oscillating plasma electrons form a density modulation as viewed on axis. This density modulation gives rise to a very high electric field which is used to accelerate the beam electrons. These dynamics are schematically shown in figure 1.1.1.

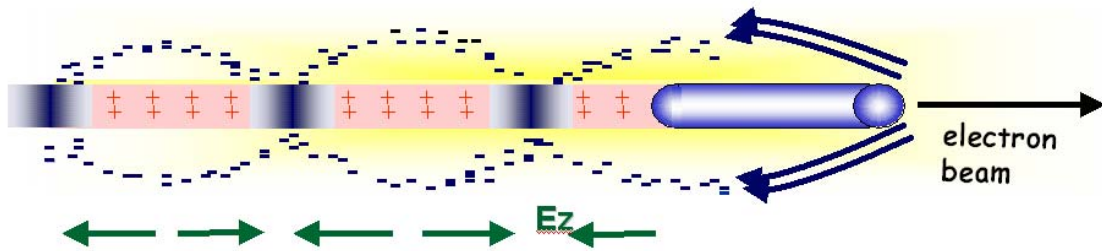


Figure 1.2.1 Wakefield generated by an electron beam

1.3 Regimes of electron beam driven PWFAs

In general, the electron beam-plasma interaction can be characterized by four regimes of propagation [13]. These regimes are defined by the relative densities of the

plasma and the beam and the ratio of the plasma wavelength to the beam spot size.

The four conditions are outlined in table 1.3.1.

Regime	Condition	E162 Condition
Unfocused	$n_p < n_b / \gamma^2$	$n_p < 3.6 \times 10^5 \text{ e}^- / \text{cm}^3$
Ion-Focused	$n_p < n_b$	$n_p < 1.1 \times 10^{15} \text{ e}^- / \text{cm}^3$
Magnetically Self-Focused	$n_p > n_b \ \& \ \sigma_r \ll \lambda_p$	$n_p > n_b \ \& \ \sigma_r \ll 2.4 \text{mm}$
Current Neutralization	$n_p > n_b \ \& \ \sigma_r > \lambda_p$	$n_p > n_b \ \& \ \sigma_r > 2.4 \text{mm}$

Table 1.3.1 Regimes of electron beam propagation

As seen in the table above, two regimes were not practically explored in our experiment. They were the unfocused regime and the current neutralization regime. The unfocused regime is where the plasma density is very low compared to the beam density. The plasma density is insufficient to significantly alter the in vacuum balance between the repulsive space charge electric field and the attractive self-generated magnetic field, and thus it has no effect on the beam propagation. In practical terms, our observation of this regime was when we did not generate any plasma. This “plasma off” case was observed to have no effect on the beam. The current neutralization regime was not accessible since we could not generate an electron beam which had a radius greater than a plasma wavelength. The characteristic feature of this regime is that the plasma return current, which is a reaction to the beam current, can only respond to features which are on the order of the plasma wavelength. Since

the radius is larger than the plasma wavelength in this regime, the return current will flow through the beam and neutralize it. The plasma density, since it is overdense, is sufficient to neutralize the beam's space charge electric field. The focusing magnetic field will be diminished due to the plasma currents flowing through the beam.

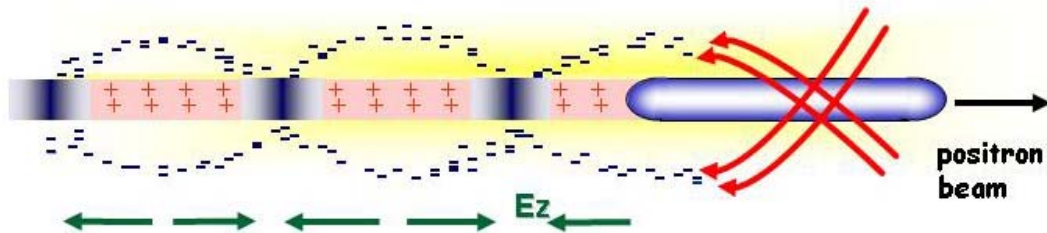
The remaining two regimes, ion-focused and magnetically self-focused, were accessible in our experiment. The bulk of the beam propagated in the ion-focused regime. In this regime, the beam's radial electric field expels all plasma electrons from a volume. The radius of this volume is approximated by the radius at which the beam's electric field is exactly canceled by the electric field of a pure ion column with a density equal to the initial plasma density. This radius is typically much larger than the radius of the beam. When an electron beam is propagating in free space in equilibrium, the repulsive space-charge electric field is canceled by self-focusing magnetic field generated by the beam's own current. When the beam propagates through the ion column, the space charge field of ion column focuses down the beam electrons. The magnetically self-focused regime is similar to the ion focused regime, except the beam density is not sufficient to expel all plasma electrons. This results in a complete neutralization of the beam's space charge field. With the repulsive space charge field neutralized, the magnetic force dominates and pinches down the beam. One consequence of this regime is that the focusing force will be non-uniform due to radial variations in the ion/plasma density [13]. This regime is characteristically different from the current neutralization case in that the plasma return currents do not

flow through the beam, and thus they do not diminish the magnetic focusing force. As seen in the above table, this regime is accessed when the beam density is less than the plasma density. Although the peak beam density is greater than the plasma density, the beam densities at the head and tail of the beam are lower, and thus in this regime.

1.4 Positron Beam Driven PWFAs

The response of a plasma to a dense beam of relativistic positrons is qualitatively different from that of a similar electron beam propagating through a plasma. When an ultrarelativistic, highly focused ($\sigma_r \ll c/\omega_p$) positron beam enters an underdense plasma ($n_b > n_p$), the in-vacuum balance between the beam's space-charge defocusing field and self-magnetic focusing field is modified by the highly mobile plasma electrons that are pulled in neutralizing the excess space charge of the positron beam. Here σ_r , c , ω_p , n_b , n_p are the beam radius, speed of light, plasma frequency, beam density, and plasma density respectively. The degree of neutralization depends not only on the plasma density, but also on the longitudinal position along the positron bunch. As plasma electrons from various radii arrive on the axis of the beam at various times and overshoot, they create a wakefield structure that has complex longitudinal and transverse electric field components [14]. If the r.m.s. bunch length σ_z is approximately $\pi c/\omega_p$, then the bulk of the positrons do work in pulling in the plasma electrons and therefore lose energy to the wakefield. However, there are a

significant number of particles in the tail of the beam where the wakefield has changed sign and are therefore accelerated.



1.4.1 Wakefield generated by a positron beam

1.5 Regimes of positron beam driven PWFAs

The regimes of propagation for a positron beam are similar to the electron beam case except for a few key differences. First, there is no analogy to the ion-focused regime for the positron case. This is because the positron beam pulls in plasma electrons, not expelling them as in the electron beam case. If the beam density is greater than the plasma density, the positron beam pulls in plasma electrons from greater and greater radii until its field is neutralized. The final difference between the electron and positron regimes is that the magnetically self focused and current neutralization regimes only depend on the beam radius in the positron case.

Regime	Condition	E162 Condition
Unfocused	$n_p < n_b / \gamma^2$	$n_p < 3.6 \times 10^5 e^- / cm^3$
Magnetically Self-Focused	$\sigma_r \ll \lambda_p$	$\sigma_r \ll 2.4mm$
Current Neutralization	$\sigma_r > \lambda_p$	$\sigma_r > 2.4mm$

Table 1.5.1 Regimes of positron beam propagation

As seen in the table, the positron beam propagated through the plasma in the magnetically self-self focused regime. Two important features of this regime are as follows. First, the transport of the beam can be theoretically approximated by a linear theory in which the beam is assumed to be point like ($\sigma_r, \sigma_z \ll \lambda_p$) and that the beam density is a perturbation to the plasma density. This is because although the beam density is greater than the initial electron plasma density, the positron beam pulls in plasma electrons from large radii, thus increasing the electron plasma density on axis. The above theory and simulations will be discussed in the next chapter. The second feature of this regime is the non-uniform focusing force imparted by the plasma on the beam. The nonuniform focusing force was demonstrated by our collaboration in a paper by Hogan et al [14] and it will also be discussed in Chapter 5.

1.6 Review of previous PWFA work

The basic mechanisms behind beam driven plasma wakefield accelerators was developed by Chen et. al. in 1985 [16]. He proposed using a point like drive beam ($\sigma_r \ll \lambda_p$) in the linear regime where the beam density is a small perturbation to the electron plasma density. Here, σ_r is the beam radius and λ_p is the plasma wavelength. This work was then continued by considering finite radius, disk like beams [17]. Ruth et. al. [18] showed that in the linear regime, the transformer ratio (the ratio of the energy gain to the initial beam energy) must be less than 2. Next, it was proposed to shape the drive bunch so that this transformer ratio limit could be exceeded [19].

Further advances were made when Rosenzweig proposed operating in the nonlinear regime where the beam density is greater than plasma density [20]. He showed that the transformer ratio in this regime could be higher than 2. He went on to show that this “blowout” regime has several benefits in addition to its higher transformer ratio [21].

The first experimental work on PWFAs was reported by Berezin et. al. in 1994 [12]. They demonstrated 250 keV/m acceleration in a 20-100 cm $10^{11} e^- / cm^3$ plasma in which the wakefield was excited by an 0.4 nC, 2 MeV electron bunch train. This was followed up by work by Rosenzweig et. al. They did a series of experiments with a 21 MeV, 7 ps, 4 nC drive beam in a 33cm $(0.4-7) \times 10^{12} e^- / cm^3$ plasma in which both linear [22] and nonlinear [10] wakefields were observed. A maximum energy

gain of 200 keV was observed and a maximum acceleration gradient of 5 MeV/m was witnessed. Further work in Japan used a 500 MeV, 10 ps, 10 nC electron beam in a 1 meter long $(2-8)\times 10^{12} e^- / cm^3$ plasma. Nakajima et al. [23] demonstrated a 30 MeV/m acceleration gradient and Nakanishi et al. [24] used bunches from two identical linacs for the drive and trailing beams.

Recent work at the Stanford Linear Accelerator Center used 28.5 GeV, 3 nC, 2 ps electron and positron beams in a 1.4 meter long $(0-4)\times 10^{14} e^- / cm^3$ plasma. Several important results stemmed from this experiment which include: Electron beam focusing by Clayton et. al. [25], Dynamic focusing of an electron beam by O'Connell et. al. [26], Lack of the electron hosing instability by Blue [27], 150 MeV/m acceleration of an electron beam by Muggli et. al. [28], focusing of a positron beam by Hogan et. al. [15], and 56 MeV/m acceleration of a positron beam by Blue et. al. [29]. The last result is the subject of this dissertation.

1.7 Summary of the dissertation

This dissertation addresses three issues relating to a positron beam driven plasma wakefield accelerator. These issues are a) the suitability of employing a positron drive bunch to excite a wake; b) the transverse stability of the drive bunch; and c) the acceleration of positrons by the plasma wake that is driven by a positron

bunch. These three issues are explored first through computer simulations and then through experiments.

Chapter 2 presents a theory on the impulse response of plasma to a short drive beam which is valid for small perturbations to the plasma density. This is followed up with several particle-in-cell (PIC) simulations which study the experimental parameter (bunch length, charge, radius, and plasma density) range. The theory and simulation chapter is concluded by a full 3-D OSIRIS simulation which uses nearly identical parameters to the E162 experiment.

Chapter 3 describes the E162 experiment which took place at the Stanford Linear Accelerator Center. The experimental setup is described with an emphasis on the equipment used to measure the longitudinal energy variations of the positron beam. The equipment and diagnostics include the plasma source, the imaging spectrometer, the optical transition radiation detector, and the time-integrated and time-resolved Cherenkov diagnostic.

In chapter 4 the transverse dynamics of a positron beam in a plasma are described. Special attention is given to the way focusing, defocusing, and a tilted beam would appear to be energy variations as viewed on our diagnostics.

Chapter 5 details the energy dynamics imparted on a 730 μm long, 40 μm radius, 28.5 GeV positron beam with 1.2×10^{10} particles in a 1.4 meter long $0.2 \times 10^{14} \text{ e}^- / \text{cm}^3$ plasma. First the energy loss was measured as a function of plasma density and the measurements are compared to theory. Then, an energy gain of $79 \pm 15 \text{ MeV}$ is

shown. This is the first demonstration of energy gain of a positron beam in a plasma and it is in good agreement with the predictions made by the 3-D PIC code.

The work presented in this dissertation will show that plasma wakefield accelerators are an attractive technology for future particle accelerators.

2 Theory and Simulations

This chapter gives an introduction to the theory of a positron beam in a plasma. First, an analytical expression is derived for the impulse response of a plasma. This is expanded into the response of a plasma to a Gaussian pulse. Finally, experimental predictions and scaling laws will be explored through particle-in-cell (PIC) simulations.

2.1 Plasma impulse response (linear theory)

Although the interaction of a dense ($n_b > n_p$), short ($\sigma_z \sim \lambda_p$) positron beam with a plasma is inherently nonlinear, we can use the linear theory (Katsouleas *et al.*, 1987) which predicts the plasma response to either a short electron or positron beam as a guide to interpret the PIC code results. Here n_b , n_p , σ_z , and λ_p are the beam density, plasma density, beam longitudinal characteristic length, and the wavelength of the plasma response respectively. Here the beam induces a small perturbation in the plasma whose response can be calculated if we assume that the beam is infinitely short.

The starting point for any electromagnetic problem is to begin with Maxwell's equations.

$$\nabla \cdot \vec{E} = 4\pi\rho \quad (2.1)$$

$$\nabla \cdot \vec{B} = 0 \quad (2.2)$$

$$\nabla \times \vec{E} = -\frac{1}{c} \frac{\partial \vec{B}}{\partial t} \quad (2.3)$$

$$\nabla \times \vec{B} = \frac{4\pi}{c} \vec{J} + \frac{1}{c} \frac{\partial \vec{E}}{\partial t} \quad (2.4)$$

Since we are dealing with charged particles which have a mass, we add the equation of motion for electrons.

$$\vec{F} = m_e \vec{a} = q\vec{E} \quad (2.5)$$

$$\vec{a} = \frac{\partial \vec{v}}{\partial t} = -\frac{e\vec{E}}{m_e} \quad (2.6)$$

Finally, we add the continuity equation which states that the change in density in a volume is equal to the flow of particles into or out of the volume.

$$\frac{dn}{dt} + \nabla \cdot n\vec{v} = 0 \quad (2.7)$$

Additionally, the current of the plasma is given by

$$\vec{J} = qn\vec{v} \quad (2.8)$$

The above equations are exact in the limit of nonrelativistic motion. Due to the complexity of plasmas, a rigorous analytic solution cannot be made. Therefore, we make viable approximations in order to gain insight. First we approximate the drive beam as a delta function. This will allow us to calculate the impulse response of the plasma.

$$\rho_{Beam} = \frac{q}{c} \delta(r) \delta\left(t - \frac{z}{c}\right) \quad (2.9)$$

Next, we linearize the equations where the first order terms are small corrections, or perturbations, to the initial values.

$$n = n_0 + n_1 \quad (2.10)$$

$$\vec{v} = \vec{v}_0 + \vec{v}_1 = \vec{v}_1 \quad \vec{v}_0 = 0 \quad (2.11)$$

$$\vec{E} = \vec{E}_0 + \vec{E}_1 = \vec{E}_1 \quad \vec{E}_0 = 0 \quad (2.12)$$

$$\vec{B} = \vec{B}_0 + \vec{B}_1 = \vec{B}_1 \quad \vec{B}_0 = 0 \quad (2.13)$$

We now insert the linear quantities 2.10-2.13 into equations 2.1-2.8 and solve for the first order terms.

$$\nabla \cdot \vec{E}_1 = 4\pi\rho_{Beam} - 4\pi en_1 \quad (2.14)$$

$$\nabla \cdot \vec{B}_1 = 0 \quad (2.15)$$

$$\nabla \times \vec{E}_1 = -\frac{1}{c} \frac{\partial \vec{B}_1}{\partial t} \quad (2.16)$$

$$\nabla \times \vec{B}_1 = \frac{4\pi}{c} \vec{J}_1 + \frac{1}{c} \frac{\partial \vec{E}_1}{\partial t} \quad (2.17)$$

$$\frac{\partial \vec{v}_1}{\partial t} = -\frac{e\vec{E}_1}{m_e} \quad (2.18)$$

$$\frac{dn_1}{dt} + n_0 \nabla \cdot \vec{v}_1 = 0 \quad (2.19)$$

$$\vec{J}_1 = qn_0 \vec{v}_1 \quad (2.20)$$

The first goal is to solve for the density perturbation as a function of the impulse response. We take the time derivative of the linearized continuity equation 2.19.

$$\frac{\partial^2 n_1}{\partial t^2} + n_0 \nabla \cdot \frac{d\vec{v}_1}{dt} = 0 \quad (2.21)$$

The acceleration is given by the linearized equation of motion 2.18.

$$\frac{\partial^2 n_1}{\partial t^2} - \frac{en_0}{m_e} \nabla \cdot \vec{E}_1 = 0 \quad (2.22)$$

The divergence of the electric field is known from equation 2.14.

$$\frac{\partial^2 n_1}{\partial t^2} - \frac{en_0}{m_e} (4\pi\rho_{Beam} - 4\pi en_1) = 0 \quad (2.23)$$

This equation is simplified by combining terms into a parameter known as the plasma frequency.

$$\omega_p = \sqrt{\frac{4\pi n_0 e^2}{m_e}} \quad (2.24)$$

$$\frac{\partial^2 n_1}{\partial t^2} + \omega_p^2 n_1 = \omega_p^2 \frac{q}{ec} \delta(r) \delta\left(t - \frac{z}{c}\right) \quad (2.25)$$

We can solve this differential equation by using the Laplace transform of a system which is initially at rest.

$$s^2 \mathbf{L} \{n_1\} - sn_1(0) - n_1'(0) + \omega_p^2 \mathbf{L} \{n_1\} = \omega_p^2 \delta(r) \frac{q}{ec} \quad (2.26)$$

$$n_1(0) = n_1'(0) = 0 \quad (2.27)$$

Solve for the density and take the inverse Laplace transform.

$$\mathcal{L}\{n_1\} = \frac{q}{ec} \delta(r) \frac{\omega_p^2}{s^2 + \omega_p^2} \quad (2.28)$$

$$n_1 = \mathcal{L}^{-1} \left\{ \frac{q}{ec} \delta(r) \frac{\omega_p^2}{s^2 + \omega_p^2} \right\} \quad (2.29)$$

$$n_1 = \omega_p \frac{q}{ec} \delta(r) \sin \left[\omega_p \left(t - \frac{z}{c} \right) \right] U \left(t - \frac{z}{c} \right) \quad (2.30)$$

This equation gives us the density as it is perturbed by the beam. The function $U(t)$ is Heavyside function which means that the plasma is not perturbed until after the beam passes. We now solve for the electric field as a function of the perturbed density. Take the curl of equation 2.16.

$$\nabla \times \nabla \times \vec{E}_1 = -\frac{1}{c} \frac{\delta}{\delta t} \nabla \times \vec{B}_1 \quad (2.31)$$

Apply the vector identity for the curl of a curl of a vector and insert equation 3.17 for the curl of the magnetic field.

$$\nabla (\nabla \cdot \vec{E}_1) - \nabla^2 \vec{E}_1 = -\frac{4\pi}{c^2} \frac{\delta \vec{J}_1}{\delta t} - \frac{1}{c^2} \frac{\partial^2 \vec{E}_1}{\partial t^2} \quad (2.32)$$

Take the time derivative of the linearized current equation 2.20.

$$\frac{\delta \vec{J}_1}{\delta t} = -en_0 \frac{\delta \vec{v}_1}{\delta t} = \frac{e^2 n_0}{m_e} \vec{E}_1 \quad (2.33)$$

Insert equations 2.33, 2.14, and 2.9 into equation 2.32 and rearrange terms.

$$\left(\frac{\partial^2}{\partial t^2} - c^2 \nabla^2 \right) \vec{E}_1 = -\frac{4\pi e^2 n_0}{m_e} \vec{E}_1 - c^2 \nabla (4\pi \rho_{Beam} - 4\pi e n_1) \quad (2.34)$$

$$\left(\frac{\partial^2}{\partial t^2} - c^2 \nabla^2 + \omega_p^2\right) \vec{E}_1 = -4\pi c q \omega_p \delta(r) U\left(t - \frac{z}{c}\right) \nabla \left[\sin \left[\omega_p \left(t - \frac{z}{c}\right) \right] \right] \quad (2.35)$$

$$\left(\frac{\partial^2}{\partial t^2} - c^2 \nabla^2 + \omega_p^2\right) \vec{E}_1 = -4\pi q \omega_p^2 \delta(r) U\left(t - \frac{z}{c}\right) \cos \left[\omega_p \left(t - \frac{z}{c}\right) \right] \quad (2.36)$$

We are interested in E_z , the longitudinal accelerating and decelerating field. To do this, we break the gradient term in its longitudinal and transverse components.

$$\nabla^2 = \nabla_{\perp}^2 + \frac{\partial^2}{\partial z^2} \quad (2.37)$$

Because we are interested in relativistic drive particle beams, the velocity is approximately the speed of light. Therefore, the time derivative can be replaced with a special derivative.

$$\frac{\partial^2}{\partial t^2} = c^2 \frac{\partial^2}{\partial z^2} \quad (2.38)$$

A further quantity is the plasma wave number.

$$k_p^2 \equiv \frac{\omega_p^2}{c^2} \quad (2.39)$$

This results in the modified Helmholtz equation for the electric field driven by an impulse.

$$\left(\nabla_{\perp}^2 - k_p^2\right) \vec{E}_1 = 4\pi q k_p^2 \delta(r) U\left(t - \frac{z}{c}\right) \cos \left[\omega_p \left(t - \frac{z}{c}\right) \right] \quad (2.40)$$

This equation has still has a delta function in it which relates to the strength of the field off axis. To solve for this, we use the Green's function response of the Helmholtz equation.

$$\left(\nabla_r^2 - k_p^2\right)G(r, r') = \delta(r) \quad (2.41)$$

We use a cylindrical geometry due to the symmetry of our system.

$$\nabla^2\phi = \frac{1}{\rho} \frac{\partial}{\partial\rho} \left(\rho \frac{\partial\phi}{\partial\rho} \right) + \frac{1}{\rho^2} \frac{\partial^2\phi}{\partial\phi^2} + \frac{\partial^2\phi}{\partial z^2} \quad (2.42)$$

Expanding equation 2.41 with equation 2.42 and using the delta function response in cylindrical geometry with no angular or longitudinal dependence.

$$\frac{1}{\rho} \frac{d}{d\rho} \left(\rho \frac{dG(\rho)}{d\rho} \right) - k_p^2 G(\rho) = \frac{1}{2\pi\rho} \delta(\rho) \quad (2.43)$$

Solutions to equation 2.43 will be of the form of solutions to the homogeneous equation.

$$\frac{1}{\rho} \frac{d}{d\rho} \left(\rho \frac{dG(\rho)}{d\rho} \right) - k_p^2 G(\rho) = 0 \quad (2.44)$$

Solutions to the modified Bessel differential equation take the form of a summation of modified Bessel functions.

$$G(\rho) = \sum_{n=-\infty}^{+\infty} c_1 I_n(k_p \rho) + c_2 K_n(k_p \rho) \quad (2.45)$$

Multiply equation 2.43 by ρ to put it in this form of Sturm-Liouville differential equation.

$$\rho \frac{\partial^2 G}{\partial \rho^2} + \frac{\partial G}{d\rho} - k_p^2 G = \frac{1}{2\pi} \delta(\rho) \quad (2.46)$$

This type of differential equation has known solutions.

$$p(x) \frac{d^2 y}{dx^2} + \frac{dp}{dx} \frac{dy}{dx} - q(x)y = f(x) \quad (2.47)$$

$$p(\rho) = \rho \quad (2.48)$$

These solutions will take the form of

$$G(\rho) = A_1 y_1(\rho) \quad 0 \leq \rho < \rho' \quad (2.49)$$

$$G(\rho) = A_2 y_2(\rho) \quad \rho' < \rho < \infty \quad (2.50)$$

$$G(\rho) = \frac{y_2(\rho')}{p(\rho')W(\rho')} y_1(\rho) \quad 0 \leq \rho < \rho' \quad (2.51)$$

$$G(\rho) = \frac{y_1(\rho')}{p(\rho')W(\rho')} y_2(\rho) \quad \rho' < \rho < \infty \quad (2.52)$$

$W(x)$ is called the Wronskian and it is given by

$$W(\rho') = y_1(\rho')y_2'(\rho') - y_2(\rho')y_1'(\rho') \quad (2.53)$$

Boundary conditions are that the field is finite at the origin and zero at infinity

$$G(0) = \text{finite} \quad G(\infty) = 0 \quad (2.54)$$

Apply these boundary conditions to the general equation of the solutions 2.45.

$$y_1 = \sum_{m=-\infty}^{+\infty} I_m(k_p \rho) \quad (2.55)$$

$$y_2 = \sum_{m=-\infty}^{+\infty} K_m(k_p \rho) \quad (2.56)$$

The Wronskian of a Bessel function is

$$J_n(\alpha\rho)Y_n'(\alpha\rho) - Y_n(\alpha\rho)J_n'(\alpha\rho) = \frac{2}{\pi\alpha\rho} \quad (2.57)$$

To find the Wronskian of the modified Bessel functions we expand the modified Bessel functions of the first and second type into their form in terms of normal Bessel functions.

$$K_m(\alpha\rho) = \frac{\pi}{2} j^{m-1} [J_m(-j\alpha\rho) - jY_m(-j\alpha\rho)] \quad (2.58)$$

$$I_m(\alpha\rho) = j^m J_m(\alpha\rho) \quad (2.59)$$

The modified Wronskian is now

$$W_m(\alpha\rho) = I_m(\alpha\rho)K_m'(\alpha\rho) - K_m(\alpha\rho)I_m'(\alpha\rho) \quad (2.60)$$

Expanding the modified Bessel functions gives

$$\begin{aligned} & \frac{\pi}{2} j^{2m-1} \alpha [J_m(-j\alpha\rho)(J_m'(-j\alpha\rho) - jY_m'(-j\alpha\rho)) \\ & - (J_m(-j\alpha\rho) - jY_m(-j\alpha\rho))J_m'(-j\alpha\rho)] \end{aligned} \quad (2.61)$$

Canceling similar terms and inserting the solution for the Wronskian of a Bessel function.

$$\frac{-\pi}{2} j^{2m} \alpha [J_m(-j\alpha\rho)Y_m'(-j\alpha\rho) - Y_m(-j\alpha\rho)J_m'(-j\alpha\rho)] \quad (2.62)$$

$$\frac{-\pi}{2} j^{2m} \alpha \frac{2}{\pi j\alpha\rho} \quad (2.63)$$

$$W_m(k_p \rho) = -\frac{j^{2m-1}}{\rho} \quad (2.64)$$

Insert 2.64, 2.55, 2.56, and 2.48 into equation 2.51.

$$G(\rho) = \frac{-1}{\pi^2 j^{2m-1}} \sum_{m=-\infty}^{+\infty} I_m(k_p \rho') K_m(k_p \rho) \quad (2.65)$$

Again we break the modified Bessel functions down into their normal Bessel function components.

$$G(\rho) = -\frac{1}{2\pi} \sum_{m=-\infty}^{+\infty} J_m(-jk_p \rho') (J_m(-jk_p \rho) - jY_m(-jk_p \rho)) \quad (2.66)$$

The following two identities for the infinite sums of Bessel functions are used to reduce equation 2.66.

$$\sum_{m=-\infty}^{+\infty} J_m(k_p \rho') J_m(k_p \rho) = J_0(k_p |\rho - \rho'|) \quad (2.67)$$

$$\sum_{m=-\infty}^{+\infty} J_m(k_p \rho') Y_m(k_p \rho) = Y_0(k_p |\rho - \rho'|) \quad (2.68)$$

This results in the 2-D Green's function response of the scalar Helmholtz equation in cylindrical geometry.

$$G(\rho) = -\frac{1}{2\pi} (J_0(-jk_p \rho) - jY_0(-jk_p \rho)) = -\frac{1}{2\pi} K_0(k_p \rho) \quad (2.69)$$

Substituting equation 2.69 into equation 2.40 give the longitudinal electric field which results from a beam approximated by a delta function.

$$E_Z = -2qk_p^2 K_0(k_p r) U\left(t - \frac{z}{c}\right) \cos\left[\omega_p\left(t - \frac{z}{c}\right)\right] \quad (2.70)$$

The response of the plasma various bunch distributions can be found by integrating the Green's function response over the charge distribution.

$$E_Z(r, \theta, \zeta) = -2k_p^2 \int_{-\infty}^{\zeta} \partial \zeta' \int_0^{\infty} \partial r' \int_0^{2\pi} \partial \theta' \rho_{Beam}(r', \theta', \zeta') K_0(k_p r') \cos k_p \zeta' \quad (2.71)$$

The peak accelerating field which results from a Gaussian distribution is given by

$$eE_Z = \sqrt{n_p} \frac{n_b}{n_p} \frac{\sqrt{2\pi} k_p \sigma_z e^{-k_p^2 \sigma_z^2 / 2}}{1 + \frac{1}{k_p^2 \sigma_r^2}} \sin k_p (z - ct) \quad (eV/cm) \quad (2.72)$$

Several important scaling laws can be extrapolated from this equation. First, the wakefield excited by the bunch oscillates sinusoidally with a frequency determined by the plasma density and its phase velocity travels at the speed of light. Second, the accelerating gradient increases linearly with increasing charge. This is because the increased charge increases the strength of the beam space charge field which in turn drives the plasma wave harder. Third, the fields excited by electrons and positron beams are equal in magnitude but opposite in phase. Finally, the field will be maximized for a value of $k_p \sigma_z = \sqrt{2}$. This is because the equation for the field is of the form of

$$f(x) = x e^{-x^2/2} \quad (2.73)$$

To find the maxima and minima of this function, we take its derivative and set it equal to zero.

$$f'(x) = (1 - x^2)e^{-x^2/2} = 0 \quad (2.74)$$

This has solutions of $x = \sqrt{2}$ and $x = \infty$. To find whether these solutions are maxima or minima, we calculate the value of the second derivative with the above solutions.

$$f''(x) = x(x^2 - 3)e^{-x^2/2} \quad (2.75)$$

We see that $f'(\sqrt{2}) < 0$ which means that that point is a maximum, and $f'(\infty) > 0$ which mean that that point is a minimum. This is why the field is maximized when $k_p \sigma_z = \sqrt{2}$. These scaling laws were derived used approximations in the linear regime. For a more complete analysis, we turn to particle-in-cell simulations.

2.2 Scaling laws explored through PIC simulations for a positron beam

Although the scaling laws inferred from Eqn. 2.72 in the previous section are useful, the approximations made are often not entirely valid as in the current experiments that are being carried out at the Stanford Linear Accelerator Center (SLAC). For instance, while the linear theory assumes that the density perturbation induced by the beam is typically small, the beam density can exceed the plasma density over most of the length of the bunch in current experiments and therefore linear theory can break down. The dynamics of the plasma electrons that are being

perturbed by the space charge field of the positron beam are extremely complicated. As plasma electrons from different radii outside of the bunch are pulled in by the space charge field of the positron beam they arrive at different times at different longitudinal locations within the beam. This mandates the use of PIC simulations in order to gain insight beyond that which was obtained from linear theory. The beam and plasma parameters used in the simulations will be the nominal parameters used in the SLAC E162 experiment (Joshi *et al.*, 2002) which are listed in Table 1.

Nominal Experimental Parameter	Value
Positron Beam Energy	28.5 GeV
Number of Beam Particles	$1.2 \times 10^{10} e^+$
Beam R.M.S. Radius σ_r	$40 \mu m$
Beam R.M.S Length σ_z	$730 \mu m$
Plasma Density n_p	$1.8 \times 10^{14} e^- / cm^3$

Table 2.2.1 Nominal Beam Parameters

The PIC code OOPIC (Bruhwiler *et al.*, 2001) was used to obtain the fields generated by the positron beam. *Unless otherwise stated, the parametric study reported in this paper was carried out by changing only one parameter in Table 1 while holding other parameters constant.* OOPIC is a fully-explicit, 2-D cylindrical

geometry code. Typical simulation parameters were radial and longitudinal grid sizes $\Delta r = \Delta z = 20 \mu m$, time step $\Delta t = 14 fs$, and a simulation box 1mm wide and 8mm long. The wakefield was measured after the beam fully propagated into the plasma ($\sim 10 \sigma_z$). At this point in the plasma, the wakefields are more or less fully excited and do not change shape or magnitude (in the beam frame) as the drive beam propagates further into the plasma although parts of the beam itself can dramatically focus and defocus in the transverse direction in response to the wakefields (Hogan *et al.*, 2003). In the longitudinal direction, there is energy gain or loss by positrons located at different phases of the beam, but at an initial energy of 28.5 GeV, the beam is “stiff” and the positrons do not physically move in the longitudinal direction. As the plasma electrons are attracted and pulled into the beam, the peak electron density within the bunch can exceed the beam density even though $n_b > n_p$, thus neutralizing the beam’s space charge and setting up strong transverse and longitudinal wakefields. As mentioned in the introduction, we will discuss the scaling of the longitudinal field only in this paper as a function of different beam and plasma parameters. As can be seen in Fig. 2.2.1, for these beam parameters, approximately the front half of the beam sees a retarding or decelerating field E^- whereas the back half of the beam sees an accelerating field E^+ . Consequently the peak voltage transformer ratio $R=E^+/E^-$ is approximately one as the front half of the beam losses energy to the wakefield and the back half of the beam extracts energy from the wakefield. The energy extraction efficiency can be quite high as seen from the second accelerating peak that is left

behind the drive bunch. This peak has half the amplitude of the first peak which in 1-D would mean that approximately 75% of the energy has been extracted from the wake by the accelerating particles. As mentioned earlier, wakefields produced after the beam has propagated 1 cm (dotted line) and 14 cm (solid line) are almost identical.

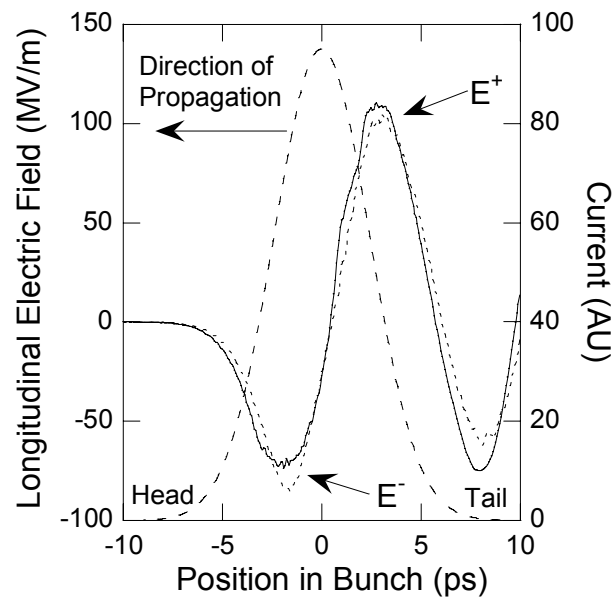


Fig. 2.2.1. Longitudinal wakefield excited on axis by a positron beam (dashed line) propagating from right to left after 1 cm (dotted line) and 14 cm (solid line) in a plasma. The notations used in the following figures 2-10 are depicted in the above figure.

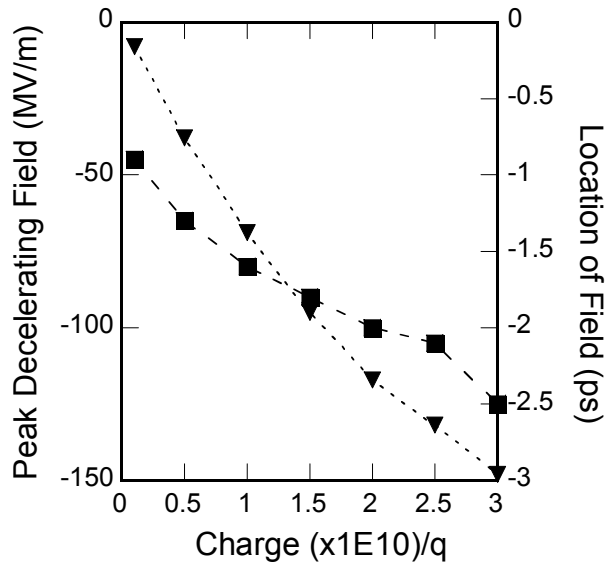


Fig. 2.2.2. Peak decelerating field (triangles) and its temporal location in the bunch (squares) vs. charge.

Figure 2.2.2 shows how the peak decelerating field E^- (triangles) varies with charge of the positron beam as the number of positrons, charge/ q , is varied between 1×10^9 and 3×10^{10} . The field increases monotonically with increasing charge. This is close to the prediction of the linear theory where the field strength would increase linearly with charge. In addition, the temporal location of the peak field is shown (squares). The location moves towards the head of the bunch again monotonically with increasing charge. As the charge is increased, the ratio of beam density to plasma density is increased. The subsequent increase in the space-charge field of the positron beam causes the plasma electrons to be pulled into the bunch sooner, thus leading to the location of the peak decelerating field moving forward.

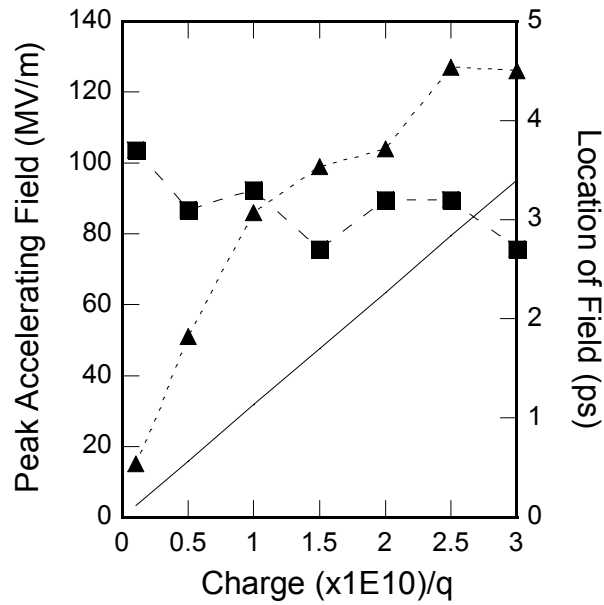


Fig. 2.2.3. Peak accelerating field (triangles) and its temporal location in the bunch (squares) vs. charge. The linear theory prediction for the peak accelerating field is shown as a solid line.

Figure 2.2.3 shows how the peak accelerating field E^+ (triangles) varies with charge. As before, the number of positrons is varied between 1×10^9 and 3×10^{10} . Consistent with the decelerating field, the peak accelerating field is also seen to increase with increasing charge; however, the field strength increases linearly up to a charge/q of 1×10^{10} , but then it begins to saturate with increasing charge. Whereas linear theory (solid line) predicted a linear growth of the field strength, it did not predict the saturation predicted by the PIC code. This saturation is due to the phase mixing of the plasma electrons pulled in by the beam as they oscillate about the beam axis. Furthermore, linear theory underestimates the field strength because of the greater role

of the radial fields of the beam. The temporal location of the peak accelerating field (squares) changes less than ± 0.5 ps with increasing charge in contrast to E^- which moves forward in the beam as mentioned earlier. It is important to note that for an electron beam driver, as one transitions from the linear ($n_b \ll n_p$) to the highly nonlinear ($n_b \gg n_p$) regime, the accelerating field rapidly increases as the beam density (or the drive beam charge for a given spot size) is increased because the plasma electrons which are blown out by the beam head return within a narrow range of arrival times which forms a density (and therefore electric field) spike on axis (Joshi *et al.*, 2002). In contrast there is a broad range of arrival times of the plasma electrons pulled in by the positron beam and therefore, there is no sharp spike in the peak accelerating field E^+ as seen in Fig. 2.2.1.

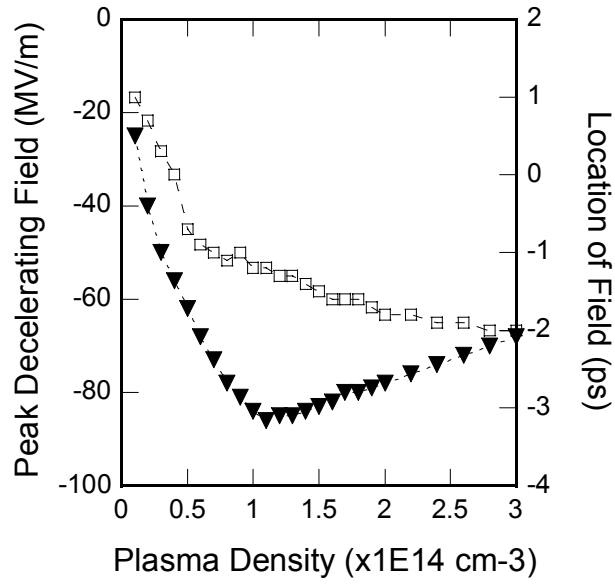


Fig. 2.2.4. Peak decelerating field (triangles) and its temporal location in the bunch (squares) vs. plasma density.

Figure 2.2.4 shows how the peak decelerating field E^- (triangles) varies with increasing plasma density. The strength of the field increases rapidly up until a peak value of -86 MV/m at a density of 1.1×10^{14} cm⁻³. This density satisfies the $k_p \sigma_z = \sqrt{2}$ condition from linear theory for peak field. As the density is further increased, the strength of the field slowly decreases as predicted from equation 5. The temporal location of the field (squares) moves from the back of the bunch towards the head of the bunch as the density is increased. This latter behavior is expected since the plasma wavelength is decreasing as the plasma density is increasing.

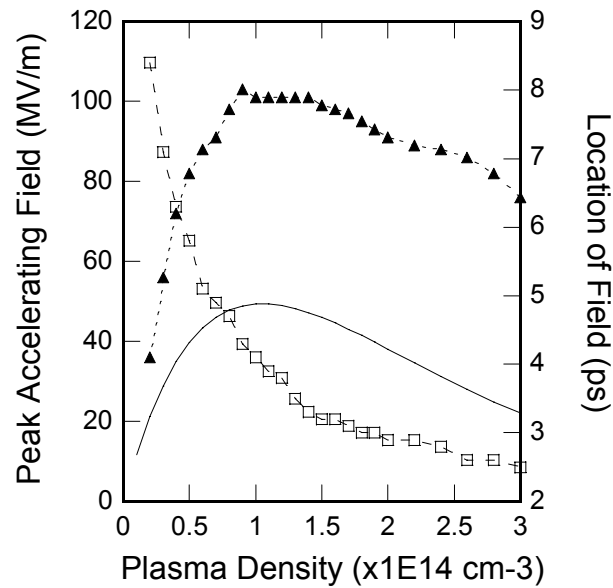


Fig. 2.2.5. Peak accelerating field (triangles) and its temporal location in the bunch (squares) vs. plasma density. The linear theory prediction for the peak accelerating field is shown as a solid line.

Figure 2.2.5 depicts the peak accelerating field E^+ (triangles) as a function of plasma density. The strength of the field rapidly increases up to a peak value of 103 MV/m at a density of $9 \times 10^{13} \text{ cm}^{-3}$. This value of density is close to that which is predicted by linear theory (solid line). Although the functional dependence of the peak accelerating field on plasma density predicted by linear theory is similar to the results obtained using PIC simulations, it underestimates the strength of the field. As the density is further increased beyond the optimal value, the peak field decreases as predicted by equation 2.72. The temporal location (squares) of this peak field moves from the back

of the pulse towards the head of the bunch as the density is increased since the plasma wavelength is decreasing.

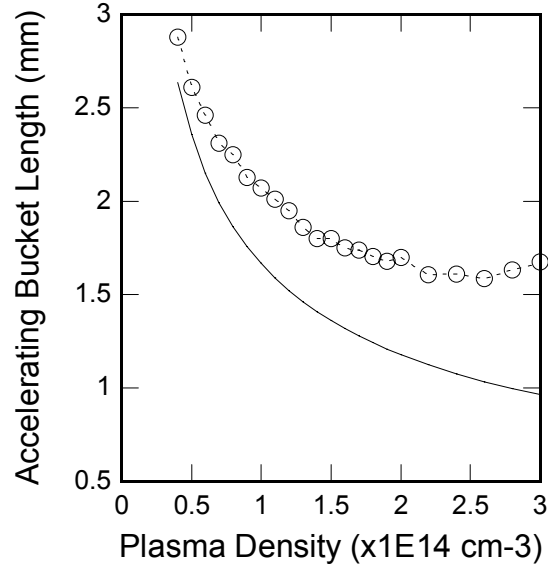


Fig. 2.2.6. Accelerating bucket width (circles) vs. plasma density. The linear theory prediction of half a plasma wavelength as a solid line.

Figure 6 shows the width of the accelerating bucket (circles) vs plasma density. The accelerating bucket is defined as the length of the field where the sign of the field is positive. According to linear theory developed in the previous section, the wake has a wavelength of $\lambda_p = c / f_p$. Since the plasma wavelength scales as $1/\sqrt{n}$, it will decrease with increasing plasma density. The accelerating bucket would then have a width given by $\lambda_p / 2$. The half wavelength is shown as the solid line in the plot. The simulations show that at low densities, the wavelength is close to the value which is

predicted by linear theory, however, at higher plasma densities the accelerating buckets are longer than that predicted by linear theory.

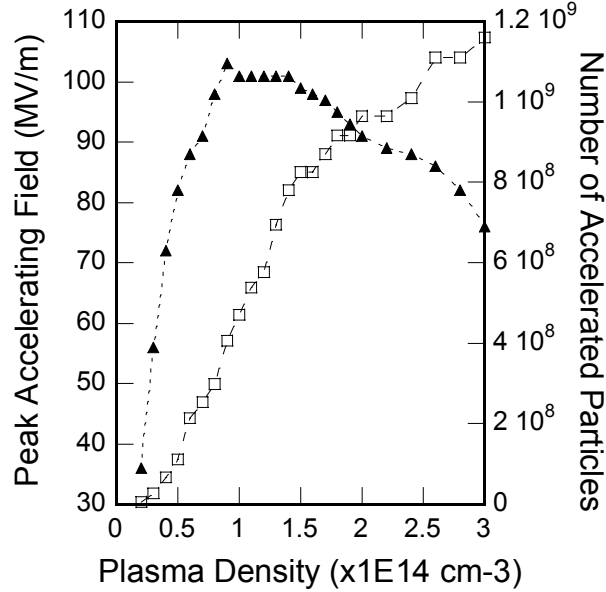


Fig. 2.2.7. Peak accelerating field (triangles) and accelerated charge in the 1 ps peak field bin (squares) vs. plasma density.

Figure 2.2.7 shows how the number of accelerated particles increases as plasma density is increased. As was shown in figure 5, the temporal location of the peak field moves from the tail towards the centroid of the bunch as the plasma density is increased. Therefore, since the pulse shape is Gaussian, more and more particles will be accelerated (squares). The number of accelerated particles is calculated by taking the number of particles in a 1 ps bin centered at the temporal location of the peak field. For instance, 5 times more particles are accelerated at a density of $2 \times 10^{14} \text{ cm}^{-3}$ than at $9 \times 10^{13} \text{ cm}^{-3}$ with only a 10% reduction in the peak field. At the optimum density of

$9 \times 10^{13} \text{ cm}^{-3}$, almost 3% of the total number of particles are within a picosecond wide slice situated about the peak accelerated field. In experiments where a single bunch is used to both excite and witness the plasma wakefield, this number of accelerated particles is important. This is due to the need to have sufficient signal strength (accelerated positrons) in order to overcome the noise in the diagnostics (usually photoelectrons on a streak camera) (Blue *et al.*, 2003).

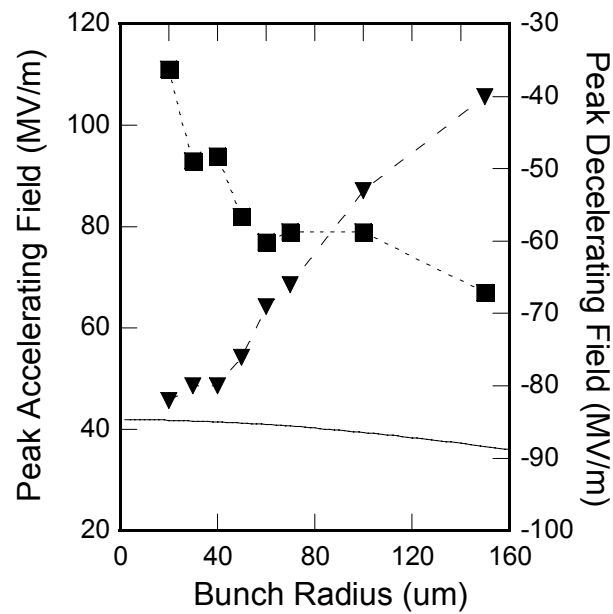


Fig. 2.2.8. Peak accelerating (squares) and decelerating (triangles) fields vs. bunch radius. The linear theory prediction for the peak accelerating field is shown as a solid line.

Figure 2.2.8 shows how the peak decelerating field E^- (triangles) changes as the radius of the beam is varied. As seen in the figure, the field decreases as the radius is increased. For instance, when the radius is increased from 40 μm (the typical value in

the experiment) by a factor of 4 to 160 μm , the field is decreased by a factor of 2. According to linear theory, as long as the bunch radius is much less than the collisionless skin depth, the decelerating field within the bunch should be independent of the beam radius. Since the radii used in the simulations are much less than $c/\omega_p = 400 \mu\text{m}$, this decrease is due to the changes in the beam charge density which in turn affects the radial distribution of the plasma electrons pulled in by the beam and therefore the work the beam does on these electrons. Also shown in Fig. 2.2.8 is how the peak accelerating field (squares) changes as the bunch radius is varied. As expected from the behavior of the decelerating field, as the radius is increased, the accelerating field strength is also decreased. As discussed earlier, the change in the field magnitude is due to both a change in the beam charge density and to the dynamics of the plasma electrons being pulled in from different radii.

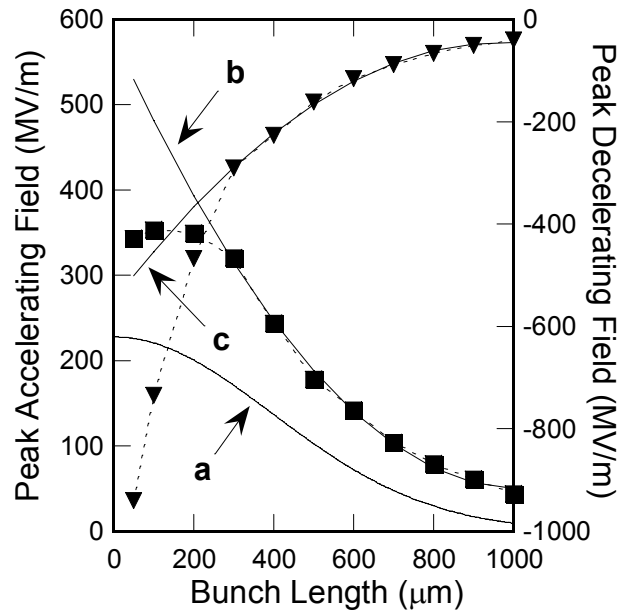


Fig. 2.2.9. Peak accelerating (squares) and decelerating (triangles) fields vs. bunch length. The linear theory prediction for the peak accelerating field (a) is shown as a solid line. The inverse quadratic dependence for the peak accelerating field (b) and the peak decelerating field (c) are shown as solid lines

Figure 2.2.9 shows the dependence of the peak decelerating field (triangles) on the bunch length. The field strength increases as the bunch length is decreased. According to the linear theory discussed in the preceding section, the field strength increases as $1/\sigma_z^2$. The data was fitted with a $1/\sigma_z^2$ dependence by taking the field at $\sigma_z = 1000 \mu\text{m}$ point as a reference point (solid line c). As inferred from the plot, the field strength does have an inverse quadratic dependence up to a bunch length of $300 \mu\text{m}$. For bunches shorter than this, the peak decelerating field seen in the simulations increases much more rapidly than what was predicted by linear theory.

Figure 2.2.9 also shows the dependence of the peak accelerating field (squares) on the bunch length. The field strength increases as the bunch length is decreased. According to the linear theory (solid line **a**) developed in the preceding section, the field strength E_+ seen in the simulations also increases as $1/\sigma_z^2$ (solid line **b**), but its magnitude is larger than that predicted by the linear theory. Note that for bunch lengths shorter than 300 μm , while the decelerating field actually increases faster than $1/\sigma_z^2$, the accelerating field saturates.

In the preceding section, scaling laws were developed in which a single beam or plasma parameter was varied while the others were held constant. Two important results were that the accelerating field increased quadratically as the bunch length was decreased (Fig. 2.2.9) and that each bunch length had a corresponding plasma density which maximized the accelerating field (Fig. 2.2.5). Therefore, we have tried a two parameter optimization of the peak accelerating field by simultaneously reducing the bunch length and increasing the plasma density using the linear theory relationship $k_p \sigma_z = \sqrt{2}$. The results for the peak accelerating field (triangles) are shown in Fig. 2.2.10(a). The solid curve shows the optimized plasma density from the linear theory. Now for $\sigma_z = 50 \mu\text{m}$ long bunches, peak accelerating fields of 2.7 GeV/m can be obtained from a 40 μm round beam with 1.2×10^{10} positrons in a $2 \times 10^{16} \text{ cm}^{-3}$ plasma. The longitudinal wakefield at this density is relatively sinusoidal as opposed to the electron beam case where it is highly nonlinear (Lee *et al.*, 2000). In

Fig. 2.2.10(b), we plot the peak decelerating field (circles) which accompanied the accelerating field as well as the transformer ratio $R=E^+/E^-$ for different values of bunch lengths used in Fig 2.2.10(a). At the bunch length is shortened, the transformer ratio increases from 1 (energy loss equals energy gain) to a value of 1.6 with a 50 μm long bunch. This means as bunch length is decreased, one benefits from both an increased acceleration field as well as a higher energy gain to energy loss ratio.

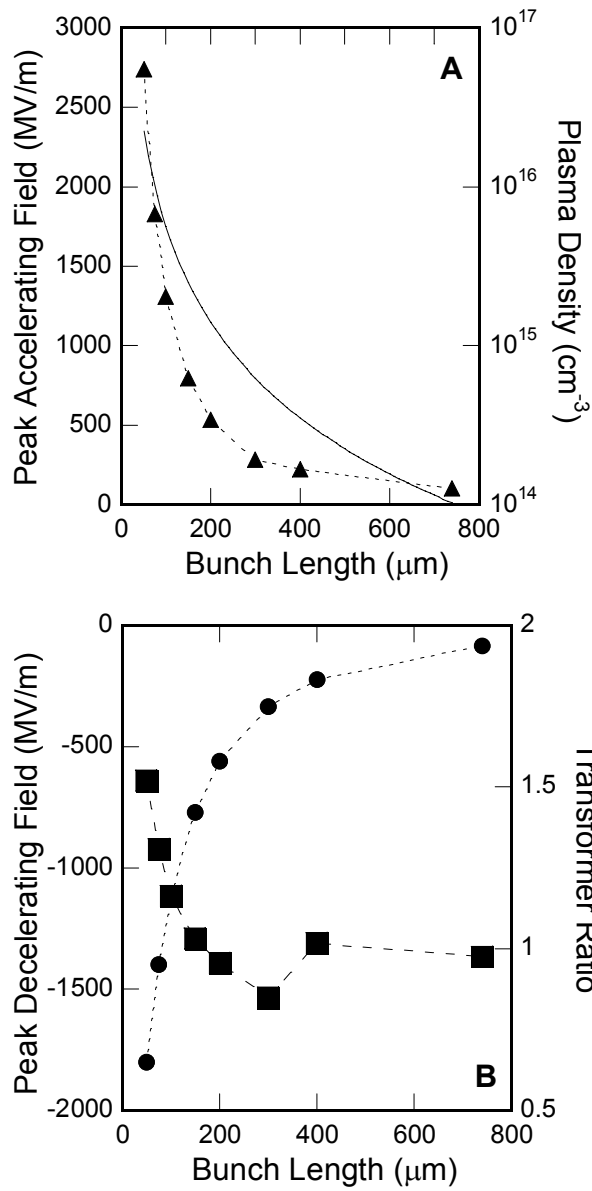


Fig. 2.2.10 Peak accelerating field (triangles), decelerating field (circles), and transformer ratio (squares) vs. bunch length. The matched plasma density for the peak accelerating field is shown as a solid line.

Further increase in the accelerating field can result from propagating the positron beam in a hollow channel as has been shown in other PIC simulations (Lee *et*

al., 2001), and higher transformer ratios could result from using tailored shapes for the drive beam instead of a symmetric Gaussian pulse. These issues are currently being explored. The stability of the drive beam against transverse beam-break up instabilities, such as the transverse two-stream instability, is also a critical issue that needs further work.

2.3 3-D Particle in Cell Simulations

The above results looked at the fields generated by the positron beam in a plasma. These fields were calculated just as the bunch entered the plasma. In the experiment, the bunch was propagated through 1.4 meters of plasma. The strong fields generated will affect the beam, which in turn will affect the fields. To predict the outcome of the experiment, full 3-D PIC simulations were run using the code OSIRIS. This code allowed us to incorporate all beam-plasma dynamics and measure the energy changes of the particles at the exit of 1.4 meters of plasma.

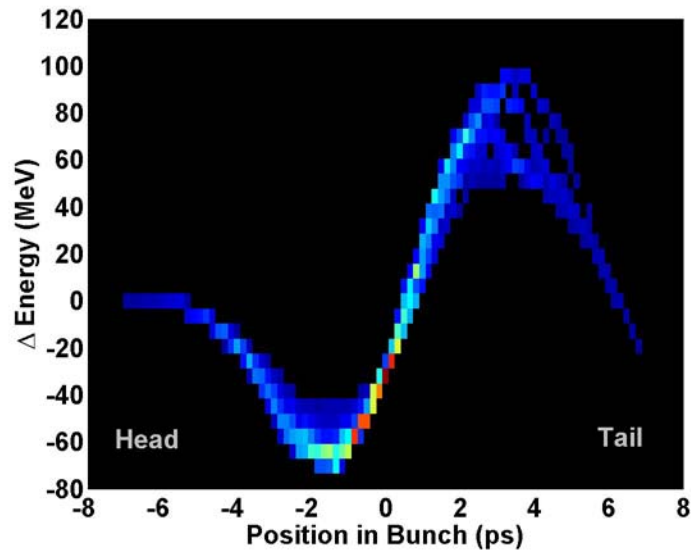


Figure 2.3.1 Beam energy at the exit of the plasma cell

Figure 2.3.1 shows the energy changes imparted on the beam by a plasma of density $1.8E14 \text{ cm}^{-3}$. The code predicts that the head of the bunch will lose energy driving the plasma wave and that the tail of the bunch will extract energy from the plasma wave and be accelerated. The simulation parameters consisted of grid sizes $\Delta x = \Delta y = \Delta z = 50 \text{ }\mu\text{m}$, 8 plasma particles per cell, 12 beam particles per cell, and a moving simulation window of $3.2 \text{ cm} \times 3.2 \text{ cm} \times 6.4 \text{ cm}$ in x , y , and z respectively. The energy of the beam is referenced to 28.5 GeV. With a similar appearance to the fields plot, the front part of the bunch is seen to lose energy while the back part of the beam is accelerated by the wakefield. An energy loss of 56 MeV and an energy gain of 74 MeV were predicted by the PIC code. In Section 6, the results of the OSIRIS simulations will be compared to the experiment.

3 Experimental Setup and Diagnostics

E162 was an experiment to study acceleration of 30 GeV electrons and positrons over 1.4 meters in a plasma wakefield accelerator [15]. The experiment was run at the Stanford Linear Accelerator (SLAC.) It was carried out by a collaboration of scientists from the University of California – Los Angeles (UCLA), the University of Southern California (USC), and Stanford University. The goal of the experiment was to explore and develop techniques needed to implement a high-gradient PWFA in a large-scale accelerator. With respect to the electron and positron beams, the goals were to study the longitudinal effects (acceleration of the tail and deceleration of the beam centroid) and the transverse effects (betatron oscillations, emission of betatron radiation, and hosing).

The basic idea of the E162 experiment is to use a single electron or positron bunch where the front of the beam excites a plasma wave and the tail of the beam witnesses the resulting accelerating field. The nominal beam parameters were 2×10^{10} , 28.5 GeV electrons or positrons, a bunch length of 0.7mm, and a transverse spot size of 30 μm . This beam was propagated through a 1.4m long Lithium plasma of a density up to $4 \times 10^{14} \text{ e}^-/\text{cm}^3$. The plasma source is positioned at interaction point 0 in the Final Focus Test Beam (FFTB) at SLAC. The FFTB is placed in a straight line path at the end of the 3km long SLAC accelerator and was designed to investigate the factors that limit the size and stability of the beam at the collision point of a linear

collider. The beam optics and diagnostics are capable of delivering a high quality, well diagnosed beam to our experiment. In addition to the beam diagnostics built into the FFTF (beam position monitors, current measuring torroids, and wire scanners), the experiment required single shot beam profile measurements before and after the plasma and time resolved measurements after an energy dispersive bend magnet. These diagnostics allowed the E162 collaboration to study the transverse and longitudinal dynamics of a high peak current ($>100\text{A}$), ultra-relativistic electron bunch in a 1.4m of $0-4 \times 10^{14} \text{cm}^{-3}$ underdense plasma.

This chapter describes how the facilities and the diagnostics were brought together to perform the complicated set of experiments known as E162. The following sections will detail the diagnostics, the experimental calibrations and measurements for those diagnostics, and the theoretical justifications of the performance of our diagnostics and equipment. The principle components of the experimental apparatus are the Lithium plasma source [30], the imaging spectrometer, the optical transition radiators [31, 32], the beam position monitors [33], and a time-integrated and time-resolved aerogel Cherenkov radiator [34]. A brief description of each component will now be given. For a more detailed view of any specific component, refer to the references given above.

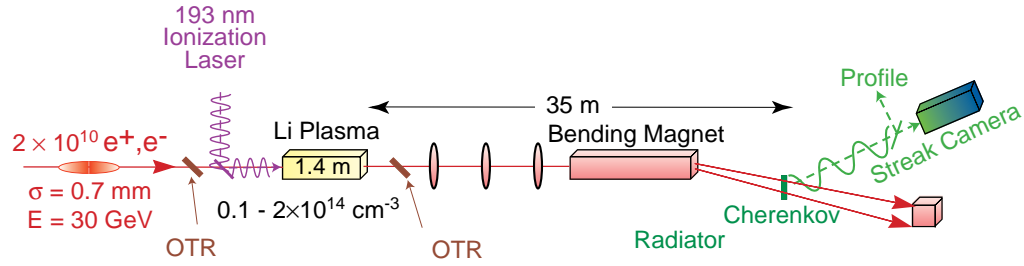


Figure 3.0.1 Schematic of experimental setup. The positron beam travels left to right in the diagram. The transverse profile of the beam is measured before and after the plasma using OTR radiators. Upon exiting the plasma, the beam is imaged from the plasma exit onto the Cherenkov radiator with a magnetic imaging spectrometer. Plasma induced energy variations along the positron bunch are measured with a streak camera.

3.1 Lithium plasma source

The two main components of the Li plasma source are the heat pipe oven and the ionizing laser. The heat pipe oven consists of a stainless steel tube wrapped in heater tapes. The inside is lined with a wire mesh and is partially filled with solid (at room temperature) Lithium. Water jackets are placed at each end of the oven. A helium buffer gas is used to constrain the Li vapor. The oven is heated to $\sim 750^\circ\text{C}$ and a Li vapor is formed. The vapor flows from the center of the oven (where it is the hottest) to the water jackets (where it is the coolest). The mesh acts as a wick and transports the Li back towards the center of the oven. The Helium gas, in conjunction with the water jackets, constrains the Li vapor into a uniform column with sharp boundaries. The end product of this heat pipe is a 1.4m long, uniform column of Li vapor at a density of $\sim 2 \times 10^{15} \text{ cm}^{-3}$.

An argon-fluoride excimer laser provides an ultraviolet pulse (193nm, 6.45eV) to ionize the Li vapor via single photon absorption. The first ionization energy of Li is 5.392eV with an ionization cross section of $1.8 \times 10^{-18} \text{ cm}^{-2}$. A 10-20ns laser pulse is focused down the vapor column so that laser fluence is constant (photon absorption is counteracted by reduced spot size). Because the laser fluence determines the plasma density, simply changing the output pulse energy on the laser can vary the oven's plasma density. This results in a 1.4m long plasma column of with a variable density up to $4 \times 10^{14} \text{ cm}^{-3}$ as the laser energy is varied from 0-40 mJ.

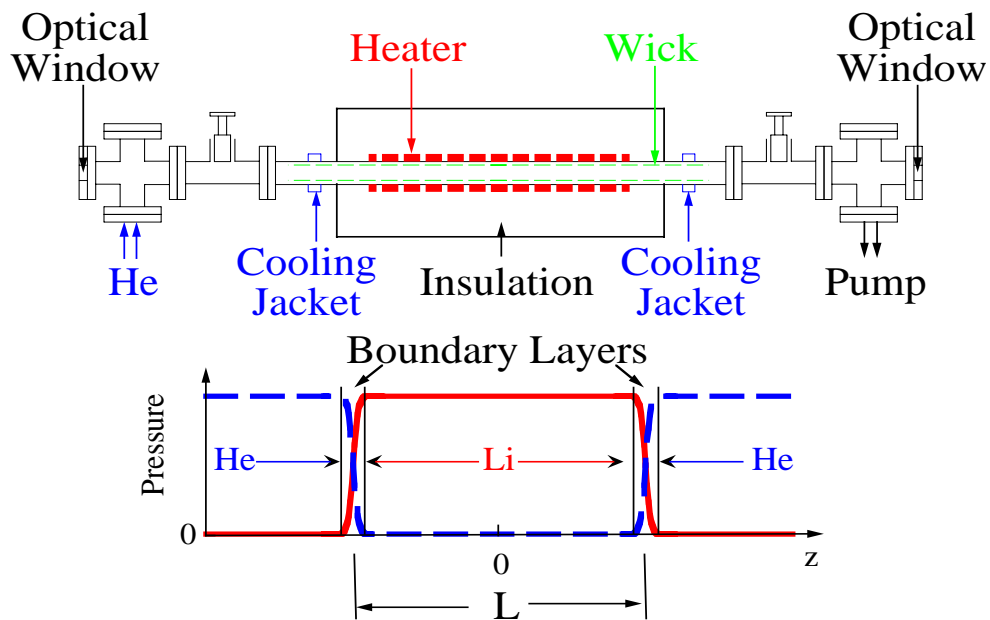


Figure 3.1.1 Diagram of Lithium Oven Setup and Depiction of Lithium Column. The cold helium buffer gas (blue) contains the hot Lithium vapor (red). The resultant Lithium vapor column has a uniform vapor density profile with sharp edges at the boundary.

3.2 Measurement of plasma density

One critical parameter in our experiment was the plasma density. The unique setup of our experiment and the plasma properties precluded us from using traditional techniques for density measurements such as Langmuir probes and interferometry. Since the plasma was produced through single photon ionization, we could determine the plasma density by knowing the laser fluence and the Lithium vapor density.

The vapor density was known by measuring the Lithium temperature profile inside of the oven. Four thermocouples located inside the oven were continuously monitored by a LabView program during the experiment. The formula for calculating Lithium vapor density from temperature is

$$n_{\text{vapor}}(T_K) = \frac{9.66 \times 10^{18}}{T_K} \cdot 760 \times 10^{\left(5.055 - \frac{8023}{T_K}\right)} \quad (3.1)$$

The following figure shows the measured temperature as recorded on December 16, 2001. The significance of this date is that the data set I use in my analysis was taken on this day.

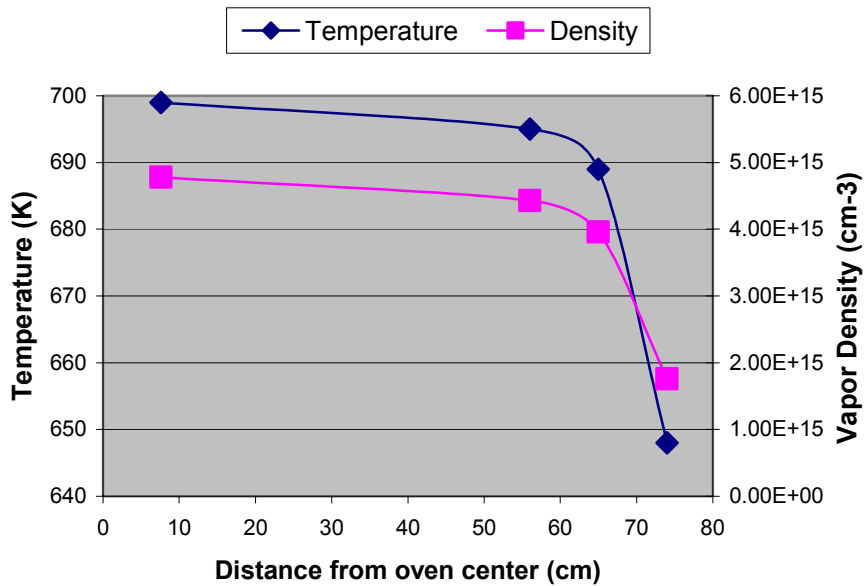


Figure 3.2.1 Temperature (blue) and vapor density (magenta) profile inside heat pipe oven as measured on December 16, 2001.

The fluence of a laser is the pulse energy per unit area. In order to calculate the laser fluence, one must know the laser energy and the area of the laser beam. It was required to know the laser energy inside of the Lithium vapor in order to calculate the density. This was not practical, but it could be inferred by knowing the energy just before the oven entrance and by knowing how the laser energy is absorbed inside of the Lithium vapor. The energy of the laser pulse was known on a shot by shot basis through the use of two laser pulse energy meters. The first energy meter was located near the output of the laser and it recorded the laser pulse energy on every shot. Due to a slow degradation of UV optics, the energy in the oven would decrease over time. In order to account for the optics degradation, a second energy meter could be inserted

in the beam line near the entrance of the oven. Since the second energy meter was after all of the optics, the energy it measured represented the energy at the entrance of the oven. Therefore, by calibrating the first energy meter with the second, the energy at the entrance of the plasma was known by measuring the energy at the exit of the laser.

With the energy at the entrance of the oven now known, we must also know how the laser is attenuated inside of the Lithium vapor. The absorption of the laser energy inside the oven is given by

$$E(z) = E_0 e^{-n_{\text{vapor}} \sigma_c z} \quad (3.2)$$

Here, E_0 , n_{vapor} , σ_c , and z are the incident laser pulse energy, the Lithium vapor density, the absorption cross section, and the distance into the vapor respectively.

Since our goal was to produce a uniform plasma column, we need to maintain a uniform fluence down the length of the Lithium vapor column. As you can see by from the absorption equation, the laser pulse energy will decrease down the length of the oven as it is absorbed and creating plasma. To counter this absorption, we focused the laser beam down the length of the oven. The following figures show the laser beam's spot size as it was focused down the oven.

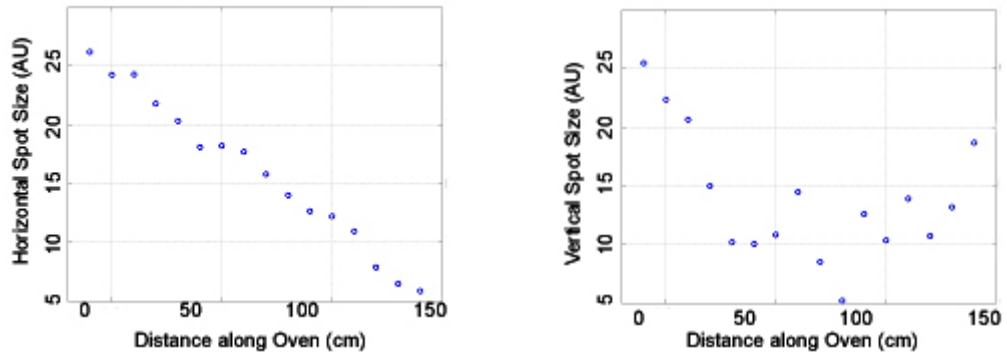


Figure 3.2.2 Focusing of laser in x (left) and y (right) through oven

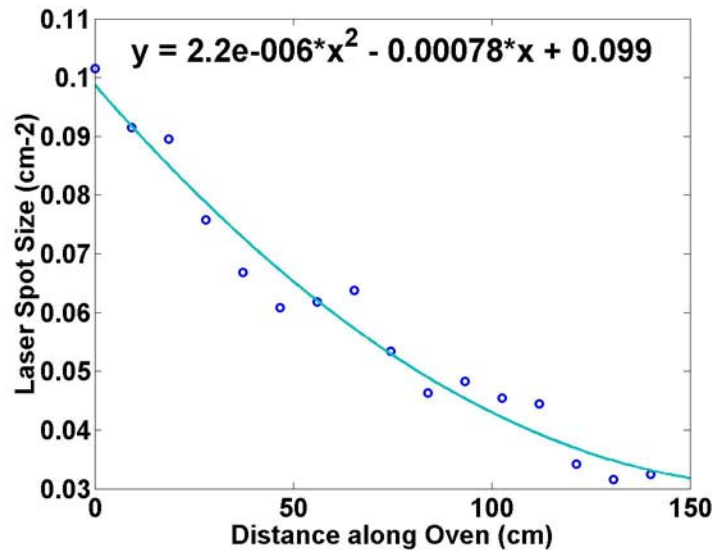


Figure 3.2.3 Area of laser pulse as it propagates through the oven

With the energy of the laser pulse and the spot size of the laser pulse known inside of the Lithium vapor, the plasma density could now be calculated. The formula is given by

$$n_e(z) = \frac{n_{\text{vapor}} \sigma_c E(z)}{h\nu A(z)} \quad (3.3)$$

Here $h\nu$ is the 193nm photon energy and $A(z)$ is the area of the laser beam along the oven. If 3 mJ is the laser pulse energy at the entrance of the oven, the plasma density along the oven is shown in the following figure. Although there appears from the figure to be a large variation on the plasma density, by looking at the scale, you will see that the density variation along the length of the oven is less than 5%. This was a significant improvement on the design requirement of less than 10%.

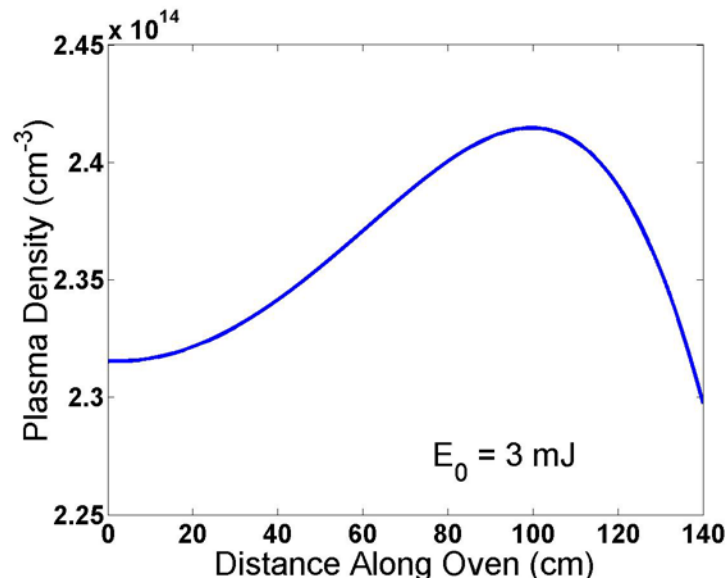


Figure 3.2.4 Plasma density profile with an initial pulse energy of 3 mJ. The plasma density is calculated using equation 4.3. The laser beam energy $E(z)$ is given by equation 3.2 where 3 mJ is the incident energy. The area of the laser beam $A(z)$ was calculated from a polynomial fit to the data points in figure 3.2.3.

3.3 Plasma Decay

The above plasma density was the initial density at time equal to zero. Due to jitter of the laser (~2-5ns), jitter of the positron beam (~10 ns), and our launching the positron beam into a plasma after a 300 ns delay time, we needed to know how the plasma evolved (i.e. decayed) on these time scales. As a first step, the theoretical work by Bates [35] was used to try and predict the behavior of our plasma. This was done by numerically solving the first order differential equation given by equation 3.4.

$$\frac{dn_p}{dt} = -\alpha_{Bates}(n_p) \cdot n_p^2 \quad (3.4)$$

This first step was very disconcerting because it predicted that the plasma would decay very rapidly on the time scale of 200-300 ns. The following figure shows how a plasma will decay in $t = 200$ and 300 ns according to Bates.

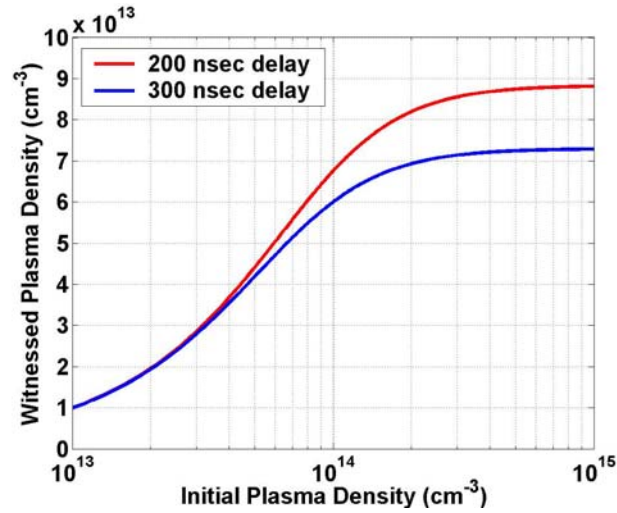


Figure 3.3.1 Theoretically predicted plasma density decay after a 200 ns delay (red) and after a 300 ns delay (blue). A plasma with an initial density of $1 \times 10^{15} \text{ cm}^{-3}$ would apparently decay to a density of $7(9) \times 10^{13} \text{ cm}^{-3}$ after 300 (200) ns.

This was problematic since it predicted that we could never reach the required density of $2 \times 10^{14} \text{ cm}^{-3}$ needed in our experiment. This prediction would explain some of the behaviors that we saw in the experiment. On some data sets, when the plasma was turned on, the positron beam focused down to a constant spot size even as the initial ($t=0$) plasma density was varied.

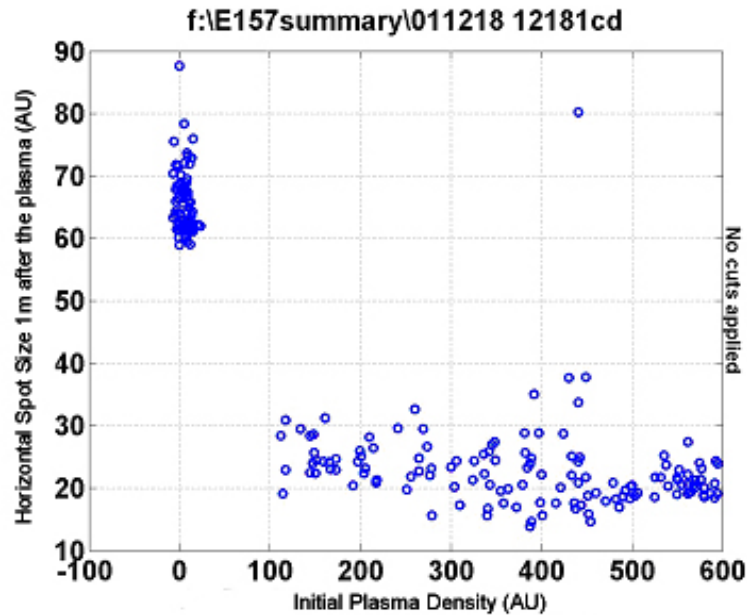


Figure 3.3.2 Focusing of positron beam vs initial plasma density.

This could be explained by the Bates analysis since the plasma decayed to a constant value after 300 ns even though the $t=0$ plasma density was varied. Fortunately, we knew that this could not be correct since betatron analysis of the electron beam proved that we had obtained densities as high as $6 \times 10^{14} \text{ cm}^{-3}$ [27]. Therefore the above figure shows the positron beam propagating through a plasma in which the beam divergence is matched by the plasma focusing force (the “match beam” case). The following figure is of an electron beam entering a nearly matched plasma. Part **a** is the experimentally measured curve of the electron beam’s spot size versus plasma density and **b** is the theoretically predicted spot size for a plasma which does not decay (blue) and a plasma which decays according to Bates (red).

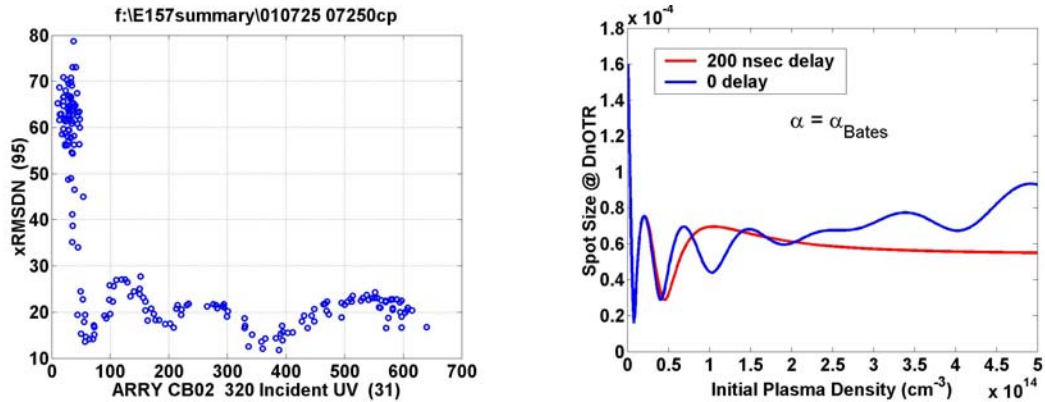


Figure 3.3.3 Electron betatron oscillations from **a** experiment and **b** theory. The experimental data shows the beam pinching down and undergoing small oscillations as the plasma density is increased. The figure on the right side shows the electron beam size at the downstream OTR which is modeled using the envelope equation for beam propagation. The blue curve represents the predicted spot size with a plasma which did not decay. The red curve represents the predicted spot size with a plasma which decayed 200 ns according to Bates. The experimental data agrees more with the plasma which did not decay.

Of note here is that the data shows oscillations at the highest density. It is not smoothed out as predicted by Bates. During discussions on plasma density, it was noted that historically there has been a disagreement between theory and experiment on plasma decay. I modified α_{Bates} by a constant to see if I could get the theoretical model to agree with experiment. The following figure shows the betatron oscillation fit to our data with and without decaying the plasma density. The plasma was decayed with $\alpha_{\text{eff}} = \alpha_{\text{Bates}}/100$.

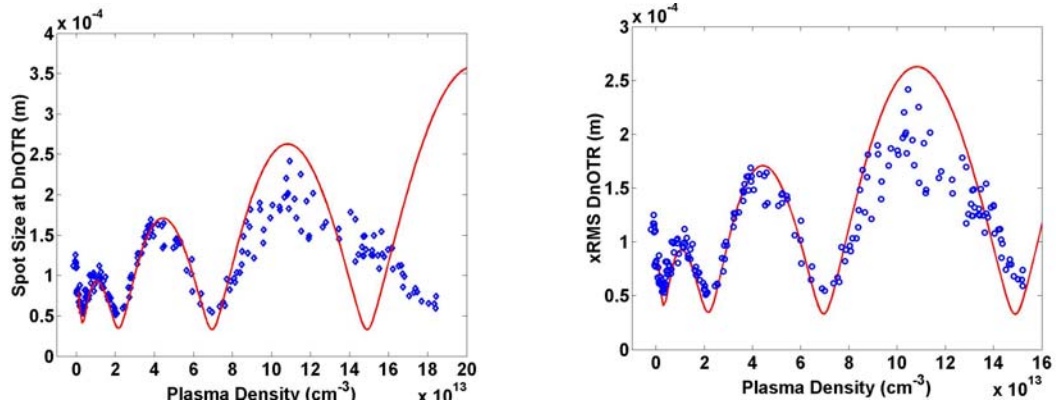


Figure 3.3.4 Betatron oscillations **a** with no plasma decay and **b** with decay. The data points (blue) are the same for both figures except for the plasma density calibration. The figure on the left used a plasma which did not decay. Disagreement is seen between the predicted density of the fourth pinch and the experimentally measured point. If the plasma is allowed to decay with an $\alpha_{\text{eff}} = \alpha_{\text{Bates}}/100$, excellent agreement is observed between our model and the experiment.

The above data was taken with a delay of 2535 ns. By using the α_{eff} , the plasma does not significantly decay on the time scale of 200-300 ns.

As a caveat to the following analysis, everyone who has tried to seriously analyze data in our experiment has attempted to tackle the problem of plasma decay. A final answer to this problem has not been reached since the plasma decay is a function of density and temperature, but all answers have come to the same conclusion that the plasma does not significantly decay for the densities and time scales used in my experiment.

3.4 Imaging Spectrometer

An imaging spectrometer was used to analyze the longitudinal dynamics of the beam in the E162 experiment. Significant knowledge was gained from the earlier E157 experiment and earlier in the E162 experiment on the dynamics of an electron/positron beam as it exited the plasma when no imaging spectrometer was used. These dynamics included betatron oscillations [25], hosing instabilities [27], dynamic focusing [26], and positron transverse dynamics [15]. These effects, while scientifically interesting, masked the energy gain/loss signature on our detectors. In order to remove (or minimize) these effects, we removed the drift space after the plasma and replaced it with an imaging spectrometer. The beam was imaged from the plasma exit onto the aerogel using quadrupole magnets and a dipole magnet added 291 MeV/mm dispersion in the y-direction or the vertical plane at the Cherenkov radiator.

3.5 Proof the imaging spectrometer was imaging

An imaging condition is reached when the spot size at an image plane is solely the function of the spot size at the object plane.

$$\sigma_{Cherenkov} = M \cdot \sigma_{Plasma\ Exit} \quad (3.5)$$

To make this measurement, the spot size at the Cherenkov is measured while the spot size at the plasma exit is varied. The spot size at the Cherenkov is measured with the time integrated Cherenkov detector. To measure the spot size at the plasma exit, first

the oven is removed from the beam line. Then a spool piece is used which has an OTR detector at the location of the plasma exit. The incoming beam is focused at the plasma exit and its size can be varied by changing the focusing strength of magnets upstream of the plasma. The following two figures show the spot size in the x-plane at the plasma exit (figure 3.5.1, 9 $\mu\text{m}/\text{pixel}$) and at the Cherenkov (figure 3.5.2, 16 $\mu\text{m}/\text{pixel}$) as the focusing strength is varied. As can be seen, the two spot sizes track each other and only differ by a magnification factor of ~ 3 .

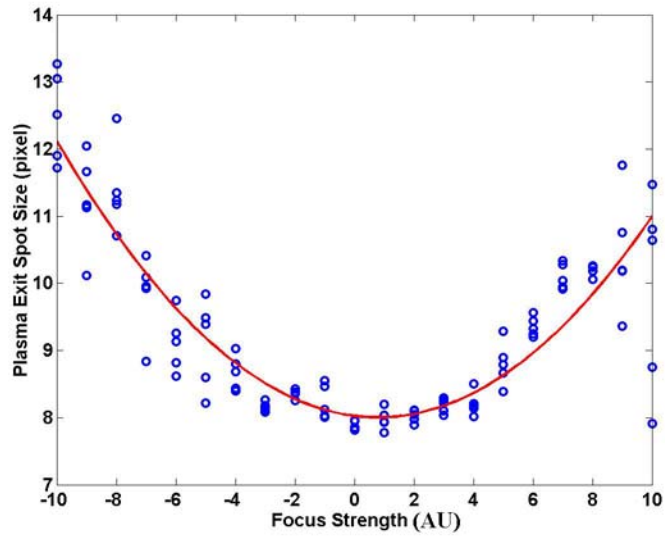


Figure 3.5.1 Spot size at plasma exit vs focusing strength

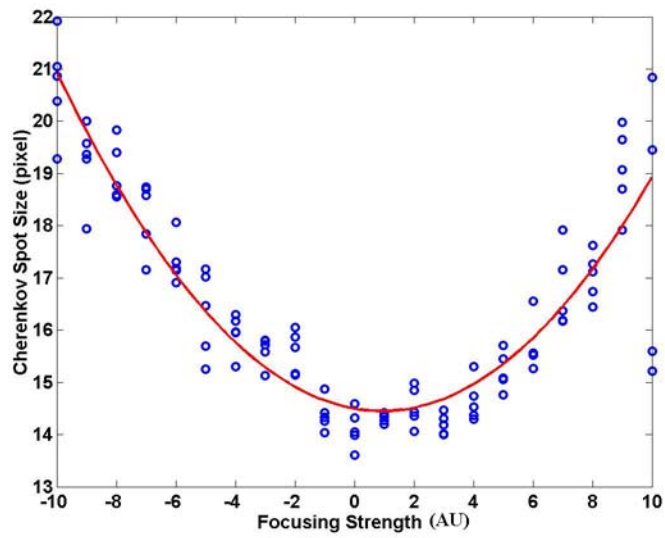


Figure 3.5.2 Spot size at Cherenkov vs focusing strength

3.6 Optical Transition Radiators (OTR)

Two OTR diagnostics were employed in the E157/E162 experiments, one ~ 1 m before the plasma and one ~ 1 m after the plasma. These diagnostics gave us a single shot time-integrated picture of the beam that allow us to measure the beam's spot size in both the x and y planes. The setup consists of a thin titanium foil placed at a 45° angle in the beam line. An AF Micro-Nikkor, 105mm, f/2.8D lens is used to image the OTR from the foil on to a 12-bit Photometrics Sensys CCD camera. The CCD has a pixel size of $9\mu\text{m} \times 9\mu\text{m}$ with an array size of 768×512 . The spatial resolution of the setup is approximately $20 \mu\text{m}$. A computer is used to read out the images and it can acquire data at 1 Hz.

OTR is one mechanism by which a charged particle can emit radiation. The radiation is emitted when a charged particle passes from one medium into another. For our case, the electron beam is propagating in a vacuum and then it enters a titanium foil. When the beam is in vacuum it has certain field characteristics, and when it is inside the titanium foil it has different field characteristics. As the beam makes the transition into the foil, the fields must reorganize themselves. In the process of reorganization, some of the field is "shed" off. Optical transition radiation is this "shed" field [36].

OTR has been used extensively on low energy (MeV) beams, but it was thought that it would not be a viable diagnostic for high energy (GeV) beams. The OTR has a peak at angles $\theta=1/\gamma$, which is small for 30 GeV beams ($\gamma=60000$).

Because diffraction limited resolution goes as λ/θ , the assumption was that high energy beams could not be resolved. The misconception was that θ is the numerical aperture of the lens, not the radiation source, and that there is significant radiation in the wings of the OTR distribution profile. The E157/E162 collaboration has proved this to be correct by measuring spot sizes on the order of 30 μm using OTR. Figures 3.6.1 and 3.6.2 show typical OTR images 1 meter upstream and 1 meter downstream of the plasma. The graininess of the downstream OTR image is not from the beam, rather it results from the grain structure of the titanium foil. Figure 3.9.3 shows how the image analysis routines in Matlab extract spot size information from the images.

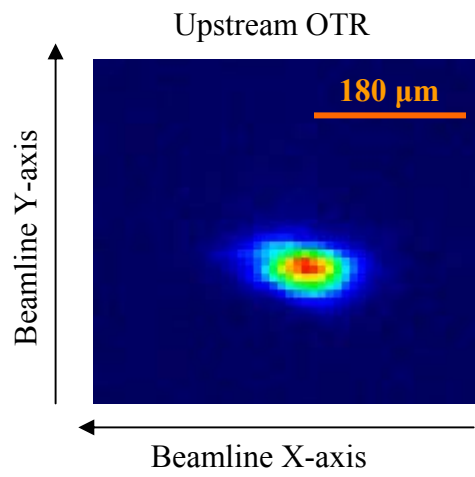


Figure 3.6.1 Sample upstream OTR image

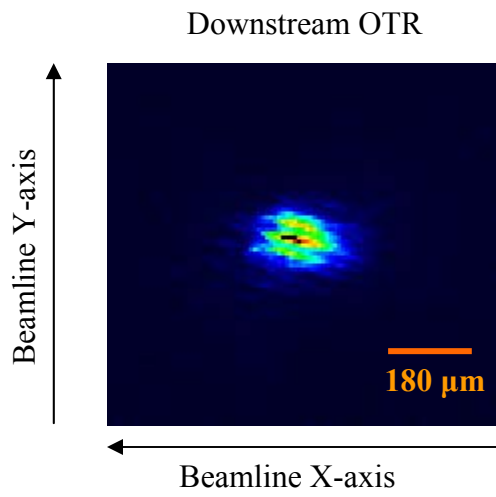
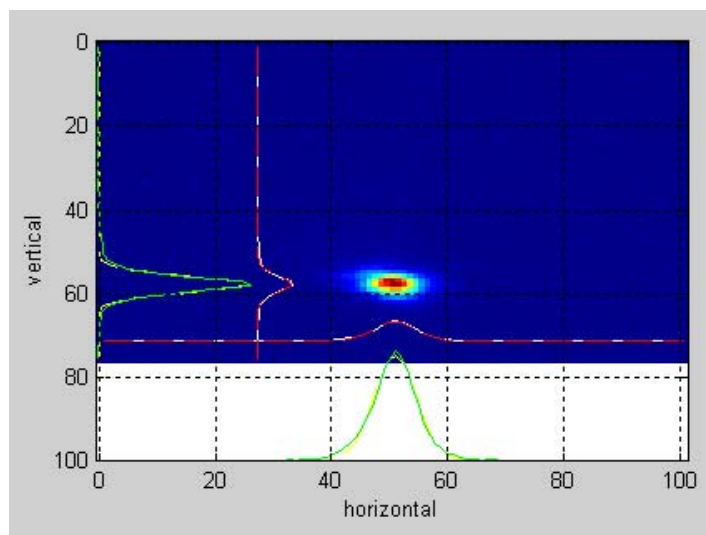


Figure 3.6.2 Sample Downstream OTR Image

Upstream OTR Image



Downstream OTR Image

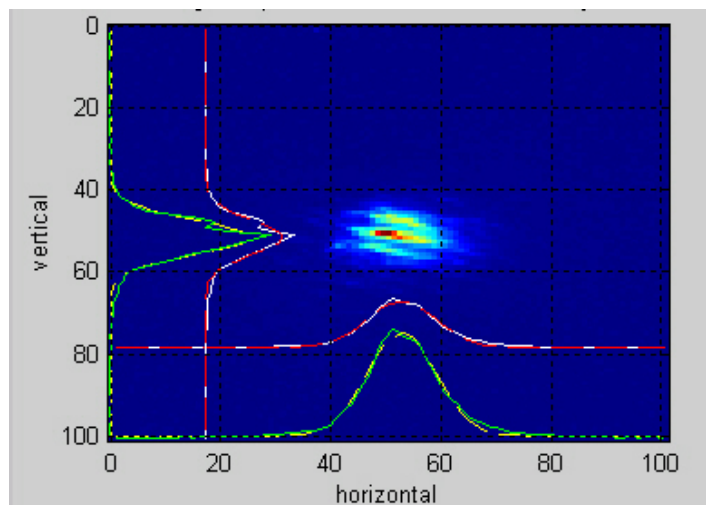


Figure 3.6.3 Image analysis of upstream and downstream OTR images. The white dashed line is the background level. The red line is a Gaussian fit to the background level. The dashed yellow line is either a summation of the columns (for the vertical plane) or a summation of the rows (for the horizontal plane). The green lines are Gaussian fits to the summation. The upstream image has a vertical spot size of $33.3 \mu\text{m}$ (3.7 pixels) and a horizontal spot size of $18 \mu\text{m}$ (2 pixels). The downstream image has a vertical spot size of $37.8 \mu\text{m}$ (4.2 pixels) and a horizontal spot size of $55.8 \mu\text{m}$ (6.2 pixels).

3.7 Proof of OTR Resolution

The optical transition radiation detector diagnostics placed before and after the plasma gave us the ability to monitor the time-integrated profiles of the positron beam on a shot-by-shot basis. This diagnostics allowed us to measure the r.m.s. spot size in both the horizontal and vertical planes. Additionally, we could detect the presence of beam tails and other asymmetries in the beam profile. Crucial to these measurements was an accurate measurement of the detectors resolution. This was performed using a resolution target with line pair widths less than the predicted resolution of $9\ \mu\text{m}$, the camera's pixel size. This was accomplished using the Air Force 1951 resolution target which consists of line pair widths ranging from $4\ \text{mm}$ to $4\ \mu\text{m}$ as shown in figure 3.7.1.

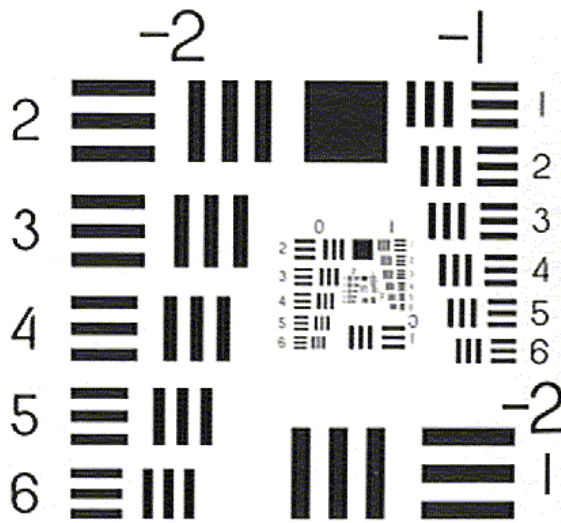


Figure 3.7.1 USAF 1951 Resolution target

Utilizing a commercial lens from Nikon in a 1-to-1 imaging mode, the following image was acquired of the resolution target.

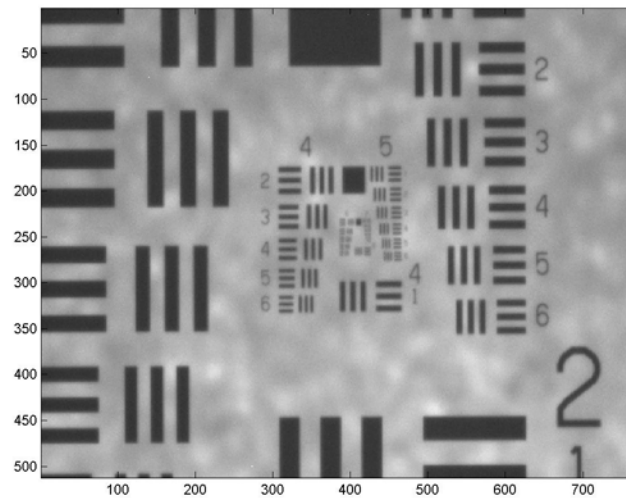


Figure 3.7.2 Acquired image of resolution target through our OTR optical setup

Based on line outs of the resolution target image for different line pairs. The depth of modulation falls below the 50% level for lines pairs less than 9 μm indicating that the our OTR optical system can resolve features down to 9 μm .

One tradeoff in obtaining the high resolution is a corresponding decrease in the depth of field (or depth of focus). This would not be an issue if we were resolving a plane perpendicular to the optical axis, but we are imaging a plane which is tilted at an angle of 45 degrees with respect to the optical axis. Based on experience of aligning and focusing the camera, we knew that the depth of field for the imaging system was

less than the field of view of $\sim 4\text{mm}$ ($9\ \mu\text{m}/\text{pixel} \times 450\ \text{pixels}$). Fortunately, the OTR radiator was not an ideal optical surface. It was a thin foil which contained rolling marks (from manufacturing) and small pits and crevices. These imperfections gave us a target to focus on and allowed us to measure the depth of field. At the highest magnifications one can see that the depth of field is now less than the field of view. The “strip of focus” was then aligned to the location of the beam so that images of the beam were in focus.

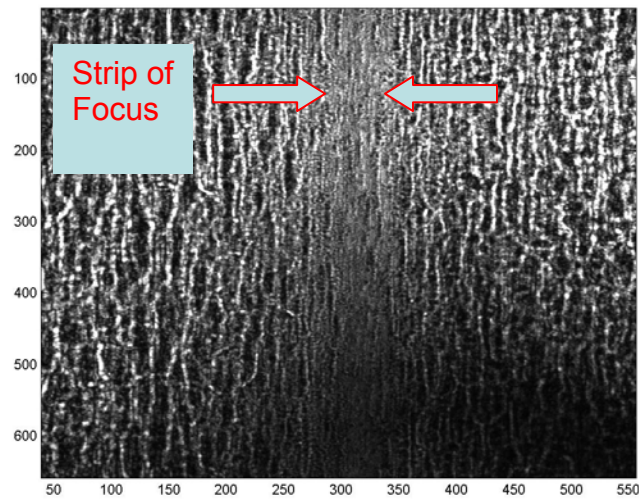


Figure 3.7.3 Strip of Focus. Only the region between the arrows is in focus because the foil is tilted at an angle of 45 degrees and the depth of focus is less than the field of view.

3.8 Beam Position Monitors (BPMs)

BPMs measure the beam's position by coupling to the beam's electromagnetic field. They use four stripline antennas mounted in quadrature inside the beam pipe as shown in figure 3.8.1.

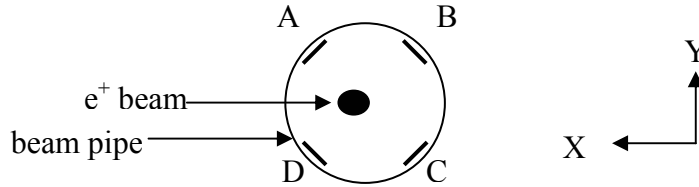


Figure 3.8.1 Typical Stripline BPM

The most common measurement is called the “difference over sum” method. In this method, the radio frequency signal is peak rectified and stretched. The output is then fed into circuitry that calculates positions from

$$X = \frac{(A+D)-(B+C)}{A+B+C+D} \frac{1}{S_x} \quad (3.6)$$

$$Y = \frac{(A+B)-(C+D)}{A+B+C+D} \frac{1}{S_y} \quad (3.7)$$

where

$$S_x(0,0) = S_y(0,0) = \begin{cases} \frac{\sqrt{2}}{r}; @45^\circ \\ \frac{1}{r}; @0^\circ \end{cases} \quad (3.8)$$

In addition to calculating position, the BPMs can also be used to measure the beam current.

BPMs are positioned all along the beam line in the FFTB. Several are upstream of the plasma chamber and are used to align the beam with quadrupole magnets and our plasma chamber. BPMs located downstream of the plasma chamber are used to measure the trajectory of the beam as it exists the plasma.

3.9 Aerogel Cherenkov Radiator

Cherenkov radiation is emitted whenever charged particles pass through a medium with a velocity that exceeds the velocity of light in that medium.

$$v > v_t = c/n \quad (3.9)$$

where v is the particle's velocity (in our case $v=c$), v_t is the threshold velocity, and n is the index of refraction of the medium. One can see that Cherenkov radiation will be emitted anytime a relativistic beam passes through any medium ($n>1$). The light is emitted at a constant angle with respect to the particle's trajectory.

$$\cos(\delta) = \frac{v_t}{v} = \frac{c}{vn} = \frac{1}{n\beta} = \frac{1}{n} \text{ (for } v = c) \quad (3.10)$$

This emission is similar to the bow shock created during supersonic flight.

In our experiment, we use the Cherenkov light as part of our energy gain diagnostic. The electron beam exits the plasma and is imaged onto a piece of aerogel ($n=1.008$) through an energy dispersive magnet. As the beam passes through the

aerogel it emits Cherenkov radiation in the visible spectrum at a cone angle given by equation 3.10. The light is transported approximately 15m to an optical table outside of the FFTB. The light passes through a beam splitter and a small fraction of the light is sent to a CCD camera for time-integrated images of the beam. A typical example of the time-integrated Cherenkov image is shown in figure 3.9.1 (similar to the OTR images). The remaining light passes through a beam splitter (50% transmitted and 50% reflected) again and one arm is rotated 90 degrees. The two paths are recombined and sent to the streak camera. The 90 degree rotation allows us to streak both the energy dispersive plane (y-axis) and the non-dispersive plane (x-axis) simultaneously figure 3.9.2. Figure 3.9.3 shows the layout of the optical table. The streak camera has a temporal resolution of approximately one picosecond and a spatial resolution of $\sim 100 \mu\text{m}$.

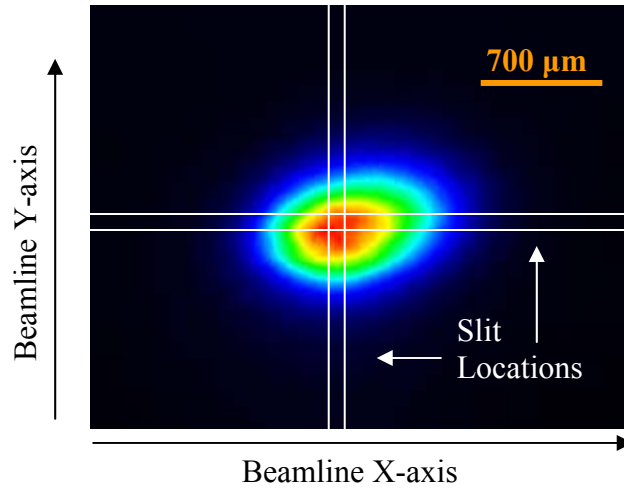


Figure 3.9.1 Time Integrated Cherenkov Image depicting the parts of the beam seen by the horizontal and vertical slits on the streak camera

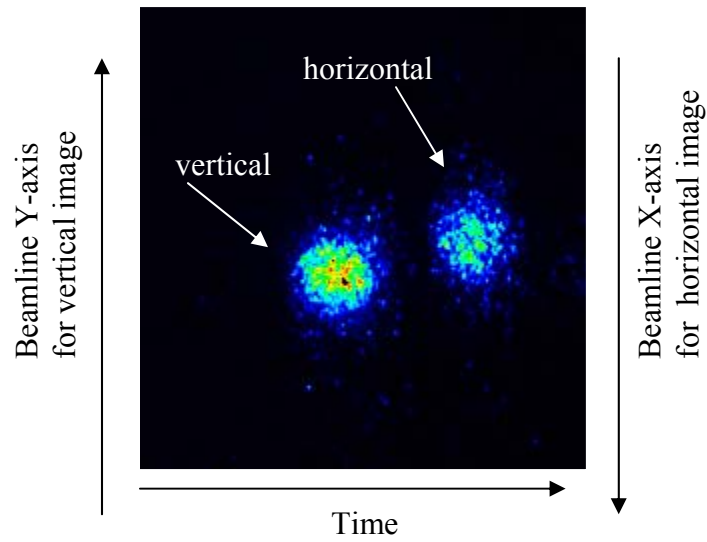


Figure 3.9.2 Typical Streak Camera image showing both the horizontal and vertical streaks

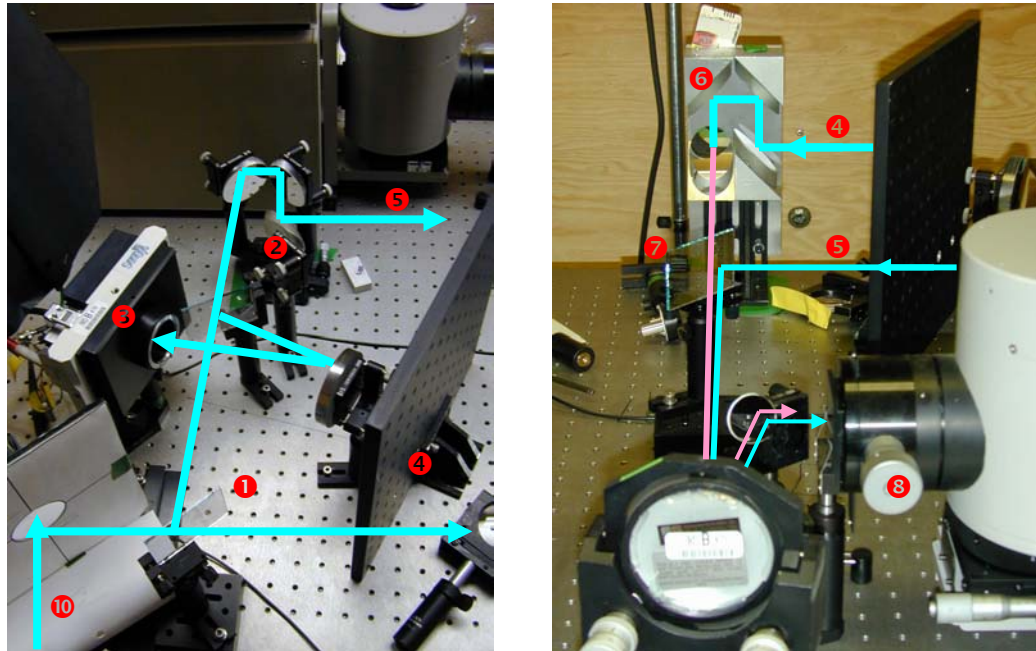


Figure 3.9.3 Diagram of Cherenkov radiation detector setup. The light radiated from the aerogel enters the setup at ⑩. It is reflected off of a mirror towards beam splitter ①. Part of the light is sent to the image rotator ⑥ via path ④ while the other part is directed towards beam splitter ②. Part of light off of beam splitter ② is sent to a CCD camera ③ for time integrated Cherenkov images while the rest is directed towards beam splitter ⑦ via path ⑤. The image on path ④ passes through an image rotator ⑥ where it is rotated 90 degrees (the unrotated path is shown in light blue while the rotated image path is shown in purple). Both the unrotated and rotated images are combined at beam splitter ⑦. The combined images (slightly delayed in time from each other) are then sent to the streak camera ⑧ for time-resolved analysis.

3.10 Time-Integrated Cherenkov Calibration

The time-integrated Cherenkov image provided vital information to our experiment. The first piece of information was the overall transverse spatial profile of the bunch. The second piece was the overall energy spread of the beam. The final piece was the determination of which parts of the beam were sampled by the streak

camera. The methods of calibration are similar to the methods used with the OTR detectors. The main differences were that due to the larger beam size, a custom target was used for $\mu\text{m}/\text{pixel}$ calculation and that since the Cherenkov radiator was perpendicular to the optical axis, depth of field was not an issue. From the line pair separation of 1 mm as seen in Figure 3.10.1, a calibration of $16 \mu\text{m}/\text{pixel}$ is calculated. With the dispersion of 291 MeV/mm in the vertical plane, each pixel also corresponds to 5 MeV of energy.

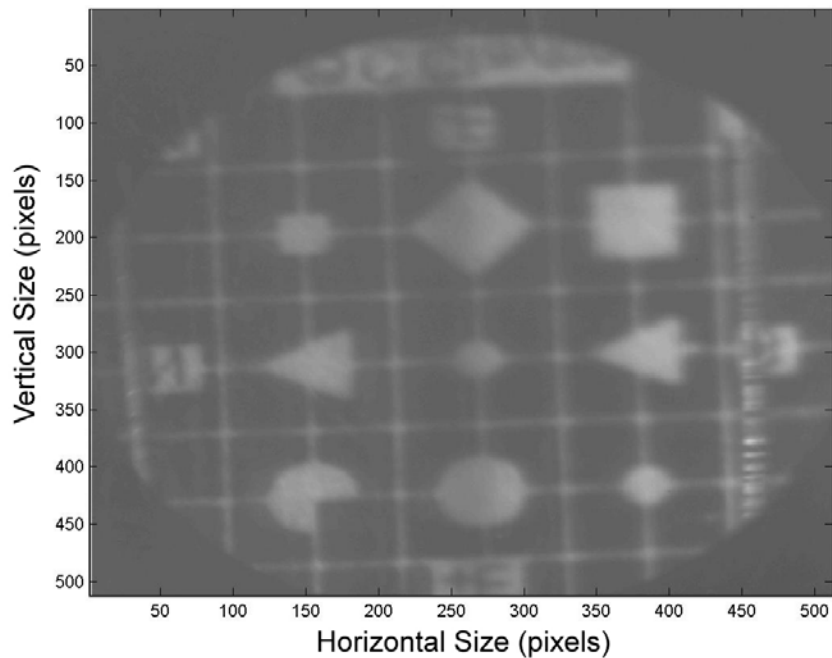


Figure 3.10.1 Resolution target image on integrated Cherenkov. The units of the acquired image are pixels. The line spacing on the resolution target is 1mm. This allows us to know the number of pixels per mm, or conversely, microns per pixel.

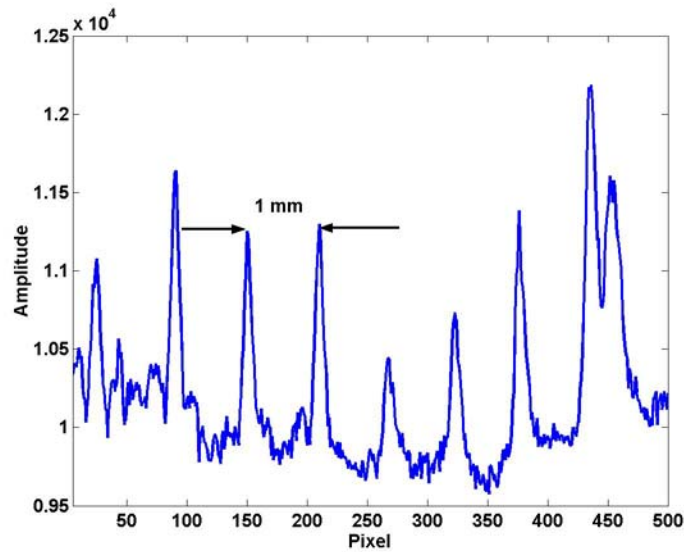


Figure 3.10.2 Line out of resolution target for pixel calibration. The peaks on the line out correspond to the 1 mm separated lines on the resolution target. By knowing the number of pixels per mm, we can calibrate microns per pixel.

3.11 Streak Camera Calibration

The time-resolved Cherenkov radiation was the main diagnostic of the experiment since it permitted energy changes as a function of time within the positron bunch to be measured. While the temporal resolution was limited to 1 ps by the streak camera, the pixel size needed to be calibrated in terms of spot size and energy. The calibration follows the exact same methods used to calibrate the time-integrated Cherenkov diagnostic. As can be seen in the following figures, the streak camera has a calibration of 16 $\mu\text{m}/\text{pixel}$ and this corresponds to 4.56 MeV/pixel in the vertically dispersed image.

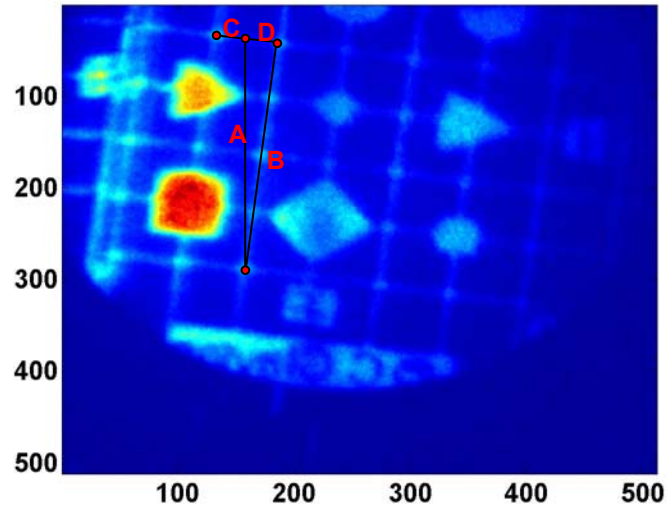


Figure 3.11.1 Resolution target for streak camera calibration. The calibration is done by using the distances labeled above in the figure. Since the target is tilted with respect to the axis of dispersion (the vertical axis), the distance **A** must be calculated from the know distances **B**, **C**, and **D**.

$$B = 4mm$$

$$C + D = 1mm$$

$$A = \sqrt{D^2 + B^2}$$

$$Calibration = 16 \mu m / pixel$$

$$\Delta y = \eta \frac{\Delta E}{E} \quad (3.11)$$

$$E = 28,500 MeV$$

$$\eta = 10cm$$

$$\frac{\Delta E(MeV)}{\Delta y(Pixel)} = \frac{E(MeV)}{\eta(cm)} \frac{1(cm)}{10^4(\mu m)} \frac{16(\mu m)}{1(Pixel)} = 4.56 MeV / pixel$$

3.12 Measurement of Bunch Length

The bunch length is an important quantity in our experiment. It was a straight forward measurement using the streak camera to obtain the temporal (i.e. longitudinal or length) profile of the beam. Care was taken to make sure that the streak camera's slit sampled the entire beam so that the bunch length measurement was accurate. In addition, several measurements were taken while varying the streak camera attenuation so that space-charge effects did not factor into our measurement. The next figure shows a typical streak camera image along with its corresponding integrated Cherenkov image which shows which part of the beam was sampled by the slit of the streak camera.

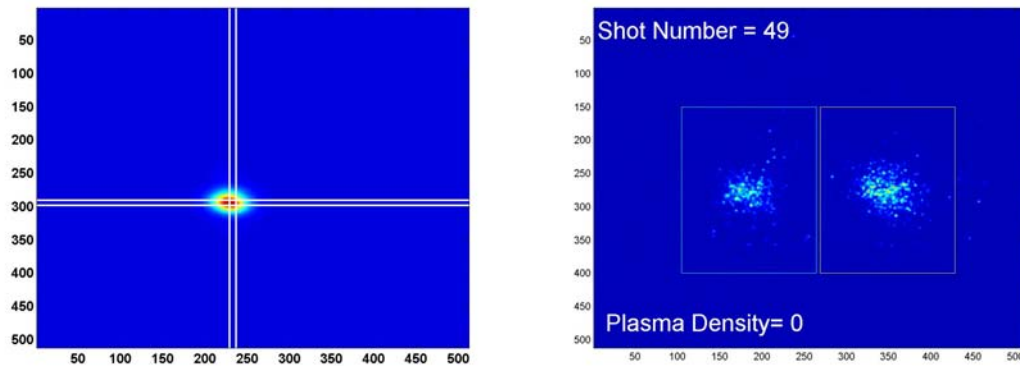


Figure 3.12.1 Time Integrated (left) and Time Resolved (right) images for the same shot. The white lines represent the slit of the streak camera so that we know which part of the beam was sampled by the streak camera slit. The right hand image shows the time resolved streak camera data. Time on the streak camera image increases from left to right. The vertical streak is at an earlier time than the horizontal streak since a delay was added to the horizontal streak camera optical path.

The next figure shows the longitudinal profile of the beam as derived from the streak camera image. Superimposed on the image is a Gaussian fit to the data. The fit shows a r.m.s. bunch length of 0.73 mm.

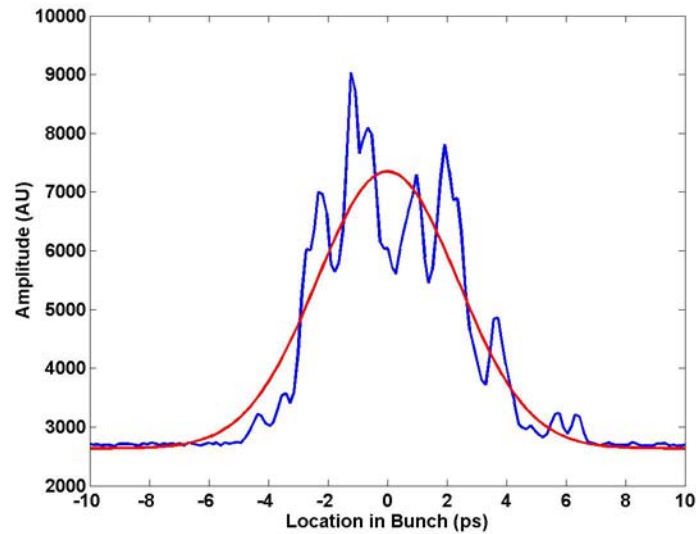


Figure 3.12.2 Gaussian fit of bunch length. A temporal lineout from streak camera data (blue) is fitted to a Gaussian profile (red). The Gaussian fit gives an r.m.s. bunch length of 0.73 mm. The graininess of the data is due to photoelectrons in the streak camera's micro-channel plate.

4 Transverse Dynamics of the Positron Beam

In this chapter the transverse dynamics of a positron beam in a plasma will be discussed. As the positron beam traverses the plasma column, the space charge field of the beam attracts the highly mobile plasma electrons. These plasma electrons disrupt the in-vacuum balance between the repulsive space charge field and the attractive self magnetic field. The transverse dynamics associated with this disruption will be presented in this chapter. First, the primary result of focusing and defocusing of the beam will be discussed. Next, the effect of a tilted beam will be analyzed with the implications of a hosing instability. Third, the effect of impact ionization will be looked at. Finally, the implications of these transverse dynamics will be discussed as they relate to the measurement of energy gain and loss on our diagnostics.

4.1 Focusing and Defocusing

The focusing mechanism for bunched relativistic beams, of either charge, is the collective reaction of the plasma electrons to the relativistically foreshortened electromagnetic field of the bunch. Even on the time scale of a few picoseconds, plasma electrons are able to move and disrupt the balance between the beam's space charge field and self magnetic field. The primary effect is a partial neutralization of the defocusing electric field of the bunch leading to a net focusing force on the beam.

In the case of an electron beam, the beam's space charge field expels the plasma electrons leaving behind a uniform ion column. The electric field of the ion column partially neutralizes the beam's space charge field. Since the majority of the electron beam "sees" this uniform ion column, the net result is a collective focusing and defocusing of the entire bunch. On the other hand, the positron beam's space charge field is neutralized by the highly mobile plasma electrons that are attracted towards the beam from different transverse positions from the beam. As a result they arrive within the beam at different times and then result in a phase mixing where each slice of the beam "sees" a different electron density, and thus a different neutralizing electric field. This phase mixing results in a highly dynamic transverse profile as the beam exits the plasma. For instance, figure 4.1.1 shows the radius of the beam as a function of longitudinal position in the bunch of a positron beam 1 meter after it exited 1.4 meters of plasma as predicted by the 3-D OSIRIS PIC code using the nominal experimental parameters as given in chapter 3. As seen in the figure, the beam has a complex longitudinal-radial profile as it exits the plasma. The transverse momentum of each beam voxel, is a function of both its longitudinal position and its radial position. The imaging spectrometer was needed to remove these transverse momentums from our energy gain measurement.

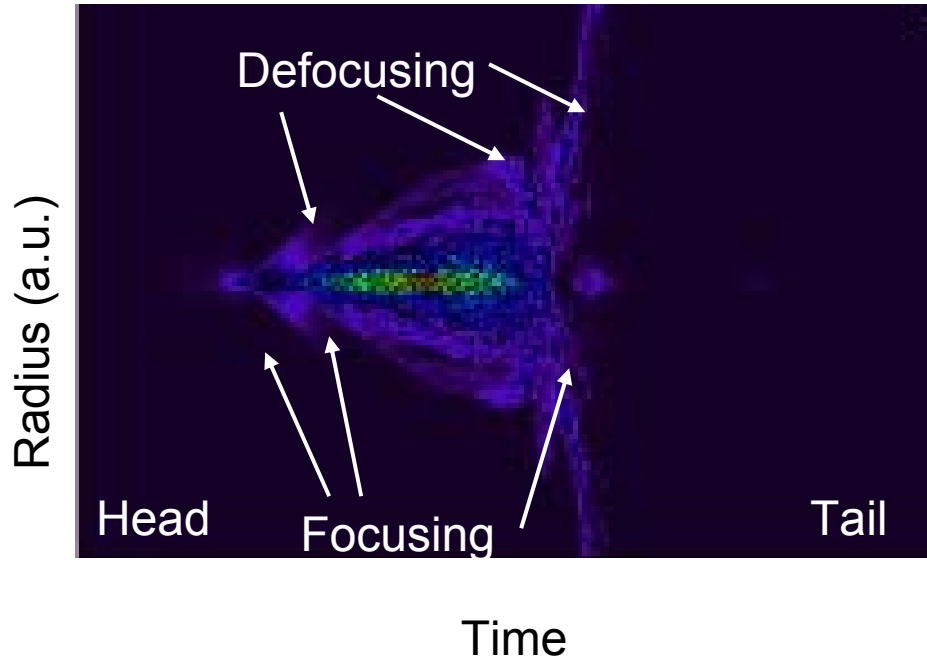


Figure 4.1.1 PIC Simulation of Positron Beam's Transverse Profile for the nominal experimental parameters. The beam is traveling from right to left in the figure. Several regions of focusing and defocusing appear simultaneously in the same bunch as it exits a plasma column. The transverse momentum of each beam voxel, is a function of both its longitudinal position and its radial position. The imaging spectrometer was needed to remove these transverse momentums from our energy gain measurement

The results of the simulation show that the temporal-radial dynamics are very complicated at higher densities ($\lambda_p \sim \sigma_z$). At much lower densities, the plasma wavelength is long enough so that the entire beam “sees” a uniform electron density. This is the so called plasma lens case. Figure 4.1.2 shows both the integrated spot size 1 meter downstream of the plasma cell as measured on the downstream optical transition radiation diagnostic (green) and the integrated spot size 12 meters

downstream as measured on the integrated Cherenkov diagnostic for densities on the order of $1\text{E}12\text{ cm}^{-3}$ (blue).

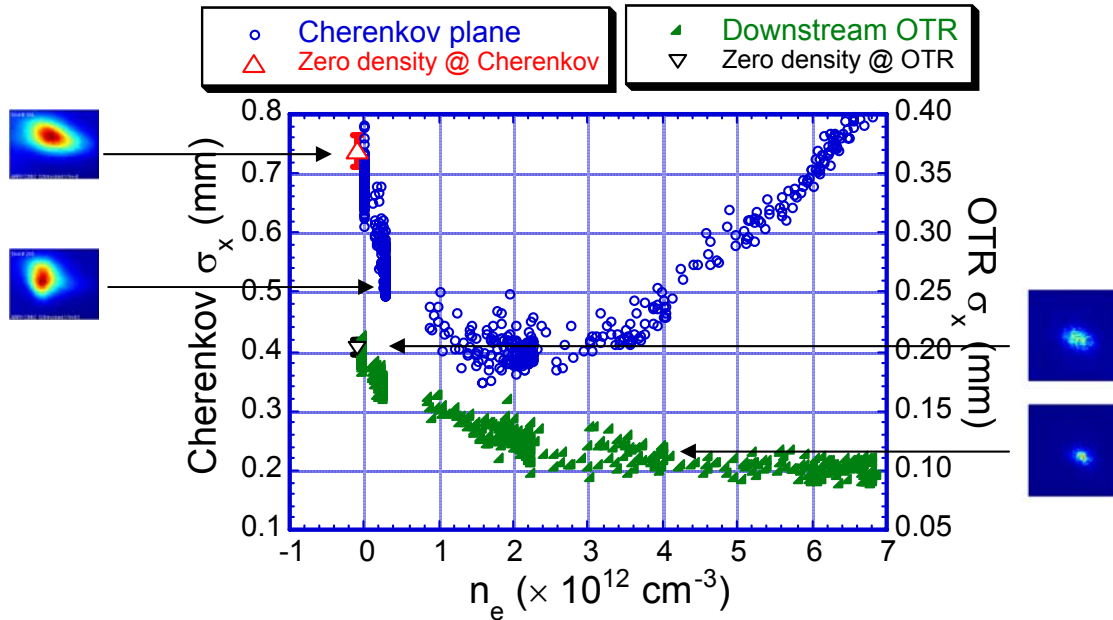


Figure 4.1.2 Integrated spot size after the plasma vs plasma density. Focusing of the positron beam is observed 1 meter downstream of the plasma (green) and 12 meters downstream of the plasma (blue). Sample images are provided of both the Cherenkov data (left) and OTR data (right). Note this data was taken at a charge of $2\text{E}10$. Although acquired at a higher charge, the physics of the plasma lens is unchanged.

As seen in figure 4.1.2, as the density is increased from 0 to $\sim 2\text{E}14\text{ cm}^{-3}$, the plasma acts as a lens and focuses the beam 12 meters away (at the Cherenkov diagnostic). As the density is further increased, and thus the focal strength of the lens is increased, the beam spot size begins to diverge at the Cherenkov as the focus is pulled towards the downstream OTR diagnostic. As the density is further increased, Hogan et. al.[15]

have shown dynamic focusing within a single positron bunch as seen on the time-resolved streak camera diagnostic.

4.2 Is there evidence of a hosing instability?

In the electron beam case, if the beam has a r-z tilt, the beam will oscillate transversely in the ion channel that is created by the beam itself. Under certain conditions, this oscillation can go unstable [41]. This instability is known as the electron hose instability. The instability arises from the interaction between the tilted beam and the walls of the ion channel. One question for our experiment was the existence (or nonexistence) of a similar instability for the positron drive beam since in this case the analogy of an ion column does not exist.

To analyze the transverse r-z dependence of the beam, a 3-D beam reconstruction analysis was developed. At the expense of losing a single shot diagnostic, a 3-D profile of the beam was developed by sampling different x-z slices (horizontal slit of streak camera) of the beam while varying y. Figures 4.2.1-3 depict how the 3-D data was generated. 4.2.1 shows an integrated Cherenkov image with the slit locations of the streak camera superimposed on the image. The method for generating the y-data is depicted in figure 4.2.2. During a run of 200 shots where the beam conditions were not changed, the beam was scanned up and down over the horizontal slit of the streak camera. The blue circles in the plot are the mean vertical positions of each shot during the run. Figure 4.2.3 shows how the x and z data were

generated. The horizontal streak camera measures the horizontal dynamics versus time (or longitudinal position). Due to jitter in the timing system and the streak camera, the horizontal streak camera image needed an absolute timing reference. The vertical streak camera image sampled the same part of the beam on every shot, so it was used as a timing reference as depicted in the figure. Now that $x, y,$ and z are known, a 3-D beam reconstruction can be made.

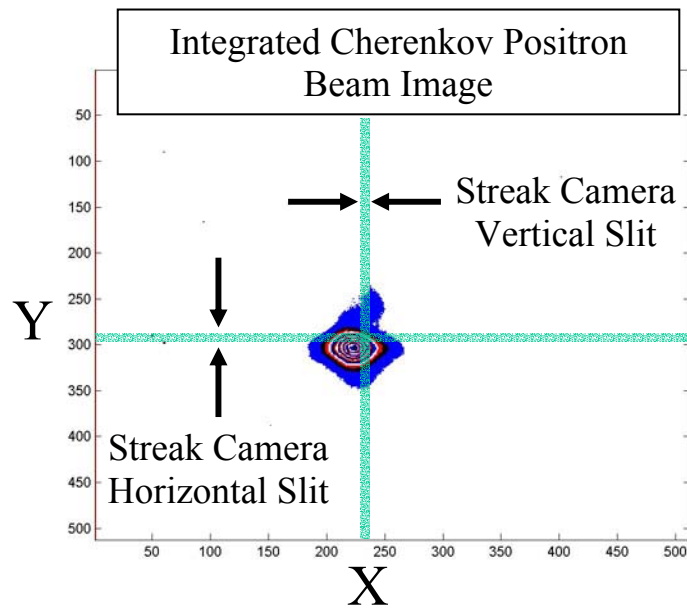


Figure 4.2.1 Slit location of beam sample

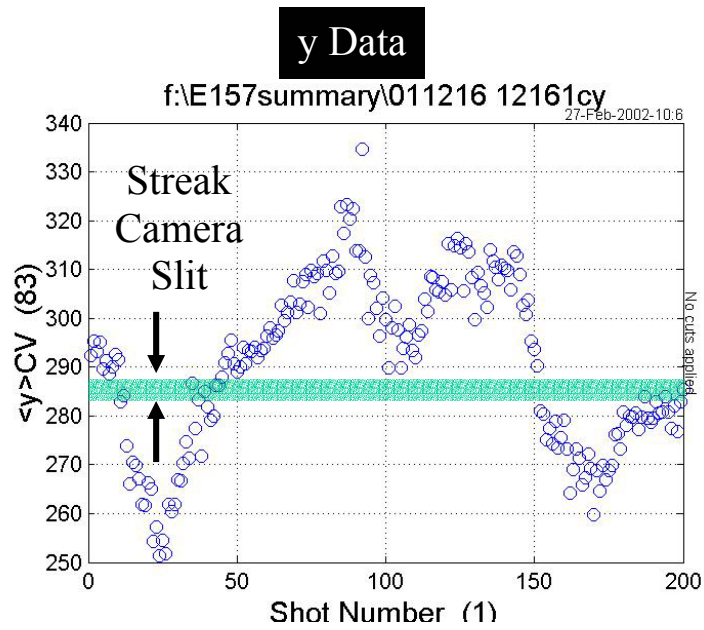


Figure 4.2.2 3-D y-data extraction from Cherenkov data

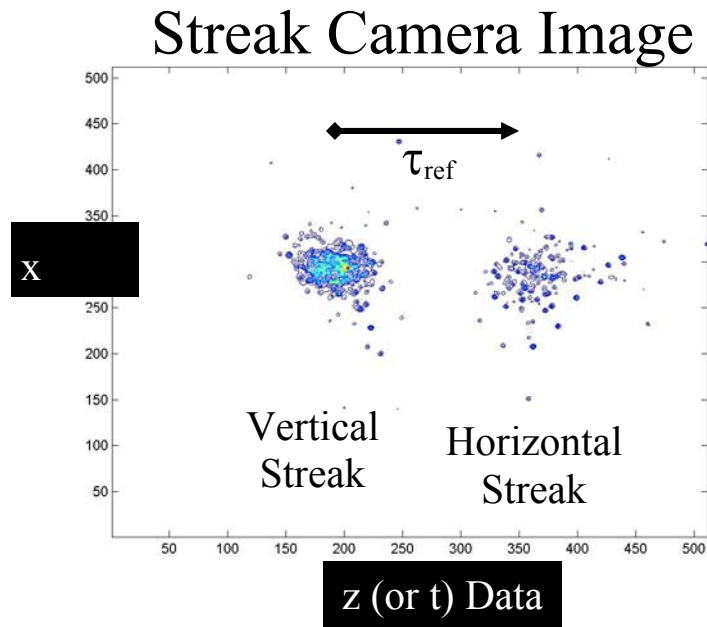


Figure 4.2.3 3-D x,z data extraction from Streak Camera data

The importance of the 3-D analysis is that it allows us to temporally resolve the dynamics of the beam without worrying which part of the beam was sampled by the slit of the streak camera since we are sampling all cross-sections of the beam. Since we are using several shots to reconstruct the beam profile, we were not able to use this reconstruction on a single shot basis.

The following figures show the results of the 3-D analysis in the dispersion free plane for a beam with $1.2E10$ positrons at two different plasma densities. The figures 4.2.4 and 4.2.5 show the beam's tilt (red), and spot size (blue) and charge distribution (black). The plasma density of figure 4.2.4 was $3E13 \text{ cm}^{-3}$ and the plasma density of figure 4.2.5 was $1.8E14 \text{ cm}^{-3}$. The change in mean position (red point) versus longitudinal position in the bunch is defined as the tilt of the beam. We can see that the beam has a tilt at both densities ($\sim 10 \mu\text{m} / \sigma_z$). What is important is that the magnitude and direction of the tilt is approximately the same at both densities. Figures 4.2.6 shows how the longitudinal beam slices evolve with increasing plasma density. The slices do not undergo any significant oscillations as their offset from the front part of the beam is nearly constant as the plasma density is increased. These measurements of the transverse dynamics in the dispersion-free plane show no evidence of hosing in our measurements, thus confirming that the measurements of energy gain and loss were due to energy changes imparted on the beam by the plasma.

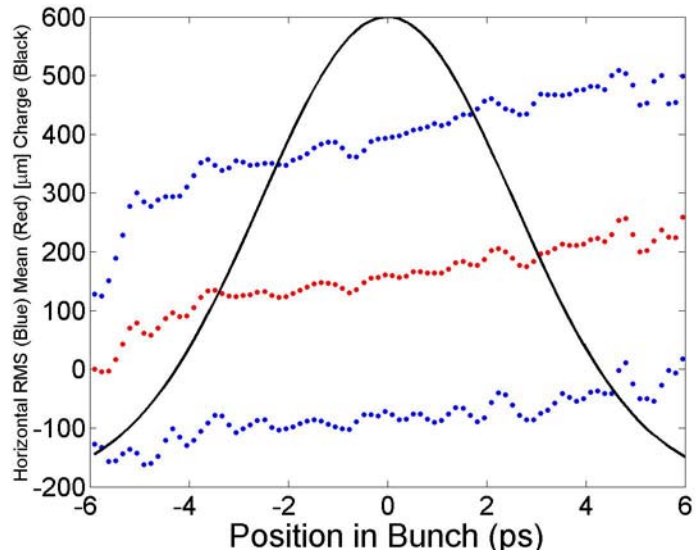


Figure 4.2.4 3-D beam analysis at a plasma density of $3E13 \text{ cm}^{-3}$

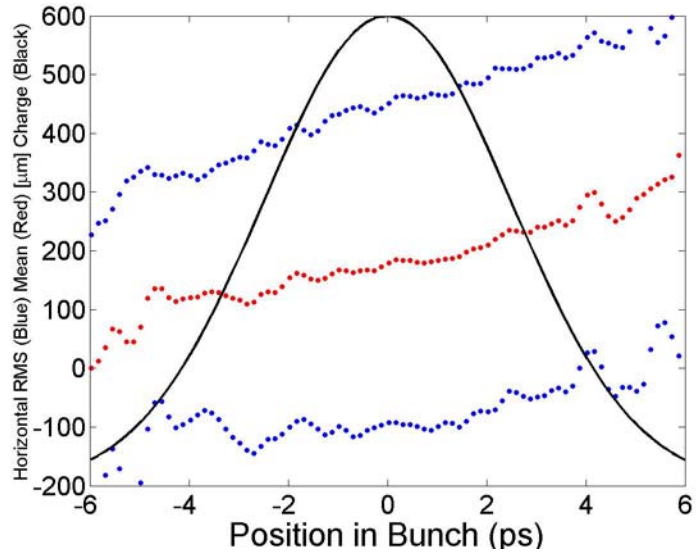


Figure 4.2.5 3-D beam analysis at a plasma density of $1.8E14 \text{ cm}^{-3}$

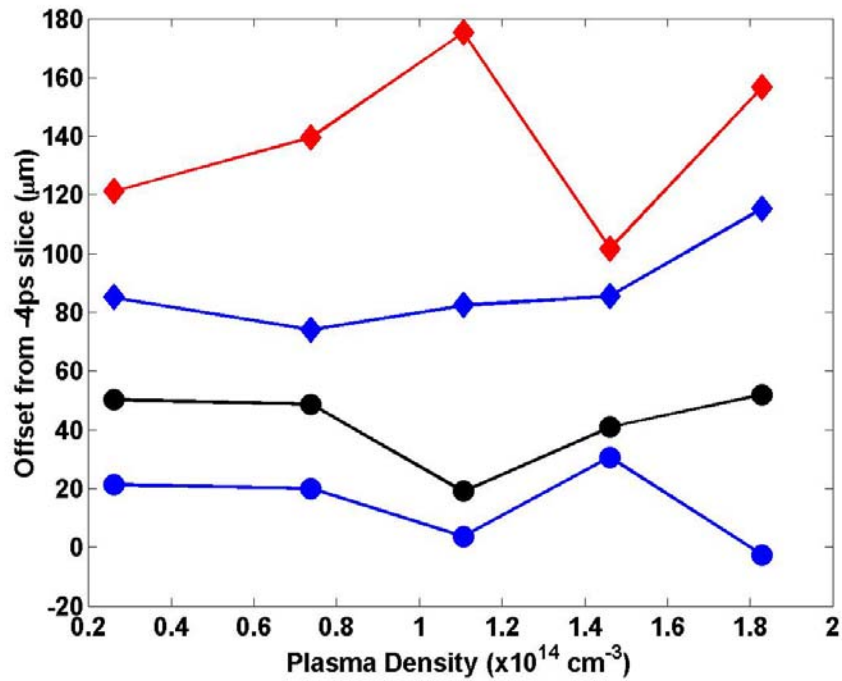


Figure 4.2.6 Oscillations of beam slices vs plasma density. The offset of the slice 3 ps in front of the centroid is labeled by blue circles. The offset of the centroid is labeled by black circles. The offset of the slice 3 ps after of the centroid is labeled by blue diamonds. The offset of the slice 5 ps after the centroid is labeled by red diamonds. The magnitude of the offset of each beam temporal slice is nearly constant and each slice does not oscillate around the -4 ps slice. Although each slice has slight fluctuations as the plasma density is increased, the slices do not gain the large offsets which would correspond to an instability.

4.3 Effects of transverse dynamics on the energy gain diagnostic

To understand how the transverse dynamics will effect our energy gain measurement, we must first understand how the imaging spectrometer (IS) will propagate the beam from the exit of the plasma to the Cherenkov radiator. First, the IS maps the position of the particles exiting the plasma onto the aerogel Cherenkov radiator. The IS does not permit any perpendicular momentum the particles have when they exit the plasma from being mapped into a position change at the aerogel. A simplified schematic of the IS is shown in figure 4.3.1.

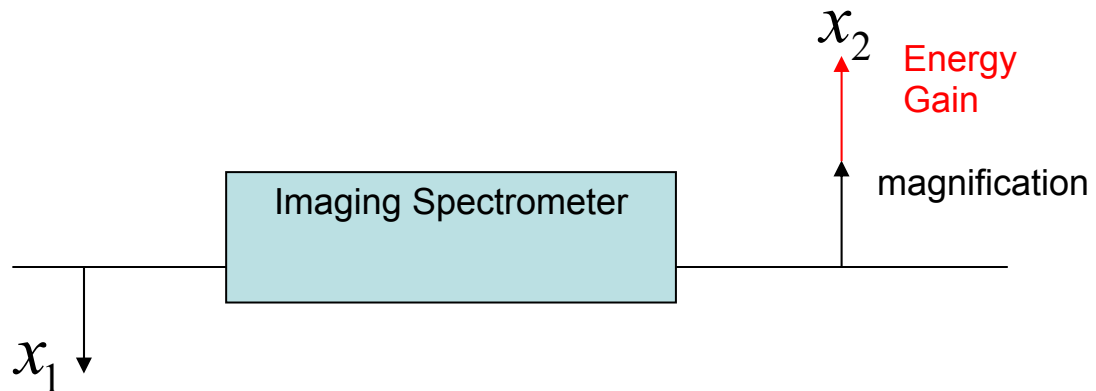


Figure 4.3.1 Imaging Spectrometer Schematic. A test particle which is initially displaced from the axis by a distance x_1 will be imaged by the spectrometer to a point where the displacement from the axis x_2 will be a function of the spectrometer magnification and of the spectrometer dispersion.

The position measured at the aerogel (x_2) is a function of the position at the exit of the plasma (x_1), the magnification of the spectrometer M , the dispersion of the spectrometer (ΔE), and the initial energy E .

$$x_2 = Mx_1 + \eta \frac{\Delta E}{E} \quad (4.1)$$

As a first approximation, we will look at how the spot size and mean position of a beam exiting the plasma are mapped onto the aerogel with no energy spread.

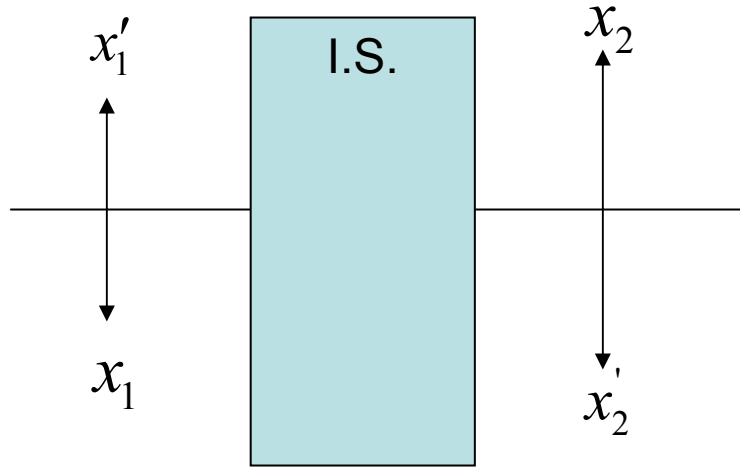


Figure 4.3.2 Gaussian propagation through the spectrometer with no energy change

The mapping of particles x_1 and x'_1 is given by

$$x_2 = Mx_1 \quad (4.2)$$

$$x'_2 = Mx'_1 \quad (4.3)$$

The spot size is given by the distance between the two particles

$$x_2 - x'_2 = M(x_1 - x'_1) \quad (4.4)$$

$$\sigma_2 = M\sigma_1 \quad (4.5)$$

The mean position is given by the average position of the two particles.

$$\frac{x_2 + x_2'}{2} = \frac{M(x_1 + x_1')}{2} = 0 \quad (4.6)$$

$$\bar{x}_2 = \bar{x}_1 = 0 \quad (4.7)$$

It follows that a beam which is centered on axis, remains on axis. The next step is to look at how the spot size and mean position are mapped when the beam has an energy change.

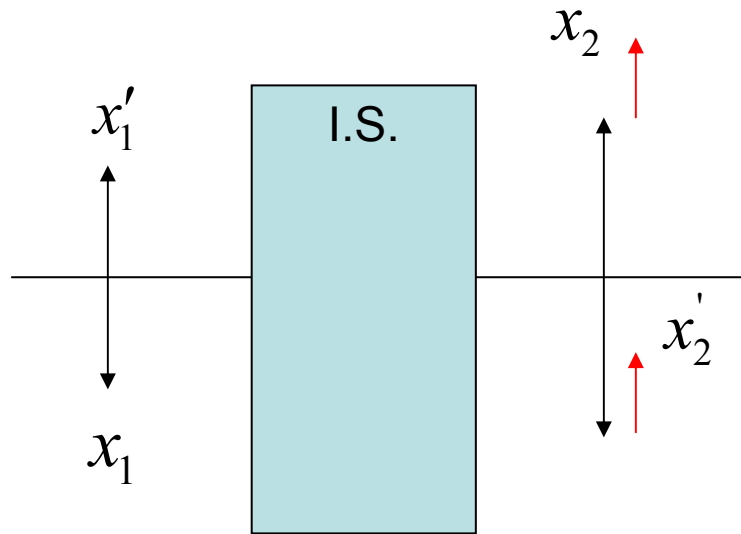


Figure 4.3.3 Gaussian propagation through the spectrometer with energy change (red)

The positions of the particles mapped through the spectrometer are

$$x_2 = Mx_1 + \eta \frac{\Delta E}{E} \quad (4.8)$$

$$x_2' = Mx_1' + \eta \frac{\Delta E}{E} \quad (4.9)$$

The spot size is given by

$$x_2 - x_2' = Mx_1 + \eta \frac{\Delta E}{E} - Mx_1' - \eta \frac{\Delta E}{E} \quad (4.10)$$

$$\sigma_2 = M(x_1 - x_1') = M\sigma_1 \quad (4.11)$$

As with no energy spread, the spot size is only affected by the magnification of the spectrometer. The change in mean position is

$$\frac{x_2 + x_2'}{2} = \frac{Mx_1 + \eta \frac{\Delta E}{E} + Mx_1' + \eta \frac{\Delta E}{E}}{2} \quad (4.12)$$

$$= \frac{M(x_1 + x_1')}{2} + \eta \frac{\Delta E}{E} = 0 + \eta \frac{\Delta E}{E} \quad (4.13)$$

$$\bar{x}_2 = \eta \frac{\Delta E}{E} \Rightarrow \Delta E = \frac{\bar{x}_2 E}{\eta} \quad (4.14)$$

As expected, the change in energy is mapped into a change in position. Finally we look at how a beam which is off axis is mapped onto the aerogel. This is analogous to a tilted beam where the head defines the axis and the tail is offset from the axis.

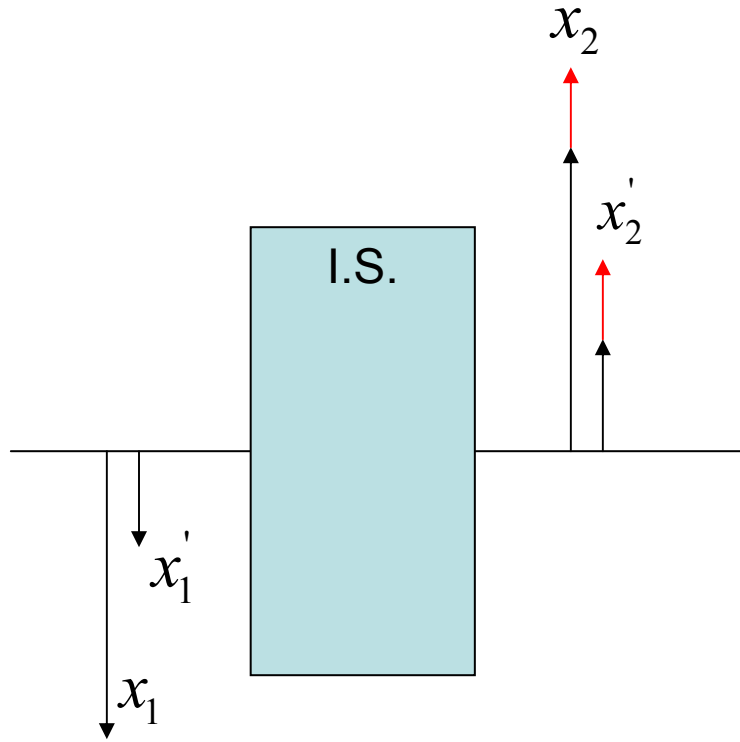


Figure 4.3.4 Gaussian propagation with an energy change and offset

The mapping of the particles is the same as equations 4.8 and 4.9 and the spot size calculation is the same as the case in which a beam is on axis. The calculation for the mean position as measured at the aerogel is

$$\frac{x_2 + x_2'}{2} = \frac{Mx_1 + \eta \frac{\Delta E}{E} + Mx_1' + \eta \frac{\Delta E}{E}}{2} \quad (4.15)$$

$$= \frac{M(x_1 + x_1')}{2} + \eta \frac{\Delta E}{E} \equiv Mx_{Tilt} + \eta \frac{\Delta E}{E} \quad (4.16)$$

$$\bar{x}_2 = Mx_{Tilt} + \eta \frac{\Delta E}{E} \quad (4.17)$$

$$\Delta E = \frac{E}{\eta} (\bar{x}_2 - Mx_{Tilt}) \quad (4.18)$$

From equation 4.18 we see that the apparent energy change will be altered by an initial tilt on the beam. Therefore the observed energy change will be due to the tilt, the initial energy spread, and the tilt on the beam.

$$\Delta E_{observed} = \Delta E_{plasma} + \Delta E_{Initial} + \frac{M\bar{x}_T E}{\eta} \quad (4.19)$$

$$\bar{x}_2 = M\bar{x}_{TPlasma On} + \eta \frac{\Delta E_{Initial}}{E} + \eta \frac{\Delta E_{Plasma}}{E} \quad (4.20)$$

The goal of our experiment is to measure the energy change induced by the plasma. To do this we must remove the initial energy spread and contribution of the tilt from our measurements. We do this by looking at the plasma off case where the measured position is given by

$$\bar{x}_{2np} = M\bar{x}_{Tnp} + \eta \frac{\Delta E_{Initial}}{E} \quad (4.21)$$

Since the beam does not hose to any measurable extent, the ratio of the plasma on to plasma off tilts is given by the ratio of the respective spot sizes.

$$\frac{\bar{x}_{Tnp}}{\bar{x}_{Tp}} = \frac{\sigma_{xnp}}{\sigma_{xp}} \quad (4.22)$$

Now solving for the mean plasma off position in terms of the plasma on tilt.

$$\bar{x}_{2np} = M \frac{\sigma_{xnp}}{\sigma_{xp}} \bar{x}_{Tp} + \eta \frac{\Delta E_{Initial}}{E} \quad (4.23)$$

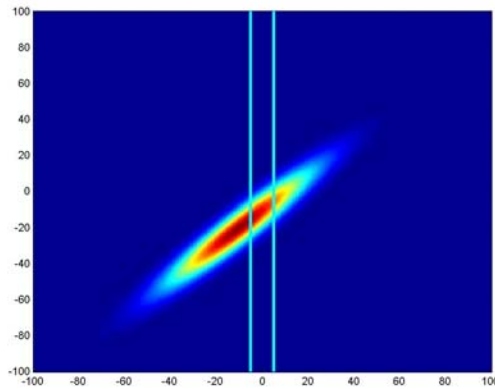
$$\bar{x}_{Tp} = \frac{\bar{x}_{2np} \sigma_{xp}}{M \sigma_{xnp}} - \eta \frac{\sigma_{xp}}{M \sigma_{xnp}} \frac{\Delta E_{Initial}}{E} \quad (4.24)$$

Substituting equation 4.24 into 4.20 yields the measured plasma position at the aerogel in terms of the plasma off case, the energy spread, and the change induced by the plasma.

$$\bar{x}_2 = \frac{\bar{x}_{2np} \sigma_{xp}}{\sigma_{xnp}} + \eta \left(1 - \frac{\sigma_{xp}}{M \sigma_{xnp}} \right) \frac{\Delta E_{Initial}}{E} + \eta \frac{\Delta E_{Plasma}}{E} \quad (4.25)$$

From this equation, we can interpret how a shift in position on the aerogel corresponds to a change in beam energy. The first term is due to the tilt on the beam. The second term is due to the initial energy spread. The final term is due to the plasma induced energy change. Since we measure the change in position, we needed to reduce the beam tilt and the energy spread. The majority of time spent on our experiment was spent minimizing these parameters so that an accurate measurement of energy gain and loss could be made.

Another consequence of positron focusing is how a focused beam can appear to have a change in energy on our streak camera diagnostic. Figure 4.3.5 shows a x-y slice of the beam. The slit of the streak camera is superimposed on the image.



$$\sigma_{x'_1} = 5 \quad \sigma_{x'_2} = 30$$

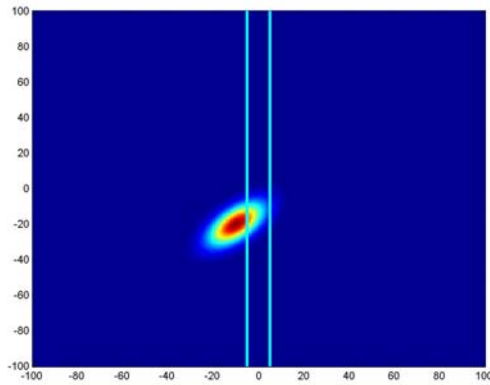
$$\bar{x}'_1 = -10 \quad \bar{x}'_2 = -20$$

$$\theta = 45^\circ$$

$$\bar{y}_{SC} = -11.7$$

Figure 4.3.5 Unfocused tilted offset beam on streak camera slit. The measured mean position on the streak camera slit (space between the blue vertical lines), was -11.7 (the units are arbitrary).

Three conditions are placed on the beam. First it is asymmetric. That means that one axis has a much greater width than the other axis. Second, the beam is tilted. In the above figure, the beam has a tilt of 45 degrees. The third condition is that the centroid of the beam is offset from the center of the slit. As seen in the above figure, the measured centroid mean position on the slit of the streak camera is -11.7. Figure 4.3.6 shows the same beam as it is focused. The measured mean position on the streak camera is -15.4. This analysis shows how simple focusing of the beam could appear to be energy gain on our streak camera diagnostic and thus the importance of alignment for accurate analysis of the energy gain results.



$$\sigma_{x'_1} = 5 \quad \sigma_{x'_2} = 10$$

$$\bar{x}'_1 = -10 \quad \bar{x}'_2 = -20$$

$$\theta = 45^\circ$$

$$\bar{y}_{SC} = -15.4$$

Figure 4.3.6 Focused, tilted offset beam on streak camera slit. The mean position as measured on the streak camera slit (the space between the light blue vertical lines) was -15.4. The shift in mean position between the focus and unfocused beams was 3.7 units. Energy changes imparted on the beam by the plasma will change the mean position of the beam on the streak camera diagnostic. This analysis has shown how simple focusing of the beam would shift the mean position and thus giving the appearance of an energy change. To negate this effect, the center of the beam must be aligned to the center of the streak camera slit.

5 Longitudinal Dynamics of the Positron Beam in a Meter Long Plasma Column

In this chapter we present the analysis of the longitudinal dynamics of the positron beam. Two significant experimental results will be presented. First, results on energy loss of the bulk of the beam will be presented. Secondly, and more importantly, energy gain of the particles in the back of the beam will be presented.

5.1 Energy loss

A primary indicator that the positron beam is driving, and thus transferring energy to, a plasma wakefield is the observation of energy loss of the bulk of the beam. The energy loss of the beam was measured after the plasma by dividing the entire energy-dispersed streak camera image into 1 ps slices (the temporal resolution of the streak camera), fitting a Gaussian profile to the data of each slice, and tracking the relative position of each Gaussian's mean. The plasma density was varied between $0-2 \times 10^{14} \text{ cm}^{-3}$ over a series of 200 shots. The ionizing laser was not fired every fourth shot to provide a baseline measurement of incoming beam parameters and to provide the data for zero plasma density. The measured mean positions were binned by plasma density. Figure 5.1.1 shows the energy loss as measured on the streak camera. The error bars represent the standard deviation of the mean of the energy (vertical error bars) and plasma density (horizontal error bars) for each density bin.

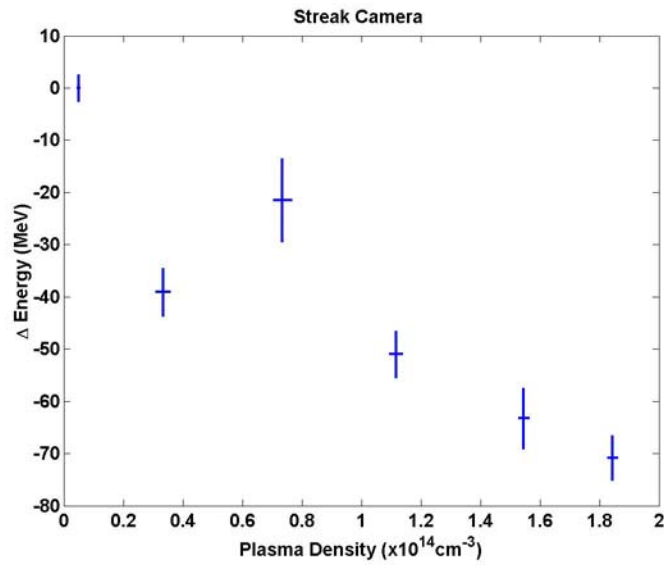


Figure 5.1.1 Energy Loss vs. Plasma Density Measured on the Streak Camera

The above figure shows that the beam loses energy with increasing plasma density. The data shows some structure where the beam loses less energy at $8 \times 10^{13} \text{ cm}^{-3}$ than it did at $3 \times 10^{13} \text{ cm}^{-3}$. This is not consistent with our intuition or with the simulations. One assumption in the above figure is that the incoming beam energy was constant over the 200 shots. We verify this assumption by looking at a beam position monitor (BPM) in a dispersive section of the beamline upstream of the plasma. This BPM measures the changes in the incident beam energy. These variations are plotted in figure 6.1.2 and the error bars have the same meaning as before.

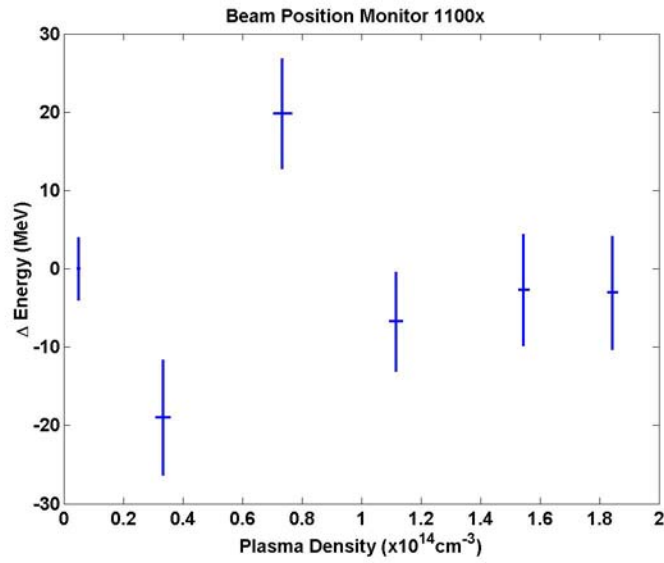


Figure 5.1.2 Variations in the Incident Beam Energy

The above figure shows that our assumption for constant incoming energy was not valid. The energy is seen to vary by up to 20 MeV. This is a small fraction of the 28.5 GeV, but it is significant for our measurements. Therefore, to get the actual energy loss induced by the plasma on the beam, we subtract the incident energy from the energy measured after the plasma (at the streak camera). This result is shown in figure 6.1.3.

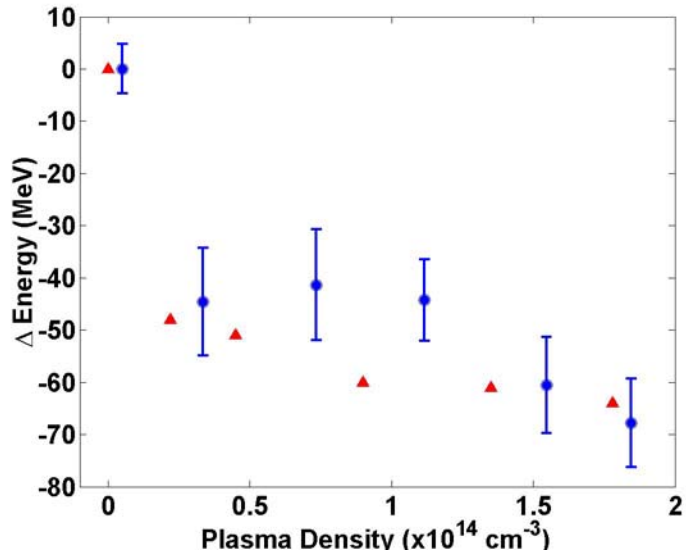


Figure 5.1.3 Peak energy loss after propagating through 1.4 meters of plasma

Energy loss measurements over a wide range of plasma densities are presented in Figure 6.1.3 (blue circles). Figure 5.1.3 also shows the energy loss predictions from 3-D PIC simulations (red triangles). As can be seen in Figure 5.1.3, simulations predict and experimental data confirm that the beam losses energy in the plasma. The energy loss gradually increases with increasing plasma density with a maximum measured energy loss of 68 ± 8 MeV at a plasma density of $1.8 \times 10^{14} \text{ cm}^{-3}$. This is in good agreement with 3-D OSIRIS simulations which predicted a peak energy loss of 64 MeV at the same plasma density.

5.2 Energy Gain

Since the plasma wakefield is an energy transformer, the energy loss data strongly suggests that the particles in the beam's tail should gain energy in this experiment as the beam length approaches $\pi c/\omega_p$ or half the plasma wakefield wavelength. As opposed to the energy loss of the beam, which can be measured at plasma densities as low as $3 \times 10^{13} \text{ cm}^{-3}$, the energy gain of the "tail particles" can only be observed for densities greater than $\sim 1.5 \times 10^{14} \text{ cm}^{-3}$. For densities less than $1.5 \times 10^{14} \text{ cm}^{-3}$, the plasma wakefield wavelength is too long for the wake to accelerate enough beam charge to be measured with the limited dynamic range of the streak camera. Temporal resolution of the beam was only possible between the -4 ps slice and the 5 ps slice due to the signal-to-noise ratio (i.e. limited dynamic range) in the streak camera. Figure 5.2.1 shows the amplitude of the slices up to 10 ps away from the centroid. The red box represents the region in which the amplitude of slice was insufficient to extract a meaningful signal. Therefore, the first and last slices measured on the streak camera are not the true head and tail of the beam. Rather, they represent slices which lie $\sim 2 \sigma_z$ before and after the centroid. Figures 5.2.2-3 depict the -6 ps slice to give an example of a slice which has an insufficient signal. Figure 5.2.2 is the raw data with the -6 ps region bounded by the two lines. Figure 5.2.3 shows the analysis of that data. The blue curve is the raw data, the green curve is Gaussian smoothed data, the dashed red line is the Gaussian fit approximation, and the

solid red curve is the Gaussian fit to the green smoothed data. As seen in the figure, the streak camera raw data consists of just a few photoelectrons. The signal consists of two spikes and the total count level is very low. In addition, the Gaussian fit to the signal is poor. These are the reasons why we say that this data is categorized as being below the signal-to-noise ratio threshold. Figures 5.2.4-5 show an example of data which is just above the signal-to-noise threshold. Figure 5.2.4 shows the raw data for the 5 ps slice and figure 5.2.5 shows the analyzed slice data where the different colored lines have the same meaning as figure 5.2.3. In this case, you can see that the peak counts are much higher than the previous case and that there is significantly more signal. In addition, the Gaussian fits the data well.

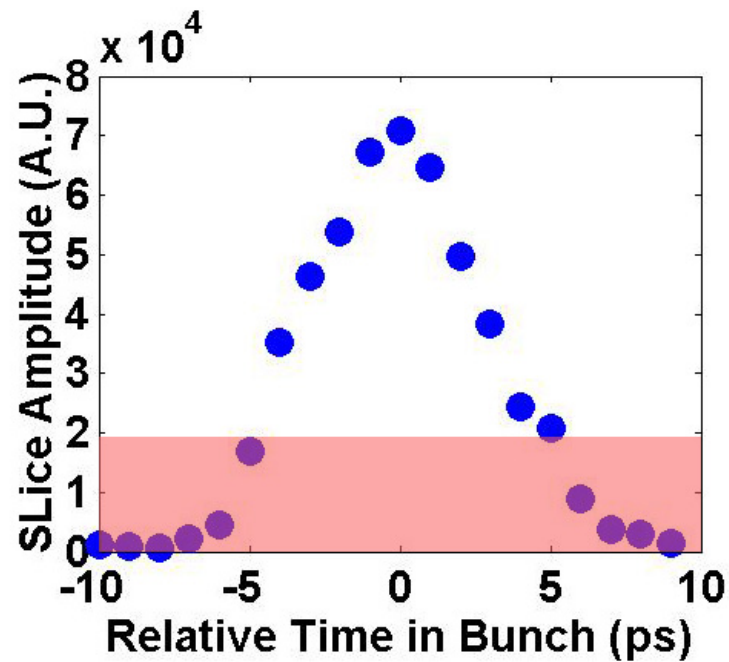


Figure 5.2.1 Amplitude of Slice Data From the Streak Camera

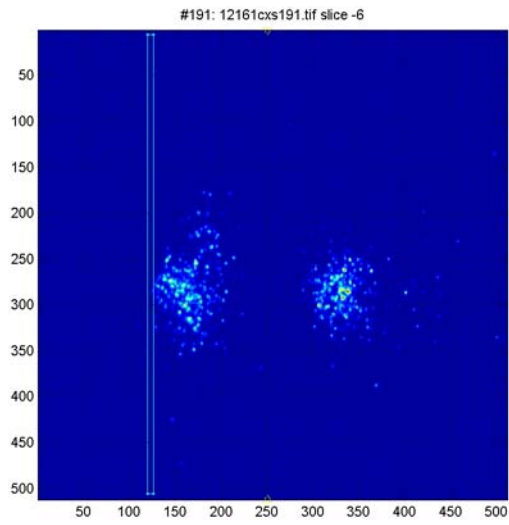


Figure 5.2.2 Raw data of -6 ps slice

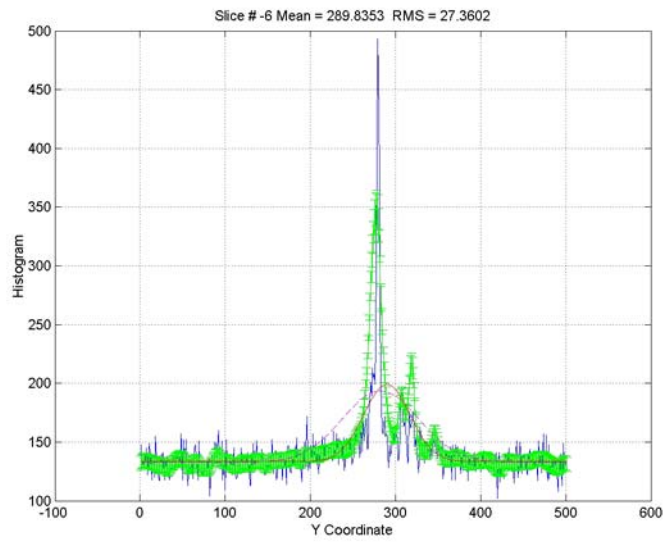


Figure 5.2.3 Slice Analysis of -6 ps slice

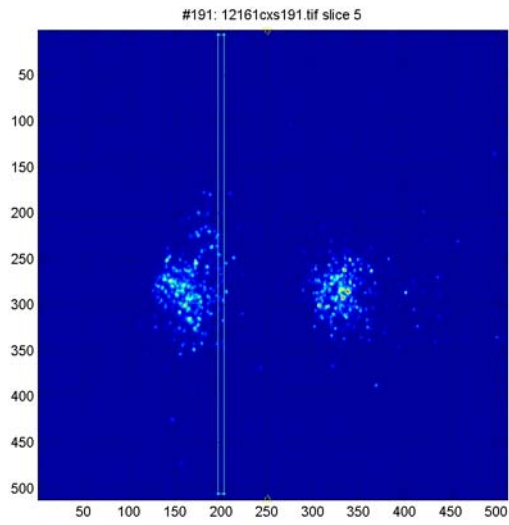


Figure 5.2.4 Raw Data of 5 ps Slice

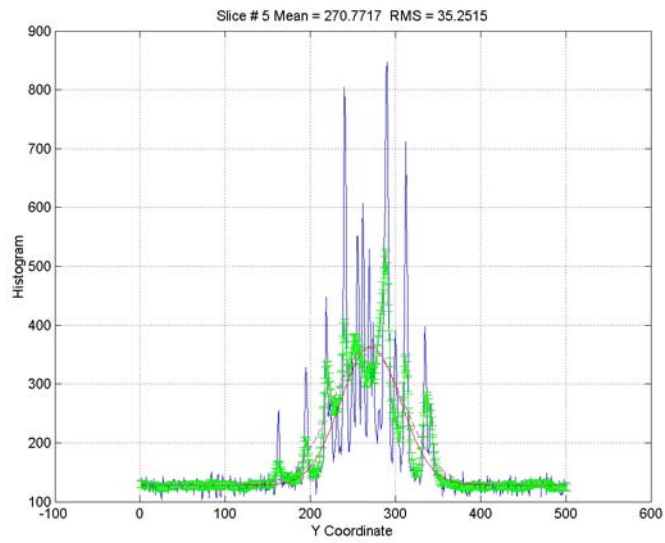


Figure 5.2.5 Slice Analysis of 5 ps slice

The above analysis showed which slices of the streak camera data were not usable. Now we will concentrate on the part of the data that we can use. The first step was to find data which did not have a tail, was not tilted, and had a small energy spread. A 200 shot run which took place on December 16, 2001 fit the above criterion. This run, 12161cx, was used for this analysis.

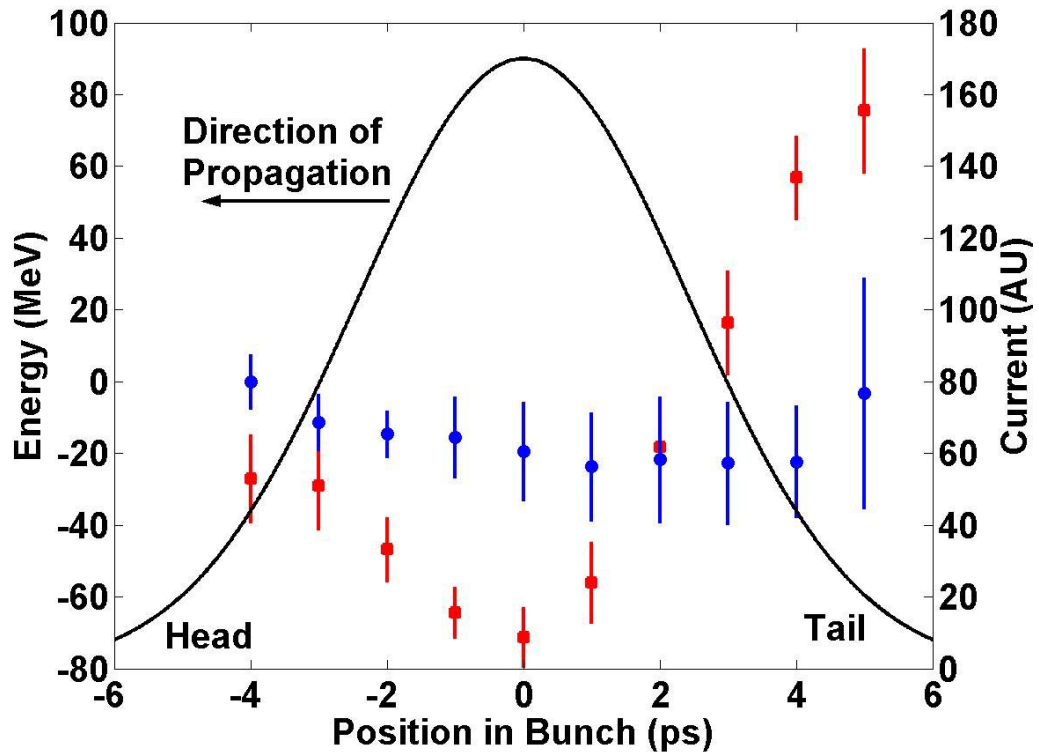


Figure 5.2.6 Time Slice Analysis of the Energy Dynamics with a Positron Bunch

Figure 5.2.6 shows the relative energy of each time slice along the bunch of the positron beam when the plasma is off (blue circles) and when the plasma turned on

(red squares) with a density of $1.8 \times 10^{14} \text{ cm}^{-3}$. The energy variation in time for each shot was obtained by dividing the energy-dispersed streak camera images into 1 ps slices and tracking the mean positions (energy) of each slice. The vertical error bars represent the standard deviation of the mean for each temporal bin. The raw images that comprise Figure 5.2.6 are all documented in Appendix B. The black line is the charge distribution of the bunch which is moving from right to left in the figure. Since the change in energy is important, not the absolute energy, energy changes were measured with respect to the -4 ps plasma off slice. The plasma off case shows that the beam has a head-to-tail energy chirp of $\sim 20 \text{ MeV}$. With the plasma on, energy loss is observed for the bulk of the beam out to about one σ_z behind the centroid. The positrons behind this point have gained energy. The data show that $\sim 5 \times 10^8$ positrons in a 1 ps slice $1.6 \sigma_z$ after the centroid were accelerated by $79 \pm 15 \text{ MeV}$ in 1.4 m ($\sim 56 \text{ MeV/m}$ gradient). These results are in good agreement with 3-D PIC simulations which predicted a peak energy gain of 78 MeV. The maximum energy loss in the simulations occurred at about -1.5 ps whereas in the experiment the 0 ps slice (i.e. the beam's center slice) shows the greatest loss. This is thought to be due to small differences between the actual beam current profile and the fitted Gaussian current profile that was used in the simulations and also due to space charge broadening effects in the streak camera.

6 Conclusions

In summary, this dissertation demonstrates the first acceleration of positrons by a plasma wakefield. Excellent agreement was found between the experimental results and those from 3D PIC simulations for both energy gain and loss. Energy loss of the centroid was found to increase with increasing plasma density up to a value of ≈ 68 MeV at a plasma density of $1.8 \times 10^{14} \text{ cm}^{-3}$. At this density, energy gain of positrons in a plasma of 79 MeV was measured. The acceleration gradient of 56 MeV/m measured in this proof-of-principal experiment can be increased to the GeV/m level in future experiments by a combination of an increase in the drive beam charge, a decrease in the drive beam pulsewidth (with a corresponding increase in the plasma density), and by employing a plasma channel rather than a uniform plasma. Furthermore, in a real application of such a plasma wakefield accelerator, the drive positron bunch will be followed by an optimally placed trailing witness bunch with a sufficient current to both realize high gradient acceleration and a reasonable beam load and narrow energy spread. These scalings have been explored through PIC simulations. These results and future experiments will be the basis of work to design a plasma-based linear collider which will either utilize multiple plasma wakefield accelerator sections or an extremely high-gradient single stage plasma wakefield “afterburner” at the end of an existing linac to double the energy of the electron and positron beams.

Appendix A: Experimental Facilities

A.1 Stanford Linear Accelerator (SLAC)

Before a description of the E157/E162 experimental components is given, a brief introduction to SLAC is necessitated. SLAC is operated under contract from the United States Department of Energy (DOE) as a national basic research laboratory. Its function is to probe the structure of matter at the atomic scale with x-rays and at much smaller scales with electron and positron beams. The major facilities at SLAC are the linac, End Station A, SPEAR and SSRL, PEP II, SLC, and the FFTB. The linac is a three kilometer long accelerator capable of producing electron and positron beams with energies up to 50 GeV. End Station A is for fixed target experiments. Early work in End Station A showed that the constituents of the atomic nucleus, the proton and neutron, are themselves composed of smaller, more fundamental objects called quarks. The Stanford Synchrotron Radiation Laboratory (SSRL) uses the SPEAR storage ring to produce intense x-ray and ultraviolet beams for probing matter on the atomic scale. PEP II is a storage ring for a B meson factory in which an experiment, BaBar, is seeking to answer why the universe is made of matter and not anti-matter. The Stanford Linear Collider (SLC) in conjunction with the Stanford Large Detector (SLD), analyzed collisions of 50 GeV electrons on 50 GeV positrons in order to determine the mass and other properties of the Z^0 particle, which is a carrier of the weak force of subatomic physics. The Final Focus Test Beam (FFTB) is a facility for

research on future accelerator design. The E162 experiment was located inside the FFTB.

A.2 Linac Beam Transport

The function of the linac was to deliver short high-charge 28.5 GeV bunches of positrons and electrons to our experiment. Precise tuning of the beams orbit is needed in order to transport the bunch with good beam quality. One deleterious effect which tuning minimizes is wakefields. Wakefields act as the feedback mechanism in the linac in which the beam undergoes transverse deflections due to its own space charge field. The strength of this wakefield scales as the bunch charge squared which means that it is increasingly more difficult to transport a higher charge bunch with good beam quality. The linear accelerator is capable of transporting bunches which contain 4×10^{10} particles, but it requires continuous tuning in order to maintain that charge.

Our experiment was designed for a bunch which contained 2×10^{10} positrons. Since the effect of the plasma on the beam is a strong function of the beam's incoming parameters, an extremely high quality beam was needed to make the precise energy gain measurements. The charge was lowered from the design of 2×10^{10} down to 1.2×10^{10} and with a significant tuning effort by SLAC's Main Control, a high quality bunch was delivered to our experiment in the FFTB. The following four figures show the differences between the high and low charge beams with and without a plasma.

As you can see, the low charge beam has very little energy spread, it is round, and it “behaves” nicely when it is propagated through the plasma.

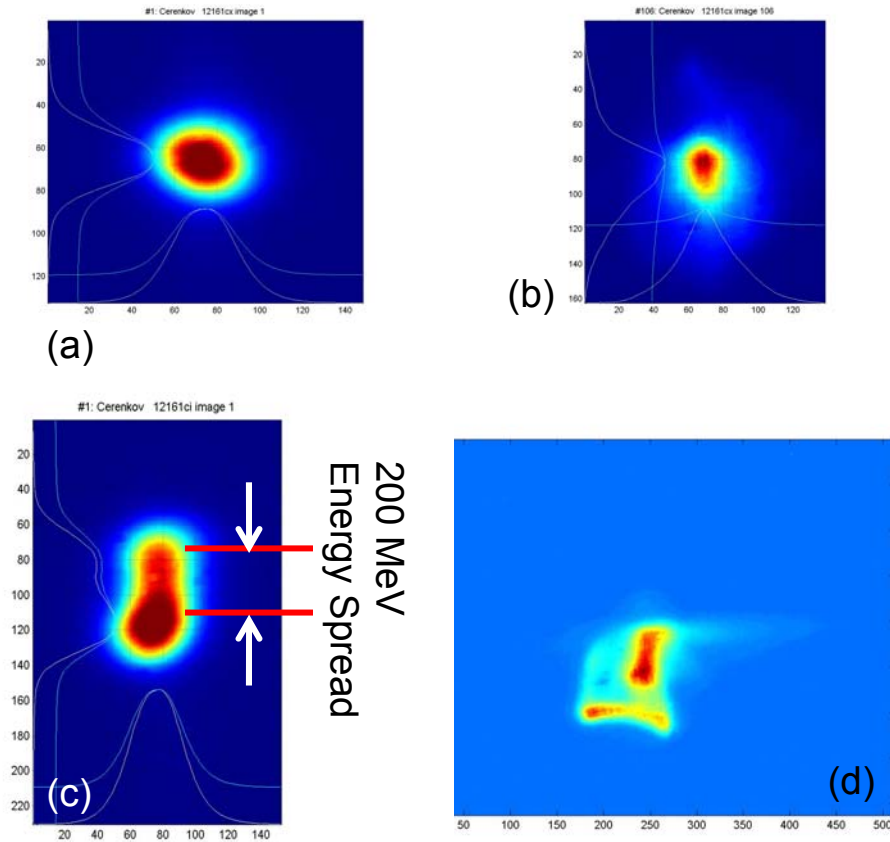


Figure A.2.1 Improved beam quality at lower charge. These four images are time integrated Cherenkov images. There is energy dispersion in the vertical axis of these images. **a** and **b** show the beam with a low charge ($1.2 \times 10^{10} e^+$) without **a** plasma and **b** with a $2 \times 10^{14} e^- / cm^3$ plasma. As you can see, the beam is well behaved and is not degraded by the plasma. **c** and **d** show the beam at a high charge ($2.0 \times 10^{10} e^+$) without **c** plasma and **d** with a $2 \times 10^{14} e^- / cm^3$ plasma. As you can see the beam has an initial large energy spread, and is severely degraded when it propagates through the plasma.

A.3 Final Focus Test Beam (FFTB)

The FFTB was designed to be a facility to be used for the development and study of optical systems, instrumentation, and techniques needed to produce the small beam spot sizes required for future electron-positron colliders. The design consists of five key sections. The first part is a matching section to match the beam that appears at the end of the linac to the lattice of the FFTB beamline. This matching section also has a lens to match the betatron space of the beam to the second section, the chromatic correction section. The second, third, and fourth sections are used to correct chromatic and geometric aberrations on the beam. The final section is a telescope that focuses the beam down to a small spot size.

The optics of the FFTB consist of dipoles, quadruples, and sextuples. In order to focus the beam down to nanometer spot sizes, the optics needed to be aligned to an accuracy on the order of a micron. The optics were mounted on 3-axis positioners that allowed the optics to be moved $\pm 1\text{mm}$ with 300nm resolution. To complement these optics, diagnostics were needed to determine the spot size and position of the beam along the beamline. These include torroids (to measure the beam's charge), wire scanners (to measure spot size), a dispersive section to measure the incoming beam energy, and BPMs (to measure the beam's position, Sec. 4.11).

Appendix B: Compendium of Analyzed Images

In this appendix, raw data images are presented. The 9 shots chosen represent the shots used for the energy gain analysis in Chapter 6. Six images are displayed for each shot. The key to each figure is given in figure B.0.

The first image (top left) is from the upstream OTR diagnostic. This records the incoming beam profile 1 meter before the plasma cell. The units of each axis are pixels and each pixel represents $9\mu\text{m}$. The y-axis is the beam line y-axis and the x-axis is the inverse of the beam line x-axis. The lines represent the horizontal and vertical profiles of the beam.

The second image (top right) is from the downstream OTR diagnostic. This records the beam profile 1 meter after the plasma cell. The units of each axis are pixels and each pixel represents $9\mu\text{m}$. The y-axis is the beam line y-axis and the x-axis is the beam line x-axis. The lines represent the horizontal and vertical profiles of the beam.

The third image (the middle left image) is the integrated Cherenkov diagnostic. The units of each axis are pixels and each pixel represents $16\mu\text{m}$. The vertical axis is the beam line y-axis which is energy dispersive (each pixel represents 5 MeV of energy change). The x-axis is the beam line x-axis. Superimposed on the image are two line pairs. The area in between each line pair represents the area of the image which is sampled by the streak camera slit.

The fourth image (the middle right image) is the raw streak camera data. The units of each axis are pixels and each pixel represents $16\mu\text{m}$. The x-axis of the image is time which increases from left to right. The left image is the vertical or energy dispersive image while the right image is the time resolved dispersion free image. The boxes drawn around each image are the close ups presented in the next two figures. Superimposed on the image is the shot number and the plasma density for that shot.

The fifth image (bottom left) is the close up view of the energy dispersed streak camera image. The head of the beam is on the left and the tail is on the right. Superimposed on the image are the mean positions of Gaussian fits to 1 ps bins (circles) and a line in which each point is the center of mass calculation for each data column.

The sixth image (bottom right) is the close up view of the dispersion free streak camera image. The head of the beam is on the left and the tail is on the right. Superimposed on the image are the mean positions of Gaussian fits to 1 ps bins (circles) and a line in which each point is the center of mass calculation for each data column.

This data was acquired on December 16, 2001. The run code was 12161cx. The run consisted of 200 shots where the plasma density was varied between 0 and $2 \times 10^{14} \text{ e}^- / \text{cm}^3$. The ionizing laser was not fired every fourth shot so that the plasma free beam parameters could be recorded. This appendix shows the raw data which

was used to construct the energy gain figure in Chapter 6. The plasma off parameters consist of the average measurements made from shots 185, 189, and 193. The plasma on parameters consist of the average measurements made from shots 186, 187, 188, 190, 191, and 192.

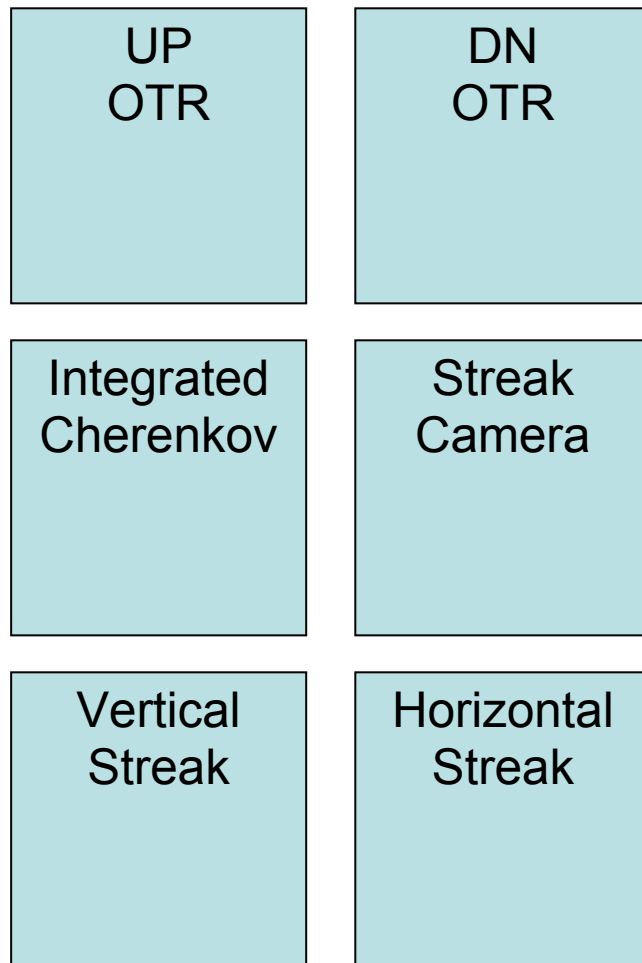


Figure B.0 Image locations in the following figures.

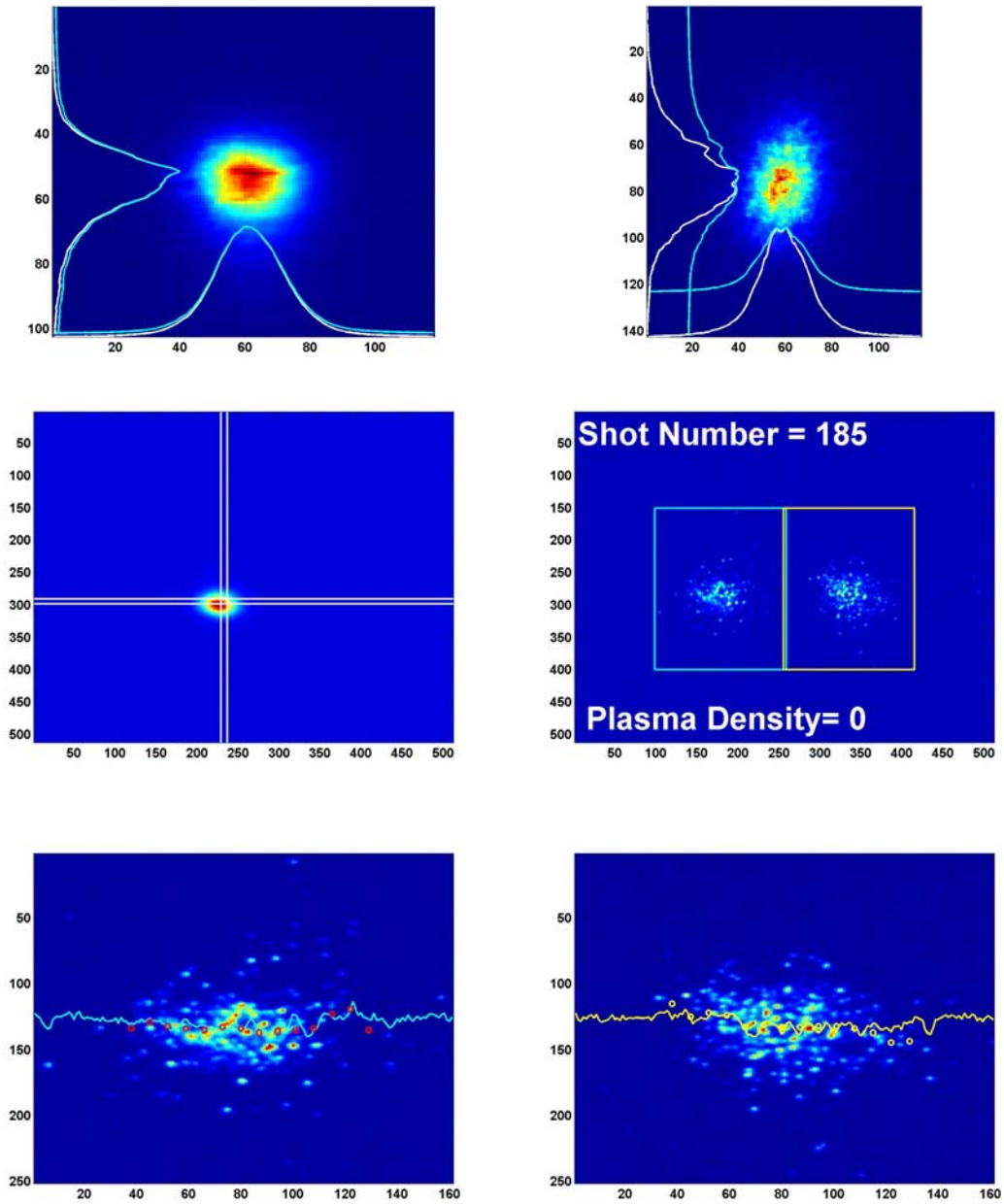


Figure B.1 Shot 185 – No Plasma – Raw Images.

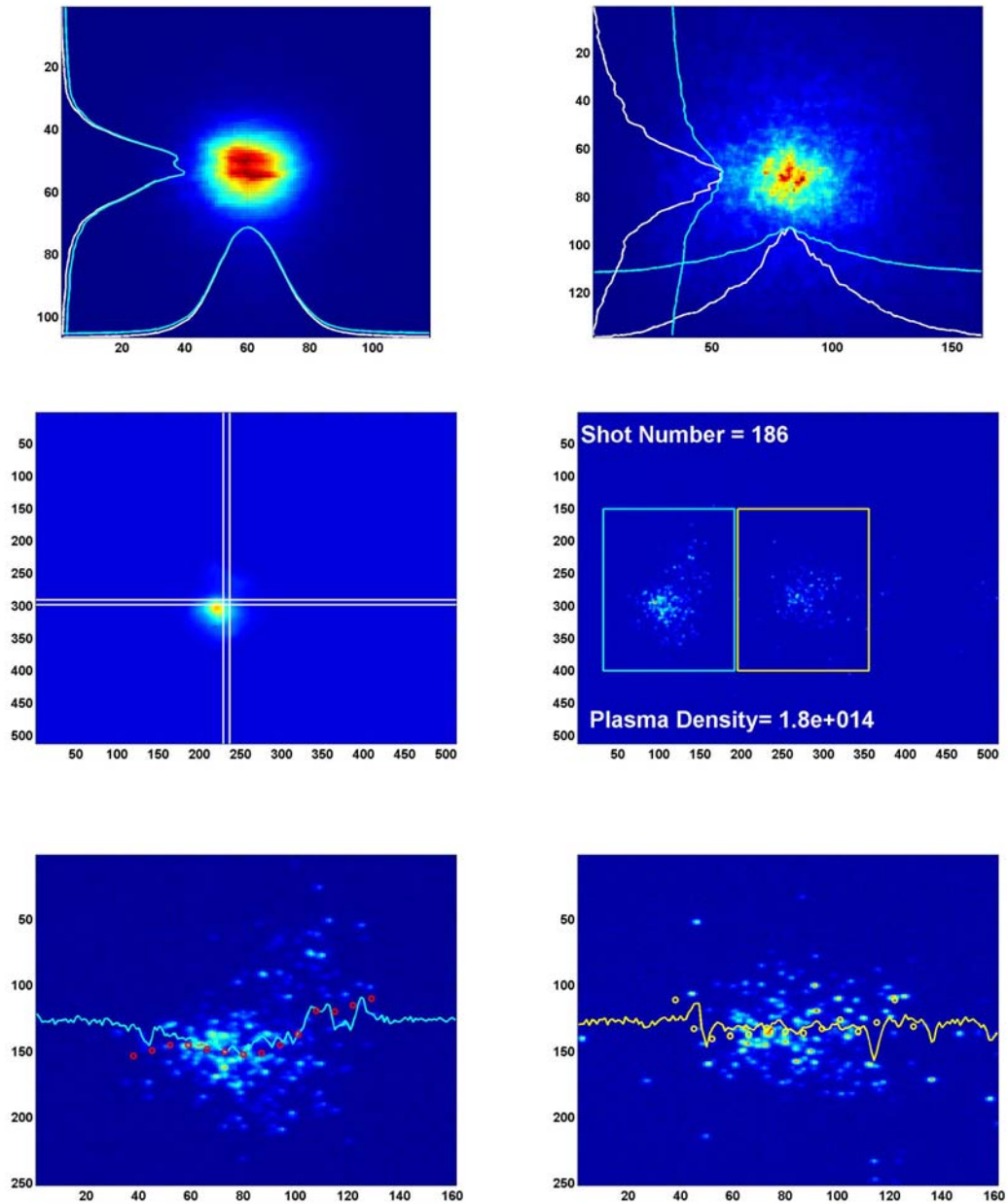


Figure B.2 Shot 186 – Plasma Density $1.8 \times 10^{14} \text{ e}^- / \text{cm}^3$ – Raw Images.

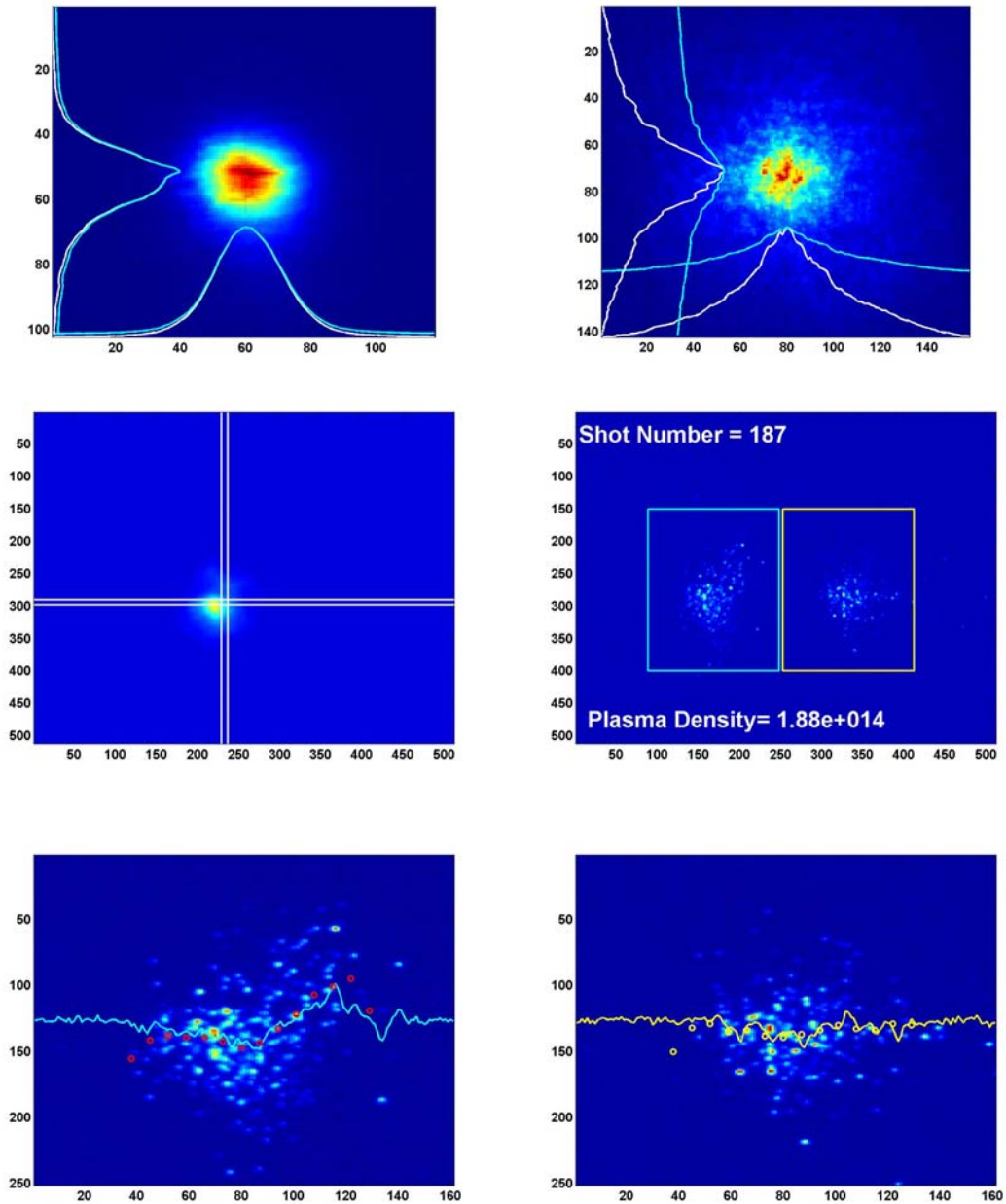


Figure B.3 Shot 187 – Plasma Density $1.88 \times 10^{14} \text{ e}^- / \text{cm}^3$ – Raw Images.

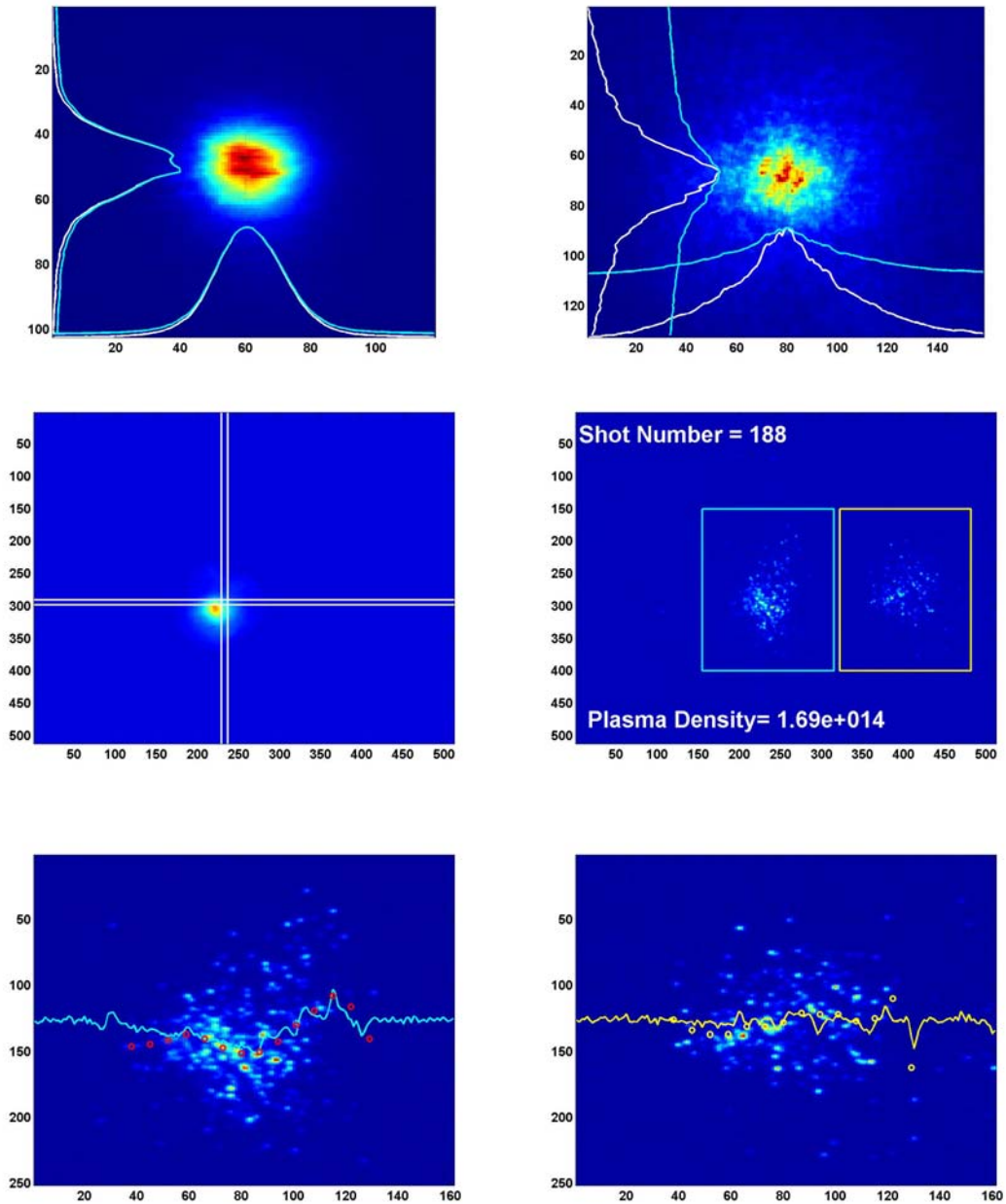


Figure B.4 Shot 188 – Plasma Density $1.69 \times 10^{14} \text{ e}^- / \text{cm}^3$ – Raw Images.

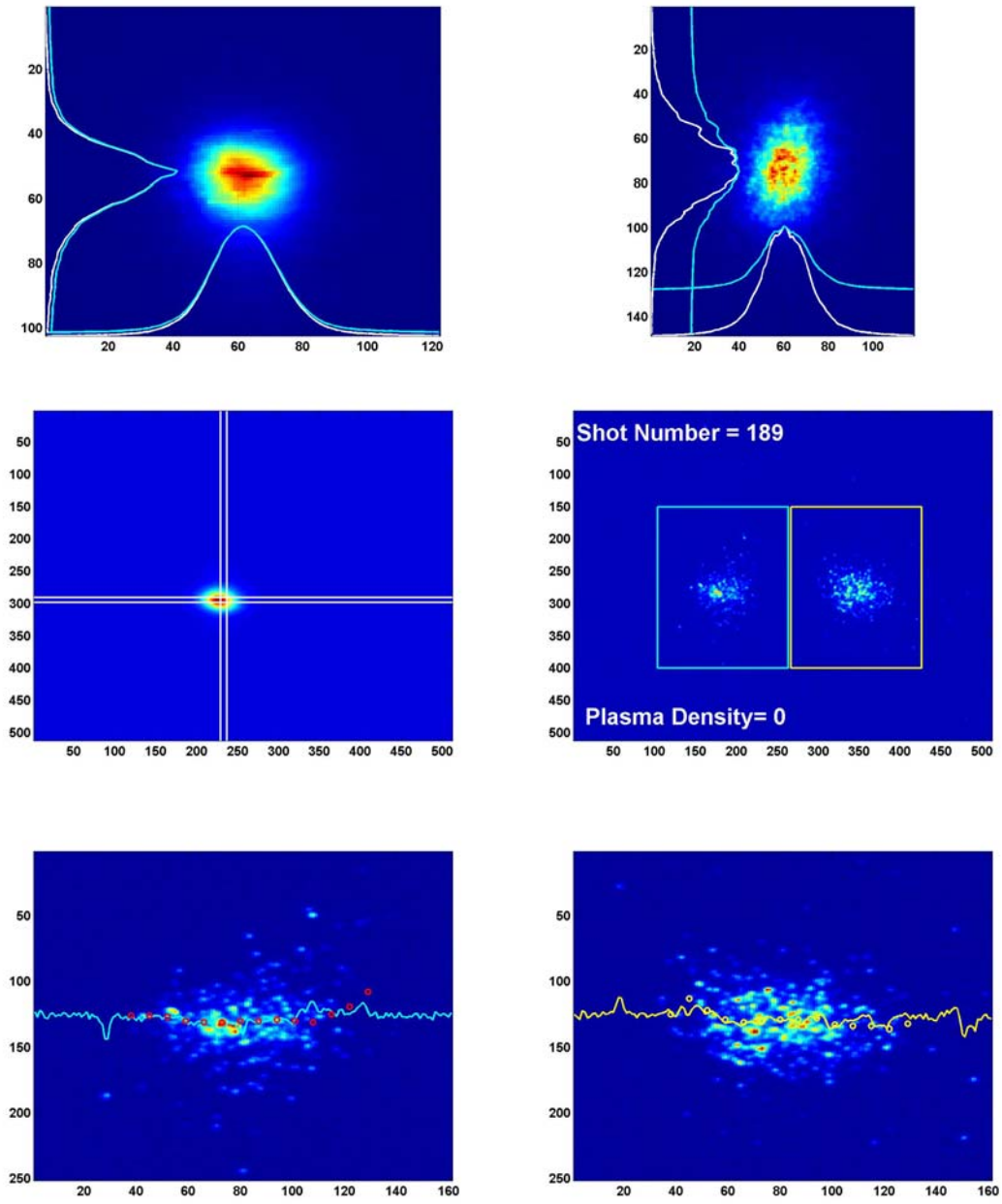


Figure B.5 Shot 189 – No Plasma – Raw Images.

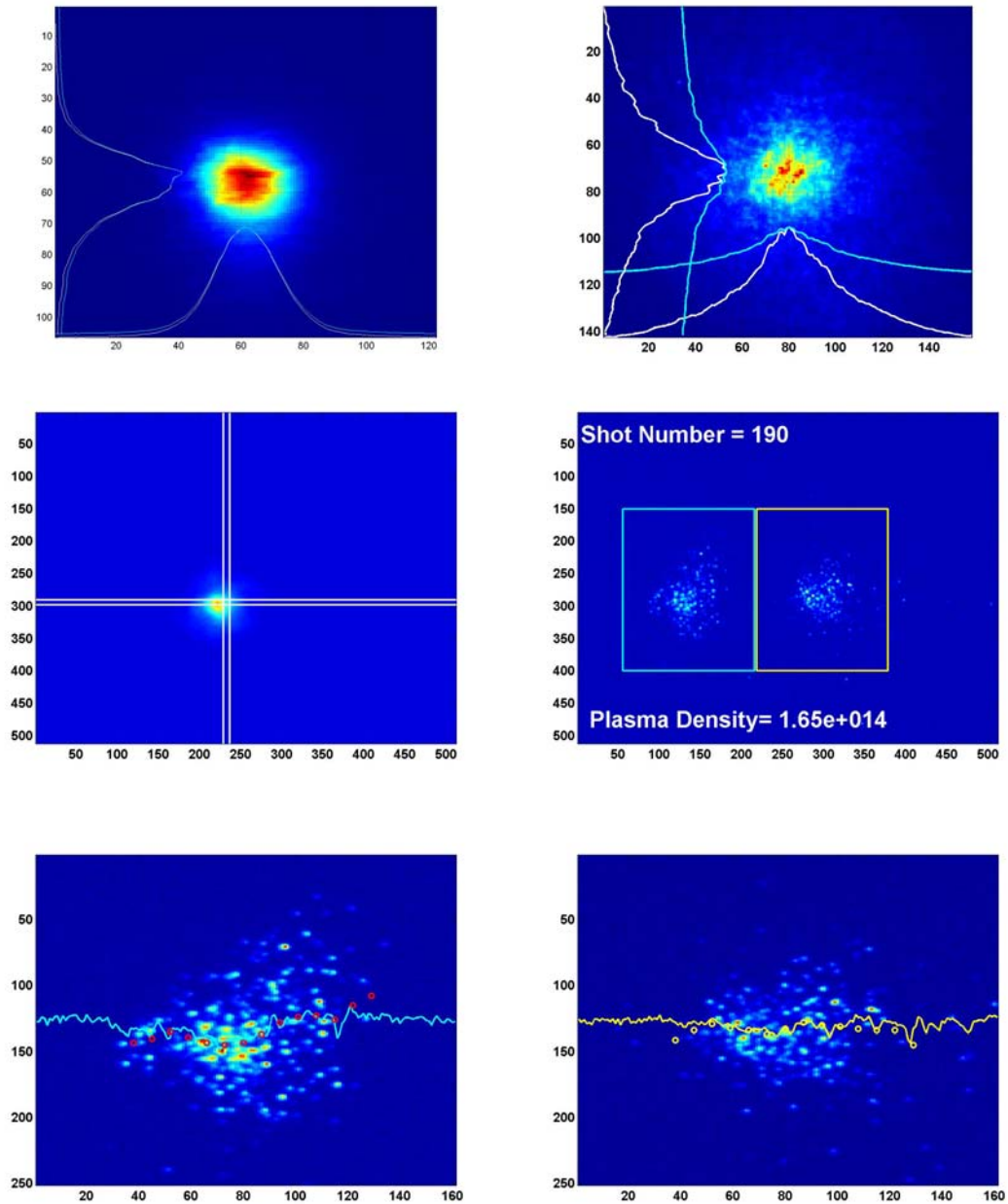


Figure B.6 Shot 190 – Plasma Density $1.65 \times 10^{14} \text{ e}^- / \text{cm}^3$ – Raw Images.

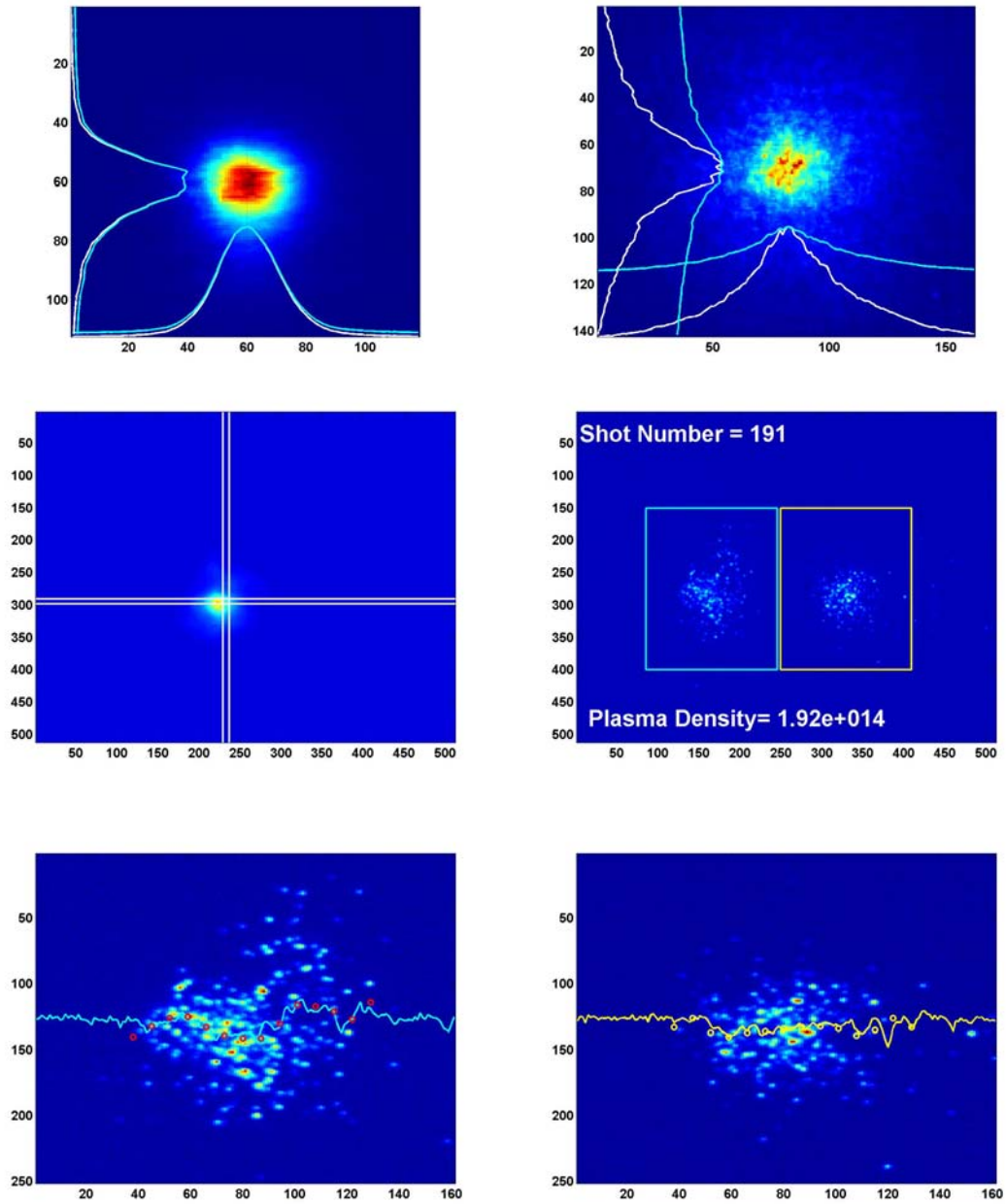


Figure B.7 Shot 191 – Plasma Density $1.92 \times 10^{14} \text{ e}^- / \text{cm}^3$ – Raw Images.

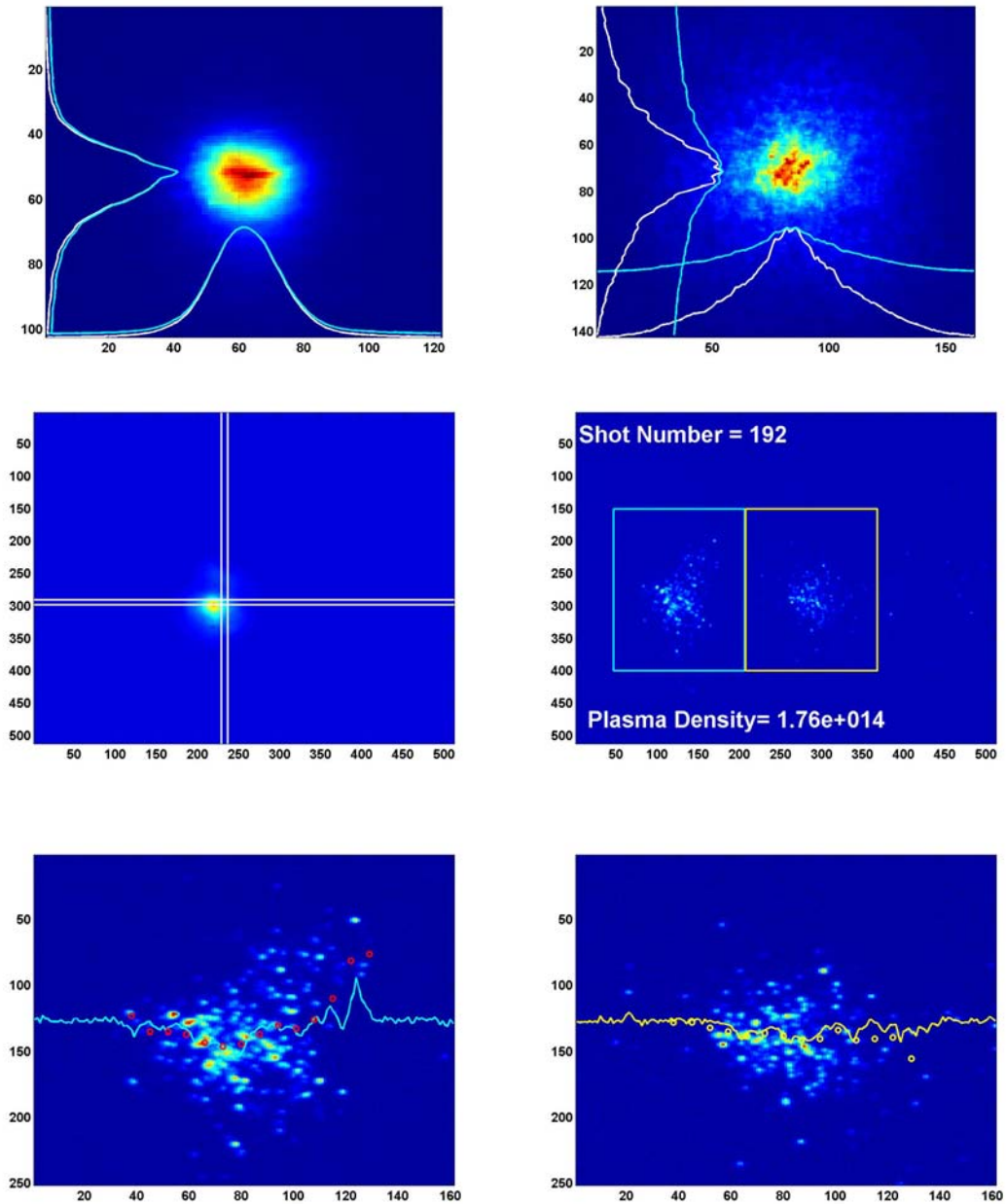


Figure B.8 Shot 192 – Plasma Density $1.76 \times 10^{14} \text{ e}^- / \text{cm}^3$ – Raw Images.

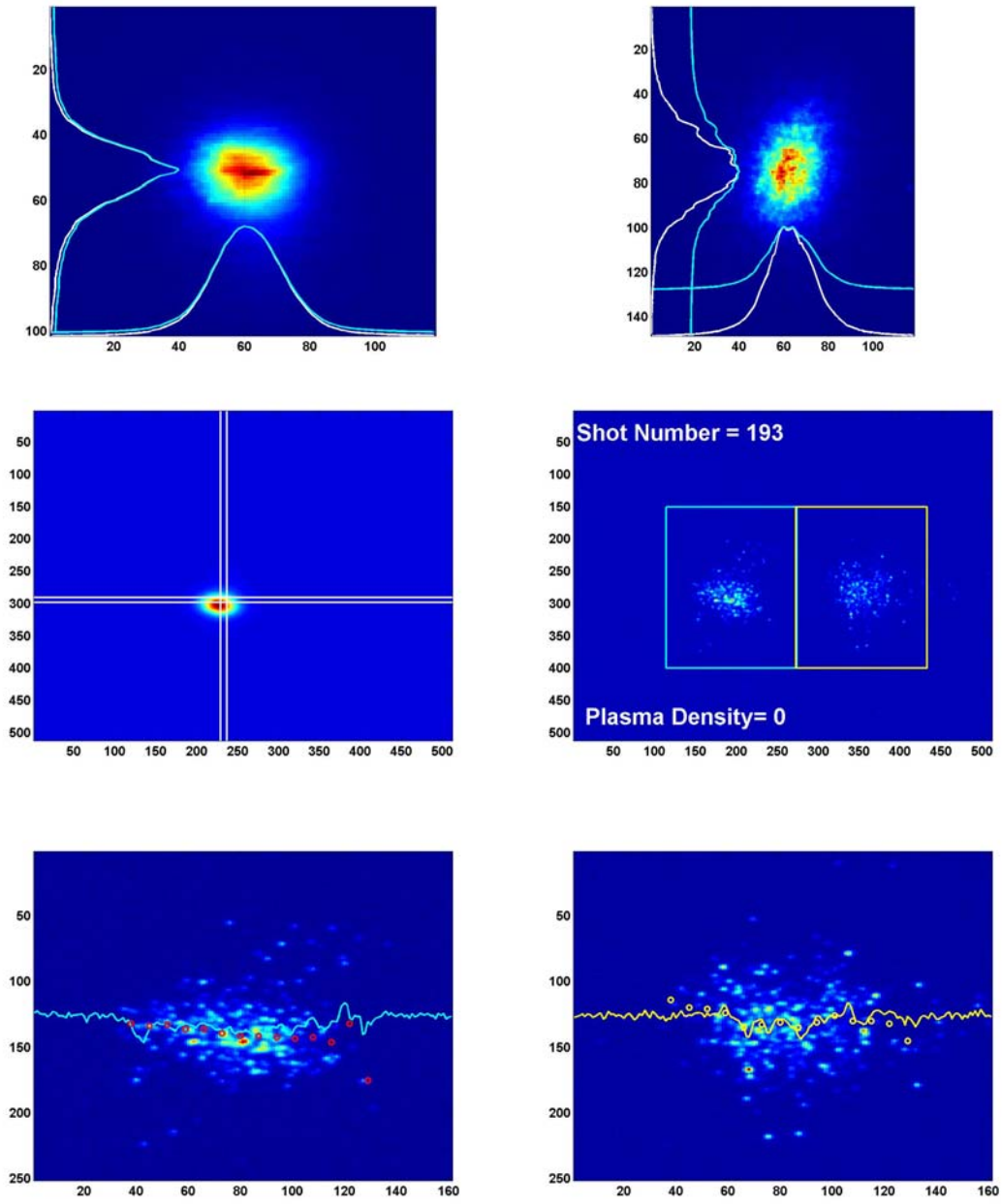


Figure B.9 Shot 193 – No Plasma – Raw Images.

Appendix C Design for an Advanced Accelerator Driven by a Proton (or Ion) Beam

This chapter presents the design for an advanced TeV electron-positron accelerator concept based on current technology and existing accelerator hardware. The first section will present the introduction to the concept. This will be followed up by simulations of different operating conditions. Finally, a couple of concepts will be explored on how to produce short proton pulses.

C.1 3rd generation plasma wakefield accelerators

In its purest sense, the plasma wakefield accelerator is an energy transformer. The energy of a drive beam is transferred to a witness beam via the plasma wakefield. Except when shaped bunches are used, the transformer ratio is limited to about 2. This implies that if a drive and a witness beam start with the same energy, the drive beam could lose all of its energy, and the witness beam would double its energy. For instance, the afterburner idea [37] would double the 50 GeV energy of the SLAC electron and positron beams to 100 GeV just before the interaction point (IP). In one sense, this is very attractive because the collision energy at the SLAC IP could be doubled without building additional accelerator infrastructure. The downside is that a significant existing infrastructure is needed to generate the drive beam. An ideal case would be to generate a high energy drive beam in a small space and use it to drive the

plasma wakefield accelerator while injecting a witness beam which would be accelerated to the high drive beam energy.

Before the advanced concept is presented, it is necessary to understand the two main types of high energy accelerators: linear and circular. High energy electron-positron colliders use linear accelerators because these particles lose unacceptably high amounts of energy from synchrotron radiation when they are centripetally accelerated. This is because the energy dissipated by synchrotron radiation scales as γ^4 and electron and positrons, due to their small mass, have a high Lorentz factor. The highest energies achieved in a linear collider were the 50 GeV ($\gamma \sim 10^5$) electrons and positrons generated at SLAC. On the other hand, circular accelerators can bring massive particles (protons, antiprotons, ions, etc.) up to TeV energies since their Lorentz factor is lower. Currently, 1 TeV protons ($\gamma \sim 10^3$) are generated in the Tevatron at Fermilab. What is readily apparent is that circular colliders can generate much higher energy particles than their linear counterparts. The shortcoming is that while electrons and positrons are fundamental particles, protons and antiprotons are not. Whereas $e^- - e^+$ collisions utilize all of the particles energy in annihilation, $p - \bar{p}$ collisions utilize only part of the total energy because one is actually colliding quarks and antiquarks that make up the protons and antiprotons.

My proposal is to drive plasma wakefields with high energy proton or ion beams and witness the wakefield with electrons or positrons. This scheme utilizes the

benefits of both types of accelerators. A high energy proton beam would be accelerated to the TeV energy range in a circular machine. The beam would then be extracted and sent into a plasma wakefield accelerator cell. Behind the proton bunch, a low energy (~ 1 GeV) electron or positron beam would be injected into the wakefield and accelerated. If we assume that the energy loss of the drive beam is equal to the energy gain of the witness beam, it is conceivable that a 500 GeV or greater electron or positrons beam could be generated.

In addition to their high drive beam energy, protons are also attractive since their high mass will diminish transverse dynamics (as compared to the electron/positron drive beam) and aid in the suppression of instabilities. A central parameter associated with transverse dynamics is the beam wave number k_b .

$$k_b = \frac{\omega_b}{c} = \frac{1}{c} \sqrt{\frac{4\pi q^2 N_b}{\gamma m}} \quad (\text{C.1})$$

The period of transverse oscillations of a beam in a plasma channel scales as k_b^{-1} , so as γm (the relativistic mass of the particle) is increased, the period increases. For instance a centroid which has an initial offset y_0 in the plasma channel will evolve according to equation C.2.

$$y(z) = y_0 \cos(k_b z) \quad (\text{C.2})$$

It is this increase in transverse “stiffness” which increases in oscillatory period and will aid in suppression of beam instabilities.

This method of plasma wakefield acceleration can be considered to be the third generation of PWFAs. The first generation used a PWFA driven in the linear regime. The second generation improved on the idea by operating in the nonlinear regime. This third regime advances the PWFA into a true energy transformer. A compact, high energy drive beam source is used to accelerate a beam of fundamental particles to a very high energy.

C.2 Simulations of proton driven PWFAs

The parameters for these following simulations are based on the use of advanced proton and ion sources [38, 39]. These sources provide the high charge ($N_b > 10^{10}$), short pulse ($\sigma_z < 1mm$) needed to drive the high ($E_z > 1GV/m$) accelerating gradient PWFAs. As a first proof-of-principle simulation, we look at the wake generated by a short proton bunch injected into a high plasma density plasma cell. The parameters for the simulation are given in table C.2.1.

Parameter	Value
Proton Beam Energy	1 TeV
Number of Protons N_b	$4 \times 10^{10} p$
Bunch Length σ_z	$40 \mu m$
Bunch Radius σ_r	$40 \mu m$
Plasma Density n_p	$1 \times 10^{17} e^- / cm^3$
Simulation Cell Size $\Delta_r \times \Delta_z$	$4 \mu m \times 4 \mu m$
Simulation Window $R \times Z$	$1200 \mu m \times 480 \mu m$

Table C.2.1 Proton PWFA simulation parameters

The on-axis longitudinal electric field (red) is shown in the following figure with the charge distribution shown in black. As seen in the figure, the front half of the beam witnesses a decelerating field and the back half of the bunch witnesses an accelerating field. Although the decelerating wake is sinusoidal (as we would expect from linear theory), the accelerating field has a complex structure. This is because the bunch length is greater than the plasma wavelength ($\lambda_p = 27 \mu m$). As the plasma electrons are pulled in from different radii, their field constructively and destructively interfere which gives rise to the complex accelerating field. Although complex, the magnitude of the accelerating field is much higher than the fields currently used in high energy

particle accelerators. The peak accelerating field is greater than 3 GV/m and the peak decelerating field is close to 4 GV/m.

The interpretation of accelerating and decelerating fields is reversed if we are considering the acceleration of electrons in the wakefield of a proton beam. The decelerating field in the front half of the drive beam is an accelerating field for electrons. This is because the proton and electron have a charge which is equal in magnitude, but opposite in sign. Because of this, the transformer ratio is exactly one since the decelerating field is the accelerating field. If this field could be utilized over 150 meters for the acceleration of electrons, the resultant beam energy of 600 GeV would be greater than the initial design energy of future linear colliders (which are ~ 30,000 meters long). Over the same distance, the drive beam would loss 600 GeV. A proton beam with an energy of 1 TeV has more than enough energy to drive this 150 meter PWFA.

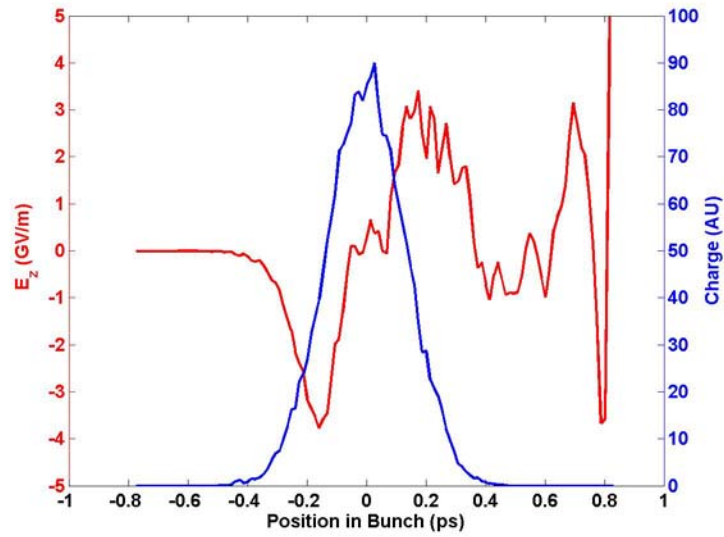


Figure C.2.1 Wakefield field induced in a plasma by a proton beam

In practice, producing a meter-scale uniform plasma column with a $10^{17} e^- / cm^3$ can be difficult. One idea is to use the beam's own electric field to ionize the neutral gas. The following figure shows the wakefield induced by a proton beam in a neutral gas. The parameters are the same as in table C.2.1, except the initial plasma is replaced by a 10 torr Lithium vapor.

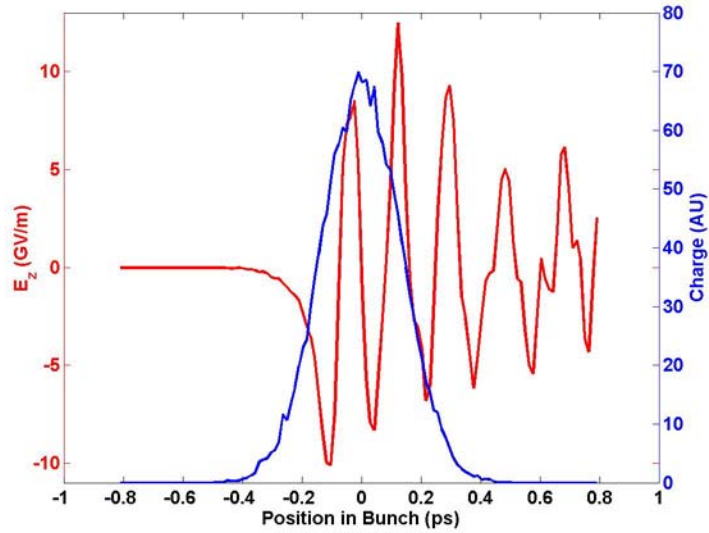


Figure C.2.2 Wakefield induced by a proton beam in a Li vapor

Two features of the wakefield are readily apparent. First, the field varies sinusoidally with a period ($\lambda_{E_z} = 45 \mu m$) which is much shorter than the preionized plasma case. The period of the field corresponds to the beam density ($n_b = 3 \times 10^{16} p/cm^3$). Second, the magnitude of the peak accelerating field is on the order of 10 GV/m and the magnitude of the peak decelerating field is 13 GV/m. As in the preionized plasma case, a decelerating field for the proton beam ($E_z < 0$) is an accelerating field for the electron beam and vice versa. These two features of the wakefield are due to the finite radius of the plasma column as shown in figure C.2.3. The figure depicts the neutral gas density in blue and the radial profile of the proton beam in red. The beam fully ionizes the gas out to a radius of $\sim \sigma_r/2$ and the full channel width extends out to

$\sim 3\sigma_r$. The physics and theory developed for PWFAs has concentrated on the beam dynamics inside an infinite (plasma radius \gg beam radius) preionized plasma. The dynamics of a beam in a narrow channel (plasma radius \sim beam radius) will be the topic of new research since high density, beam ionized plasmas are needed for future PWFAs.

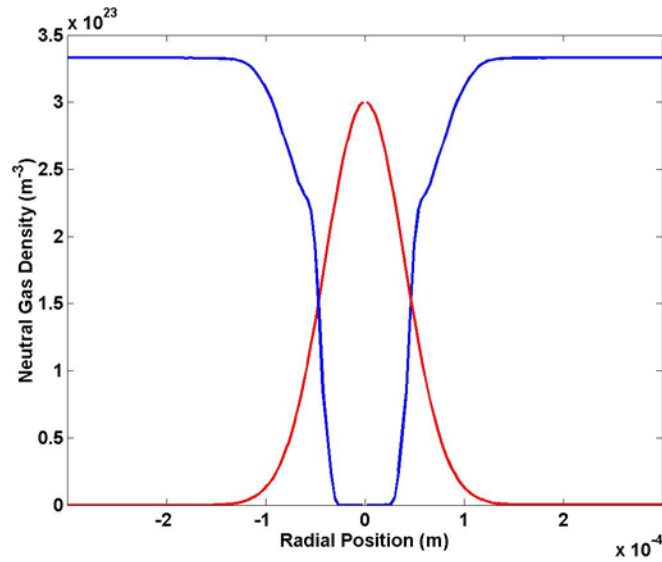


Figure C.2.3 Tunnel ionized channel width

Now that we have a feeling for the extraordinarily high fields which are generated by the proton beam, we look at how a witness electron beam will be affected by the wakefield, and how the electron beam might in turn effect the wakefield. The parameters for the simulation are identical to the tunnel ionized case, except now an electron beam is injected which has the same spatial extent as the drive beam and $1/10^{\text{th}}$ the charge.

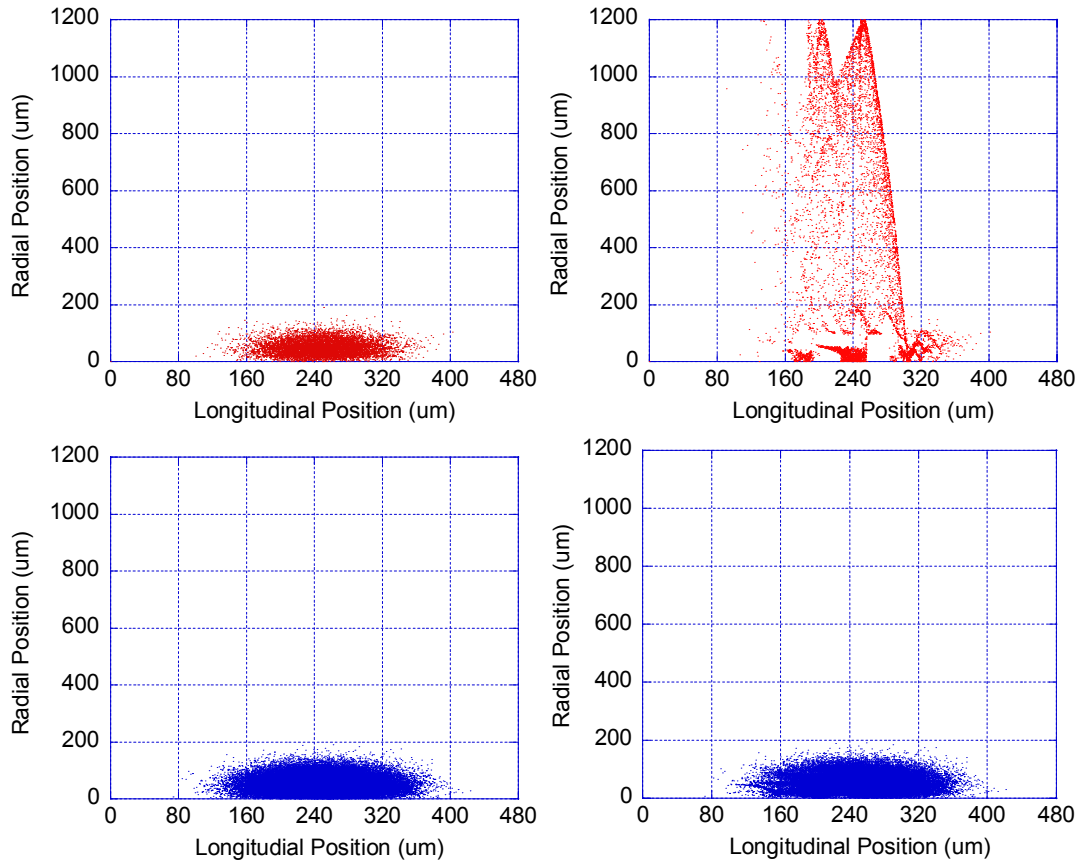


Figure C.2.4 Evolution of the proton drive beam (blue) and witness electron beam (red). The horizontal axis is the longitudinal profile of the beam in the beam's rest frame. The vertical axis is the radial profile of the beam with zero being the centerline of the beam. Each point above represents a macroparticle in the simulation. The snapshots of the beams are taken after the beam has traversed 500 μm (left hand side) and 6.2 mm (right hand side) of Lithium vapor. The beams are traveling from left to right in the frames. The drive beam does not significantly evolve due to its high rest mass. The electron beam is significantly affected by the radial forces generated in the plasma. Some particles are trapped near the axis, while others are strongly defocused. This was expected since the placement of the witness beam in the accelerating field was not optimized in this simulation.

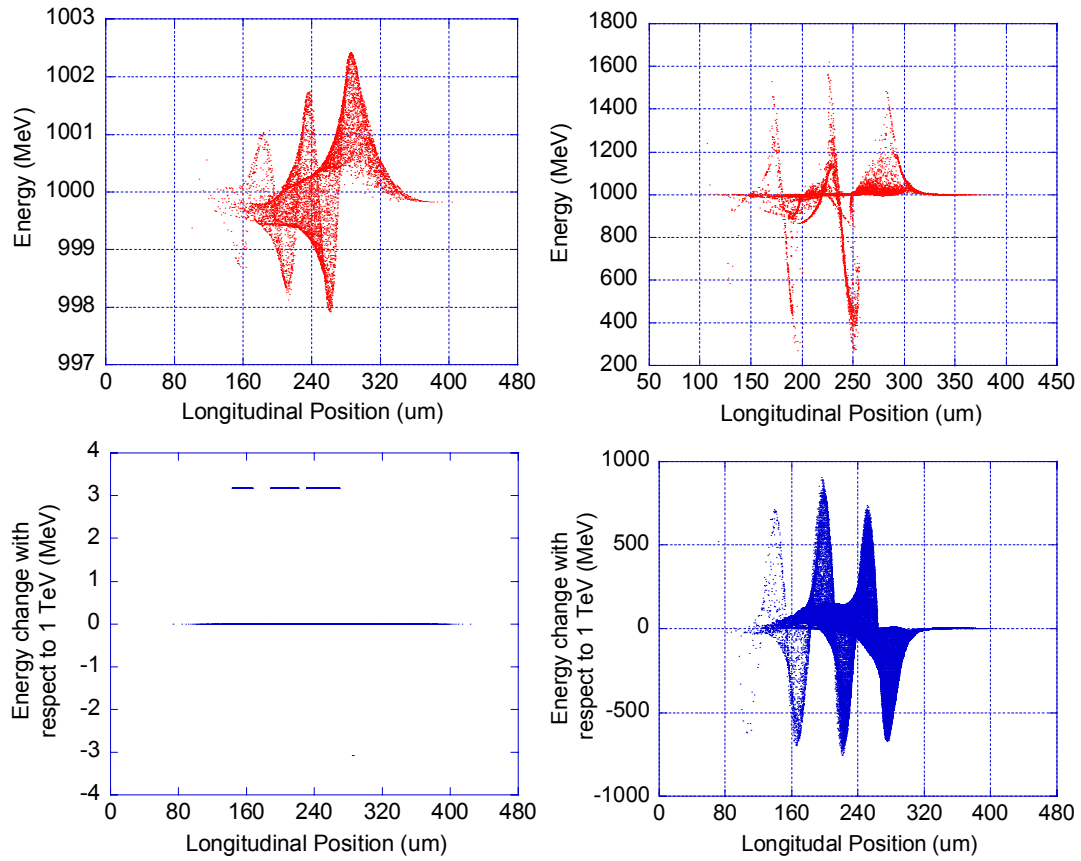


Figure C.2.5 Energy evolution of the proton drive beam (blue) and witness electron beam (red). The horizontal axis is the longitudinal profile of the beam in the beam's rest frame. The vertical axis is the energy of each beam macroparticles (each point). The snapshots of the beams are taken after the beam has traversed 500 μm (left hand side) and 6.2 mm (right hand side) of Lithium vapor. The beams are traveling from left to right in the frames. The proton beam which started at 1 TeV has negligible energy changes at 500 μm , but by 6.2 mm its energy is modulated by the wakefield with energy gains and losses on the order of 750 MeV. At 500 μm , the electron beam energy, which was initially 1 GeV, is starting to be modulated by the proton driven plasma wakefield. After 6.2 mm, the electron beam has a maximum energy gain of over 600 MeV. This corresponds to an accelerating gradient of ~ 10 GeV/m.

The phase velocity of the plasma wakefield is equal to the phase velocity of the proton beam. Although it is nearly traveling at the speed of light, it is not exactly. Furthermore, as the proton beam loses energy, its velocity will decrease. On the other hand, as the electron beam is accelerated, its velocity will increase. One limit on the interaction length of the PWFA is the distance the accelerating electron beam can travel while still inside the accelerating field of the decelerating proton wakefield. As an example we consider the separation between an electron beam which has an initial energy of 1 GeV and a wakefield which is propagating at the velocity of a 1 TeV proton beam. The proton beam will lose energy at the rate of 10 GeV/m and the electron beam will gain energy at the same rate. Figure C.2.6 shows the separation between the electron bunch and the proton wakefield versus distance traveled.

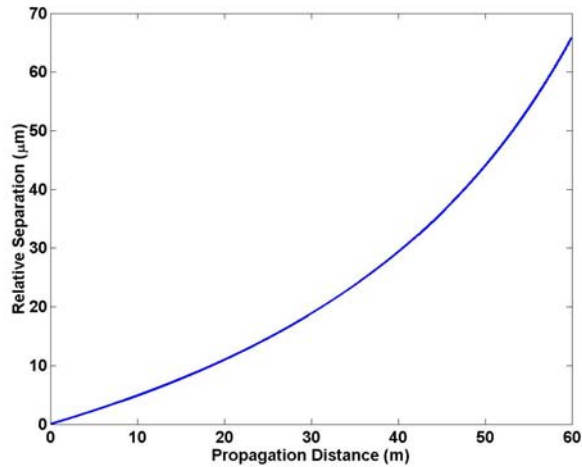


Figure C.2.6 Relative separation between an accelerating electron bunch and a decelerating proton bunch in a 10 GeV/m PWFA. The bunches, which initially start at the same longitudinal position, propagate at different velocities due to their different, and changing, Lorentz factors. We set a limit of $\lambda_w/10$ to be the maximum acceptable separation (where λ_w is the wakefield wavelength) so that the injected electron bunch would stay near the peak of the accelerating field. In the tunnel ionized plasma case, the wakefield wavelength is 45 μm , so the maximum accelerator section length is 10 meters. This implies that 5 PWFA sections would need to be staged together to reach the 500 GeV design goal of the next generation linear colliders. If we assume a drive beam energy of 7 TeV (the Large Hadron Collider (LHC) energy at CERN), phase slip is not an issue for 100's of meters of propagation. These assumptions on the velocity of the wakefield assumed that the drive beam did not significantly evolve. Further studies are needed to address this concern.

C.3 Methods of generating short ($< 100\mu\text{m } \sigma_z$) proton pulses

One hurdle which needs to be overcome, is the generation of short proton pulses. Our definition of short is bunches which are less than 100 μm long. For comparison, current and future circular accelerators use bunches which are several centimeters in length. For instance the bunch length in the Tevatron is 28 cm, and the

proposed bunch length in the LHC is 7 cm. The reason the bunch lengths are long is that collider designers strive for a higher luminosity which scales as the beam charge. One limiting factor is a limit on beam current which scales as the charge divided by the bunch length. So in order to have a higher luminosity, collider designers use a long bunch with high charge. Since short proton bunches have not previously been needed, little to no research has been done on the generation of these bunches. On the other hand, electron/positron linear accelerators have been driven towards short pulse lengths since high frequency accelerating structures, which have a higher accelerating gradient, require short bunches. Our goal here is not to provide a final solution to the problem, rather to explore methods which show that it is feasible to generate short proton bunches using extensions of current technology.

One method for generating a short proton bunch is where a powerful, short pulse laser strikes a thin foil [38, 39]. When the laser hits the target, it forms a plasma, and in turn accelerates the plasma electrons through the foil. As the electrons leave the backside of the foil, their space charge “drags” the protons out of the foil. The ejected proton bunch has a high charge ($> 10^{13}$ p), (expected to have) a short pulse length (~ 300 μm), and is at a moderate energy (~ 20 MeV) with a large energy spread. Since the energy is much less than the proton rest mass, the bunch is not relativistic and space charge will broaden the pulse length. Experimental evidence has shown that the proton energy scales as the laser intensity. If we assume that the proton pulse

would need to have an energy greater than a few GeV in order to minimize longitudinal space charge broadening, we would need a laser intensity of $10^{21} - 10^{22} \text{ W/cm}^2$ (following $I\lambda^2$ scaling [40]). Although such a laser system does not currently exist, it is foreseeable it will be built in the not too distant future.

Another possible technique is to velocity modulate a long, low energy, relativistic proton bunch with a high frequency plasma wakefield. A high current, short electron pulse could be injected into a neutral gas in order to generate a wakefield. This is the same case as last section, except now we are using an electron beam to tunnel ionize the gas and drive a wakefield. Figure C.3.1 shows the wakefield generated in a tunnel ionized Lithium plasma by a high current electron beam which is injected into the temporal center of a long proton bunch.

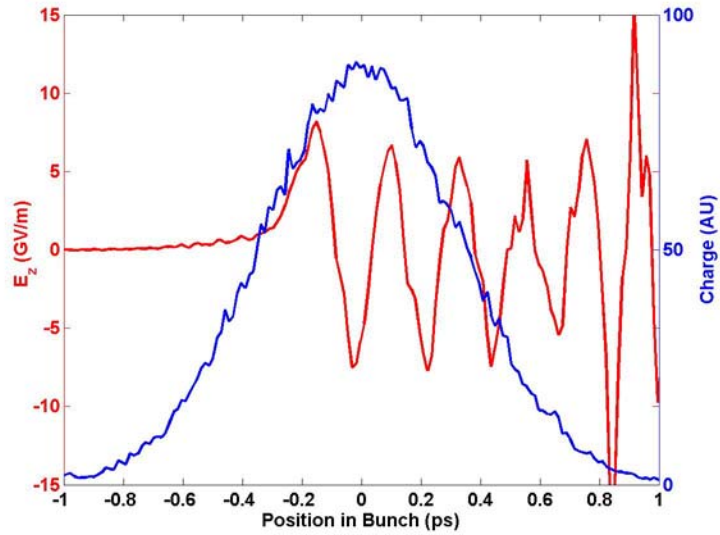


Figure C.3.1 Wakefield (red) generated by a electron beam (blue) in a tunnel ionized 10 torr plasma. A 20 GeV, 100 μm long, 40 μm wide electron bunch with 4×10^{10} particles is injected in the temporal middle of a 10 GeV, 1 cm long, 40 μm wide proton bunch (not shown) with 1×10^{12} particles. The wakefield has a magnitude of ~ 8 GV/m and a period λ_w of 76 μm . Protons which witness an accelerating field will stay in their current accelerating bucket, while those which are decelerated will fall into a trailing bucket. This will cause the beam to break up into a series of micropulses whose pulse widths will be less than $\lambda_w / 2$. For instance, if the beam passed through a 1 mm long gas jet and allowed to drift 3 meters, the protons at the peak of the field would accelerate forward in the bunch to meet the protons which were decelerated from the preceding peak decelerating field. A pulse train would emerge with ~ 40 μm long microbunches which would contain $\sim 4 \times 10^9$ protons. The jitter in the wake and charge distribution is numerical noise in the simulation.

Bibliography

- 1 T. Tajima and J.M. Dawson, "Laser Electron Accelerator," Phys. Rev. Lett. Vol. 43, pp. 267-270, 1979.
- 2 J.M. Dawson, "Nonlinear electron oscillations in a cold plasma," Phys. Rev., vol. 133, pp. 383-387, 1959.
- 3 J.W. Wang et al, "High gradient tests of SLAC linear collider accelerator structures," SLAC-PUB-6617, Aug. (1994).
- 4 Y. Kitagawa et. al., "Beat-Wave excitation of plasma wave and observation of accelerated electrons," Phys. Rev. Lett., Vol. 68, pp. 48-51, 1992.
- 5 C.E. Clayton et. al., "Ultra-high gradient acceleration of injected electrons by laser-excited relativistic electron plasma waves," Phys. Rev. Lett., Vol. 70, pp. 37-40, 1993.
- 6 M. Everett et. al., "Trapped electron acceleration by a laser-driven relativistic plasma wave," Nature, Vol. 368, pp. 527-529, 1994.
- 7 C. Cloverdale et. al., "Propagation of intense subpicosecond laser pulses through underdense plasma," Phys. Rev. Lett., Vol. 74, pp. 4659-4662, 1995.
- 8 A. Modena et. al., "Electron acceleration from the breaking of relativistic plasma waves," Nature, Vol. 337, pp. 606-608, 1995.
- 9 K. Nakajima et. al., "Observation of ultrahigh gradient electron acceleration by a self-modulated intense short laser pulse," Phys. Rev. Lett., Vol. 74, pp. 4428-4431, 1995.
- 10 J. Rosenzweig et. al., "Experimental measurements of nonlinear plasma wakefields," Phys. Rev. A., Vol. 39, pp 1586-1589, 1989.
- 11 A. Ogata, "Plasma lens and wake experiments in Japan," Proc.of the Advanced Accelerator Concepts, Vol 279, pp. 420-449, 1993.

- 12 A.K. Berezin et. al., "Wake field excitation in plasma by a relativistic pulse with a controlled number of short bunches," *Plasma Phys. Rep.*, Vol. 20, pp. 596-602, 1994.
- 13 A.A. Geraci, D.H. Wittum, "Transverse dynamics of a relativistic electron beam in an underdense plasma channel," *Phys. Plasmas*, vol. 7, pp. 3431, (2000).
- 14 M.J. Hogan et al, "Ultra-relativistic positron-beam transport through meter-scale plasmas," Submitted to PRL (2002)
- 15 M.J. Hogan et al, "E162: Positron and electron dynamics in a plasma wakefield accelerator," SLAC-ARDB-242, Oct. (2000).
- 16 P. Chen, J.M. Dawson, R.W. Huff, and T. Katsouleas, "Acceleration of electrons by the interaction of a bunched electron beam with a plasma", *Phys. Rev. Lett.* Vol. 54, 693 (1985).
- 17 R. Keinigs and M. Jones, *Physics of Fluids*, 30, 252 (1987).
- 18 R.D. Ruth et al, "A plasma wakefield accelerator," *Particle Accelerators*, vol 17, pp. 171-189 (1985).
- 19 P. Chen et al, "Energy transfer in the plasma wakefield accelerator," *Phys. Rev. Lett.*, vol 56, pp. 1252 (1986).
- 20 J. B. Rosenzweig, "Nonlinear plasma dynamics in the plasma wakefield accelerator," *Phys. Rev. Lett.*, vol 58, pp. 555 (1987).
- 21 J. B. Rosenzweig, B. Breizman, T. Katsouleas, and J. J. Su, "Acceleration and focusing of electrons in two-dimensional nonlinear plasma wake fields", *Phys. Rev. A*, vol. 44, 6189 (1991).
- 22 J.B. Rosenzweig et al, "Experimental observation of plasma wakefield acceleration," *Phys. Rev. Lett.*, vol. 61, pp. 98 (1988).
- 23 K. Nakajima, *et al.* Plasma Wake-field Accelerator Experiment at KEK, NIM-A vol. 292, pp 12 (1990).
- 24 H. Nakanishi, et al. Wakefield Accelerator Using Twin Linacs, NIM-A vol 328, pp. 596 (1993).

- 25 Clayton, C. et.al., “Transverse envelope dynamics of a 28.5-GeV electron beam in a long plasma,” *Phys. Rev. Lett.*, April 15, (2002).
- 26 O’Connell, C. et. al., “Dynamic focusing of an electron beam through a long plasma,” *PRLST-AB*, Vol 5, 121301 (2002).
- 27 B. Blue, “Hosing Instability of the Drive Electron Beam in the E157 Plasma Wakefield Acceleration Experiment at the Stanford Linear Accelerator,” Master’s Thesis, UCLA (2000).
- 28 P. Muggli et al, “A high gradient plasma wakefield accelerator,” Submitted to *Science* (2003).
- 29 Blue, B. et. al. “Plasma Wakefield Acceleration of an Intense Positron Beam”. *Nature* (2003).
- 30 P. Muggli et al, “Photo-ionized Lithium source for plasma accelerator applications,” *IEEE Transactions on Plasma Science*, vol. 27, pp. 791 (1999).
- 31 V.A. Lebedev, “Diffraction-limited resolution of the optical transition monitor,” *Nucl. Instr. And Meth. A*, vol. 372, pp. 344, (1996).
- 32 M. Castellano and V.A. Verzilov, “Spatial resolution in optical transition beam diagnostics,” *Phys. Rev. ST Accel. Beams*, vol 1, 062801, (1998).
- 33 S. Smith, P. Tenenbaum, S.H. Williams, “Performance of the beam position monitor system of the Final Focus Test Beam,” *Nuclear Instruments & Methods in Physics Research, Section A*, vol.431, pp.9, (1999).
- 34 Hogan, M. *et al.* E-157: A 1.4-m-long plasma wake field acceleration experiment using a 30 GeV electron beam from the Stanford Linear Accelerator Center linac. *Phys. Plasmas*, vol 7, 2241 (2000).
- 35 D.R. Bates et al., “Recombination Between Electrons and Atomic Ions. I. Optically Thin Plasmas ,”*Proc. Of Royal Society*, vol. 267, pp. 297 (1962).
- 36 J.D. Jackson, *Classical Electrodynamics*, 3rd Ed. pp. 646-654, New York, John Wiley & Sons, Inc., 1998.

- 37 S. Lee et. al. "Energy Doubler for a Linear Collider." Phys Rev Lett ST AB, Vol 5. 011001. (2002).
- 38 M. Hegelich et al, "MeV ion jets from short-pulse-laser interaction with thin foils," Phys. Rev. Lett., vol. 89, 085002 (2002).
- 39 R. Snavely et al, "Intense High-Energy Proton Beams from Petawatt-Laser Irradiation of Solids," Phys. Rev. Lett., vol 85, 2945 (2000).
- 40 S. J. Gitomer et al, "Fast ions and hot electrons in the laser-plasma interaction," Phys. Fluids, vol. 29, pp. 2679 (1986).
- 41 E. Dodd et al, "Hosing and Sloshing of Short-Pulse GeV-Class Wakefield Drivers," Phys ReV Lett, vol 88, 125001 (2002).